

Time-resolving electrical conduction in thin iron films

Dissertation
zur Erlangung des Grades
“Doktor
der Naturwissenschaften”
am Fachbereich Physik, Mathematik und Informatik
der Johannes Gutenberg-Universität
in Mainz

Keno Lorenz Krewer

geboren in Mainz
Mainz, den 24.03.2020

1. Gutachter: Prof. Dr. Mischa Bonn
2. Gutachter: Prof. Dr. Dmitry Budker

Datum der mündlichen Prüfung: 10.06.2020

Keno Krewer
AK Bonn
Max-Planck-Institut für Polymerforschung
Ackermannweg 10
D-55128 Mainz
krewer@mpip-mainz.mpg.de

Contents

Acknowledgments	3
Abstract	5
Kurzfassung	7
1 The concept of time-resolving conduction	11
1.1 Goal: Time-resolving the conduction process	11
1.2 Description of time-dependent conductivity	12
1.2.1 Conduction response kernel	12
1.2.2 Fourier transforming into the frequency-domain	13
1.2.3 Complex conductivity	13
1.2.3.1 Electrical conductivity of metals	14
1.3 Using an optical technique to measure electrical currents	15
1.3.1 Equivalence between optics and electronics	15
1.3.2 Refractive index, dielectric function	15
2 Theory of electrical conduction in metals	19
2.1 Drude model	19
2.2 Semiclassical Bloch-Boltzmann theory	22
2.3 Bloch waves: electronic band structure in a crystal	24
2.3.1 Reciprocal lattice of a crystal	24
2.3.2 Free electron gas	24
2.3.3 The nearly free electron model	26
2.3.4 Band bending/Bragg reflection	26
2.3.5 General band structure of a metal	27
2.3.6 Fermi energy and surfaces	28
2.4 Boltzmann equation: The role of scattering in transport	29
2.4.1 Scattering processes	29
2.4.2 From Bloch waves to quasi-particle plasma	30
2.4.3 From plasma to gas	30
2.4.4 Collision integral to relaxation times	31
2.4.4.1 Relaxation times assumption	31
2.4.4.2 Relaxation times approximation	32
2.4.4.3 Relaxation times for specific excitations	34
2.4.5 From relaxation times to conductivity	35
2.4.5.1 Frequency limit of the semiclassical theory	36

Contents

2.4.6	Maps of relaxation times and group velocities	36
2.5	Macroscopic conductivity of a relaxation time distribution	37
2.5.1	Introducing the current response time	38
2.5.2	High-frequency limit of the semiclassical picture	41
2.5.3	Universal relaxation time assumption	42
2.6	Assumptions for the relaxation time distribution model	43
2.6.1	Linearity of the response	43
2.6.2	Neglecting magnetic fields	43
2.7	Evidence for the distribution of relaxation times	44
2.7.1	Maps of point relaxation times	44
2.7.2	Deviations from Mathiessen’s rule	46
2.8	Previous models for diverse relaxation times	47
2.8.1	Mott model	47
2.8.1.1	Energy dependent relaxation times	47
2.8.1.2	Spin dependent relaxation times	47
2.8.2	Two-current models	47
2.8.2.1	Neck-belly two band model	48
2.8.2.2	Spin-split two-current model	48
2.9	Summarising	48
2.9.0.1	Calculating current dynamics from basic principles	48
2.9.0.2	Time constants describing conduction dynamics	50
3	Thickness scaling of conduction dynamics	51
3.1	Mean free path	51
3.1.1	Universal mean free path assumption	52
3.2	Thomson model	52
3.3	Fuchs model	52
3.4	Scaling of the relaxation time distribution	56
3.4.1	Narrowing by anticorrelated scattering mechanisms	57
3.4.2	Broadening by direction dependent relaxation times	57
3.5	Namba’s roughness effect	58
3.5.1	Roughness effect on measured conductivity	58
3.5.2	Roughness effect on the current response time	59
3.5.3	Roughness effect on apparent variation	60
3.5.4	Size of the roughness effect	60
3.6	Summary	60
4	Substrate referenced transmission terahertz time domain spectroscopy	61
4.1	Accessing conduction dynamics in thin metal films by substrate referenced transmission terahertz time domain spectroscopy	61
4.1.0.1	Outline	61
4.2	Terahertz time domain spectroscopy	62
4.2.1	Specific set-up used	62
4.2.1.1	Time trace of a terahertz pulse	64

4.2.1.2	Frequency domain spectra	66
4.2.1.3	Relative transmission	66
4.3	Inverting the transfer function	67
4.3.1	Geometry	68
4.3.1.1	The sample	68
4.3.1.2	Path of the pulse through the sample	68
4.3.2	Transfer matrix method	70
4.3.2.1	Fresnel coefficients	70
4.3.2.2	Transfer matrix	71
4.3.3	Transfer function	72
4.3.3.1	Thin film approximation	73
4.3.3.2	Thin conductive film approximation	74
4.4	Substrate thickness correction	74
4.4.1	Substrate thickness difference	75
4.4.1.1	Basic impact of variations in substrate thickness	76
4.4.1.2	Thickness difference indistinguishable from response time	77
4.4.1.3	Sheet conductance impacts thickness difference effect	78
4.4.1.4	Necessary precision	79
4.4.2	Measuring the substrate thickness difference with the echo	80
4.4.2.1	Beam path of the echo	81
4.4.2.2	Transfer function of the echo	81
4.4.3	Thin stack approximation	82
4.4.3.1	Arbitrary angles of incidence	84
4.4.4	Thick conductive film approximation	84
4.5	Measurements of the thickness difference	85
4.5.1	Precision estimation	85
4.5.2	Measurement and statistical precision	86
4.5.3	Comparing thin and conductive approximations	88
4.6	The thin conductive oxymoron	89
5	Conduction dynamics in thin iron films	93
5.1	Preparation and characterisation of the iron films	94
5.2	Conductivity spectra of the iron films	96
5.2.1	Example spectra	97
5.2.2	Residual correlation	98
5.2.2.1	Origin of the artefacts	100
5.3	Thickness scaling of conduction	100
5.3.1	Comparison with previous works	101
5.3.1.1	THz spectroscopy values for iron	101
5.3.1.2	Thickness scaling of THz conductivity in metals	102
5.3.1.3	Thickness scaling of iron DC-conductivity	102
5.3.1.4	Comparison to other spectroscopic data	105

Contents

5.3.1.5	THz conductivity deduced from surface plasmon polar- ition propagation	105
5.4	Thickness scaling of the variation of relaxation times	106
5.4.1	Comparison with band structure calculations	109
5.4.2	Comparison with Drude's model	109
5.5	Summary	110
6	Impact of time-resolving conduction in a metal	111
7	Appendix	115
7.1	Different relaxation times approximation	115
7.2	Geometry of the iron film samples	115
7.3	Substrate index	116
7.4	Measurement series	119

Dedication

To Eric, Eduard and Paniz, who unfortunately are no longer around to read this.

Acknowledgements

“Everything you write can and will be used against you.” - Dr. Christoph Bernhard

I wrote this thesis and performed the work leading up to it with the help and support of a lot of people. I would like to thank those people, so the following lines will contain the word thanks a lot.

First of all, I would like to thank Mischa Bonn for supervising me all the way and taking over the role of corrector which allowed me to continue this dissertation. I would also like to thank Dmitry Budker for fulfilling the role as second corrector when the Dekanat assigned this role to him in its mysterious ways.

Further, I would like to thank my family and friends, especially my parents for supporting me. Thanks for not worrying too much despite me taking so long. Thanks to Leonard Doble for proofreading as a native speaker.

I would like to thank the members of to the original THz group, of which I am one of the last remnants; especially I would like to thank:

Zoltan Mics for teaching me how to work on optics and giving me valuable advice on how to deal with the hardships of science;

Zuanming Jin for showing me the ropes and setting me on the path that led here;

Ivan Ivanov for being a good friend and neighbour and his eagle eye for optics and design;

Hassan Hafez for his cheerful and charismatic ways in scientific and unscientific discussions;

Eduard Unger who opened my eyes to the full potential of set-up automation and whose friendly and relaxed but very effective way of life I find something to aspire to;

Wentao Zhang for helping with software and measurements, and from near and far away;

Francesco D’Angelo for teaching me that perfect is the mortal enemy of good enough; and Xiaomin Liu for being a fantastic colleague and for helping me drag Wentao onto the Reeperbahn.

Thanks to Dmitry Turchinovich for supervision.

Also thanks to my colleagues from the other THz groups, starting with Enrique Cánovas’s group of Peng Han and Marco Ballabio; and now continuing with Hai Wang’s group of Xiaoyu Jia, Wenhao Zheng, Heng Zhang, Paniz Soltani and Lucia Di Virgilio. Especially I would like to thank to Alexander Tries for proofreading this thesis. I would also like to thank the princes of darkness from the SFG community for letting me occasionally switch the lights on in the lab.

Thanks to all the colleagues from the 11:30; 12:00 and 12:30 lunch groups for accepting me within their ranks despite my very imprecise timing.

Contents

Special thanks to my collaborators Guy Schmerber, Jacek Arabski and Eric Beaurepaire from the IPCM Strasbourg who manufactured the superb samples measured in this thesis. Their quick and exhaustive responses despite the difficult times were vital. Thanks to Tom Seifert and Julius Heitz from the Fritz-Haber institute in Berlin for sharing the iron samples with me.

I want to express great appreciation and gratitude to Laurie Gangloff. During a PhD, very often unforeseen problems suddenly arise and bad things happen. However, in our department occasionally problems suddenly disappear. In this case: Laurie happens. Thanks to the Dutchman who keeps this department running, Marc-Jan van Zadel; and thanks to Hans-Joerg Menges for keeping the lasers running and to Florian Gericke for running the 3-D printer.

I greatly enjoyed the company of my office mates in the United Offices of North Coffee Corner, and I want to thank especially the foundational members Amelie Ehrhard, Jenée Cryan, Patrick Ober, Sebastian Jäger and Jonas Pfisterer. Also thanks to my old office mates from the aquarium, especially Natalia Martín Sabanés and Vasileios Balos for finding life on MARS.

Thanks to Giovanni Giuzio for distractions and for pointing out that spectra are indeed plural.

Thanks to my fellow commuter Malte Deiseroth for interesting discussions and thanks to all the other great people who I cannot mention for the sake of brevity. To all the amazing people who helped me during this dissertation with life, the thesis and everything:

So long, and thanks for all the cake.

Abstract

This thesis demonstrates the time-resolution of the electrical conduction in 2 to 100 nm thin iron films to the point where the 7 to 30 fs short lag between applied electric field and resulting current is measured with ca. 1 fs accuracy. I achieve this time-resolution by improving the method of substrate referenced transmission terahertz time domain spectroscopy by correcting for the thickness difference between the substrate supporting the metal film and the reference substrate. The achieved time-resolution allows measuring how the lag depends on the thickness of the metal film. The significant difference between this thickness scaling of the lag and the thickness scaling of the direct current conductivity disproves Drude's assumption of a universal relaxation time, which would imply the same scaling of both quantities. Therefore, I derive a description of the conduction dynamics in the framework of the semi-classical Bloch-Boltzmann formalism, resulting in the picture of a distribution of microscopic relaxation times. This picture of a relaxation time distribution allows interpreting the observed lag in terms of the average and the variation of the microscopic relaxation times.

The accurate determination of the lag between applied field and resulting current in a metal, adds a second macroscopic observable to electronic transport and the relaxation time distribution picture relates this observable to microscopic relaxation processes in the metal. Thereby the improved substrate referenced transmission terahertz time domain spectroscopy can test microscopic theories of conduction more conclusively and will advance our understanding of transport processes in metals in general and in thin films in particular.

Kurzfassung

Diese Dissertation demonstriert die Zeitauflösung der elektrischen Leitfähigkeit in 2 bis 100 nm dünnen Eisenfilmen. Die erreichte Auflösung erlaubt den 7 bis 30 fs kurzen Zeitversatz zwischen dem angelegtem elektrischem Feld und dem resultierendem Strom mit etwa 1 fs Genauigkeit zu messen. Ich erziele diese Zeitauflösung, indem ich die Methode der substratreferenzierten Transmissionsterahertzspektroskopie verbessere. Dafür wird der Dickenunterschied zwischen dem Referenzsubstrat und dem Substrat, das den Film trägt, vermessen und der gemessene Zeitversatz um die Auswirkung des Dickenunterschieds korrigiert. Die erreichte Zeitauflösung erlaubt mir, die Abhängigkeit des Zeitversatzes von der Dicke des Metallfilms zu messen. Der signifikante Unterschied zwischen den Dickenabhängigkeiten des Zeitversatzes und der der Gleichstromleitfähigkeit widerspricht Drudes Annahme einer universellen Stoßzeit, die Leitfähigkeit und Zeitversatz gleichermaßen bestimmt. Daher leite ich eine Beschreibung der elektrischen Transportdynamik im Rahmen des semi-klassischen Bloch-Boltzmann-Formalismus her. Daraus resultiert das Modell einer Verteilung von mikroskopischen Stoßzeiten. Dieses Modell einer Stoßzeitverteilung erlaubt es, den beobachteten Zeitversatz durch den Mittelwert und die Variation der mikroskopischen Stoßzeiten zu beschreiben. Die genaue Messung des Zeitversatzes zwischen angelegtem Feld und resultierendem Strom in einem Metall fügt eine zweite makroskopische Messgröße für elektrische Transportphänomene hinzu. Das Stoßzeitverteilungsmodell verknüpft diese Messgröße mit den mikroskopischen Stoßprozessen im Metall. Dadurch kann die verbesserte substratreferenzierte Transmissionsterahertzspektroskopie mikroskopische Theorien der elektrischen Leitung aussagekräftiger testen und das Verständnis der Transportprozesse in Metallen im Allgemeinen und in dünnen Filmen im Speziellen verbessern.

My contribution to the subject

The experiments presented in this thesis are the results of a collaboration. It is a recommended practise to describe one's contribution to the subject matter of a thesis in a brief section. I will slightly deviate, and mostly name those parts I did not do on my own. The most prominent is the fabrication and characterisation of the iron films discussed in section 5.1, which was done by Eric Beaurepaire, Jacek Arabski and Guy Schmerber at the IPCM Strasbourg. The second is the measurements in series three, which were performed by Wentao Zhang. The set-up used for all terahertz measurements was designed by Zoltan Mics and built by Ivan Ivanov; therefore the description of the set-up is kept to a minimum. The basic automation giving the crucial ability to alternate reference and sample measurements was done by Zoltan Mics and improved upon by Eduard Unger and Wentao Zhang. The theoretical basics of conduction in metals were obviously not invented by me, but comparably little and only very piecewise theoretical descriptions of the dynamics of conduction existed. Compiling this information and filling some small gaps is my contribution. This allows me to highlight underlying assumptions and derive the function which defines the conduction dynamics: the distribution of microscopic relaxation times. Experimentally, the key to resolving the dynamics lay in developing a data treatment method that extracted the thickness difference between the substrate of the sample film and the bare reference substrate used. This method allowed correcting for this systematic error and achieving the time resolution necessary to time-resolve conduction in a metal. This, and all other analyses of terahertz data was done by me.

1 The concept of time-resolving conduction

1.1 Goal: Time-resolving the conduction process

The goal of this thesis is to show how conduction in metals can be time-resolved and to show what one can learn from such a measurement. To illustrate what time-resolving means, consider the following electrical circuit: a voltage source, a switch and a lamp (see fig. 1.1). Obviously, the lamp will shine some time after we close the switch. The question I am investigating here is: how long after we close will the lamp start to shine? In more physical terms: how big is the lag between an applied voltage and the resulting current? From our daily experience, we do not even notice any lag between flipping the switch and the light going on. But basic physical considerations demand a lag.

1. The charges carrying the current have mass and therefore inertia. They cannot accelerate instantaneously.
2. As long as Ohm's law applies, the electric field acting on the mobile charges must be in equilibrium with a friction force. The time it takes to establish such an equilibrium depends on the rate(s) of friction of the charges.

This second consideration means that time-resolving the conduction process will give unique insights into the dissipation processes in the material. The key difficulty is that the lag is small, on the order of 10 fs for a metal at room temperature. Developing a method to resolve such a short time difference is the first result of this thesis. To give an understanding of what exactly I try to resolve, I will introduce a formal description of time-dependent macroscopic conductivity.

1 The concept of time-resolving conduction

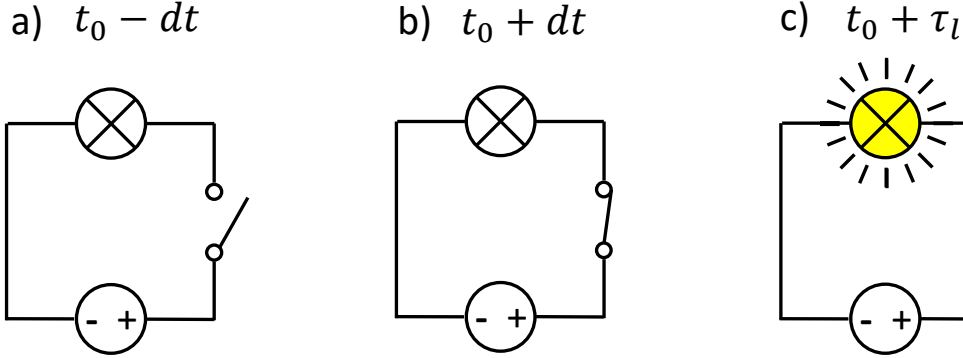


Figure 1.1: Idealised electrical circuit with a lamp responding to the closure of the switch at time t_0 . a) The circuit immediately before closing of the switch. b) The circuit immediately after closing the switch. The voltage is now applied. The charges did not yet have time to accelerate. No current is flowing. The lamp stays off. c) After a time τ_l , the charges acquired enough momentum to constitute a sizeable current. The lamp glows. The goal of this thesis is to resolve this lag τ_l .

1.2 Description of time-dependent conductivity

1.2.1 Conduction response kernel

Conduction is not instantaneous. The current will only flow after the field is applied and will continue flowing for a short time after the field is gone. This means the conduction process has a memory. The current at a certain time t_0 will depend on all values of the electrical fields at all times before t_0 . Mathematically the current density j is a convolution of the electrical field E and the conduction response function Ξ describing the system (eq. (1.1)).

$$j(t_0) = \int_{-\infty}^{t_0} \Xi(t_0 - t) E(t) dt \quad (1.1)$$

Within the scope of this thesis, I will only consider the case of the current responding linearly to the applied field; that means a response function Ξ , which does not depend on the electrical field E . Despite this, the convolution means that Ohm's law will only hold for the time averages of current and field in the time-domain. Further, the mathematical description of the time evolution with this convolution integral is quite complicated. Using a Fourier transformation to describe the conduction process in the frequency-domain transforms the convolution into a simple multiplication, thereby recovering Ohm's law.

1.2.2 Fourier transforming into the frequency-domain

We define the spectral density $\tilde{S}(\omega)$ ¹ by an integral over the time domain function $S(t)$. Another integral allows the inverse transformation from spectral density $\tilde{S}(\omega)$ back into the time domain. This is the Fourier transformation pair:

$$\tilde{S}(\omega) = \sqrt{\frac{|b|}{(2\pi)^{1-a}}} \int_{-\infty}^{\infty} S(t) e^{ib\omega t} dt \quad (1.2)$$

$$S(t) = \sqrt{\frac{|b|}{(2\pi)^{1+a}}} \int_{-\infty}^{\infty} \tilde{S}(\omega) e^{-ib\omega t} dt \quad (1.3)$$

Here $\omega = 2\pi f$ is the angular frequency, a and b are coefficients depending on convention. I use the convention $a = 0$ and $b = 1$, referred to as “modern physics convention” by Wolfram [1]. This convention is the most common in contemporary physics. Critically, since $b > 0$, a time delay results in an increase in complex phase in the frequency-domain. This is contrary to the conventions used in electrical engineering, mathematics, and mathematical optics. The frequency-domain descriptions in sources from these fields are complex conjugates of my notation. Applying this transformation to the conduction response kernel eq. (1.1) results in the frequency-domain version of Ohm’s law².

$$\tilde{j}(f) = \tilde{\sigma}(f) \tilde{E}(f) \quad (1.4)$$

\tilde{j} and \tilde{E} are the spectral densities of the current density and the electrical field. $\tilde{\sigma}$ is the complex conductivity describing the system as a function of oscillatory frequency $f = \omega/(2\pi)$. This complex conductivity is the best quantity to describe the time evolution of conduction in a material.

1.2.3 Complex conductivity

The frequency-dependent complex conductivity $\tilde{\sigma}(f)$ is conventionally displayed in terms of its real and imaginary part. This has the advantage that both dimensions of the complex quantity fit on the same graph with the same scale. However, the physical interpretation of real and imaginary part is more complicated. Expressing the conductivity $\tilde{\sigma}(f)$ in terms of amplitude $|\tilde{\sigma}(f)| = \sigma(f)$ and phase $\phi(f)$ is more intuitive. The amplitude $\sigma(f)$ answers the question: “How much current flows per unit of applied field?” and the phase $\phi(\tilde{\sigma}(f))$ tells us how the phase of this current lies with respect to the electric field $\tilde{E}(f)$. Dividing the phase by the angular frequency ω gives us the time lag τ_l between an applied field of that frequency f and the resulting current. This is what I aim to measure, hence this is my favourite way of displaying complex conductivity data.

¹I use the $\tilde{}$ to indicate complex frequency-domain quantities. It also serves to distinguish between time domain functions and their respective spectral densities, which are not the same physical quantities despite often being called the same name.

²in the presumed linear response regime

1 The concept of time-resolving conduction

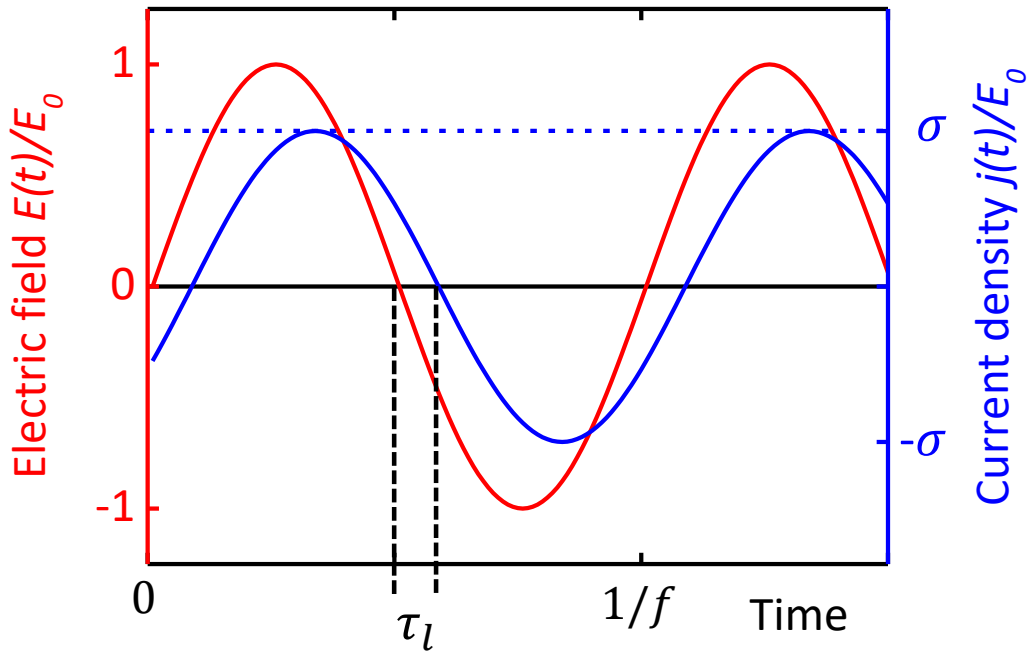


Figure 1.2: Time-dependence of a sinusoidal electric field with frequency f and resulting current density, each normalised to the amplitude E_0 of the electric field. The amplitude of the conductivity $\sigma(f)$ gives the ratio between current density and field amplitudes. The lag τ_l is the time difference between applied field and resulting current.

From this simple consideration, note that we do not have to apply a frequency similar to the inverse lag $\frac{1}{\tau_l}$ in order to resolve it. We do need to measure the phase of the current relative to the field with sufficient accuracy. This phase will increase when the frequency increases towards $\frac{1}{\tau_l}$. Therefore measuring at a higher frequency will make resolving the lag τ_l easier. To gain insight into direct current transport at room temperature, however, the energy of a quantum of electrical excitation $h \cdot f$ should not exceed the energy of typical excitations at room temperature of $\approx k_B \cdot 293K$, as I will explain in the next chapter (page 36). h and k_B are Planck's and Boltzmann's constants respectively. This limits the frequency to the range below ca. 6 THz.

1.2.3.1 Electrical conductivity of metals

The magnitude of electrical conductivity can be used to empirically classify what a metal is. To gain a general feeling for the magnitudes of conductivity we are dealing with in

1.3 Using an optical technique to measure electrical currents

metals, here is a basic overview of room temperature steady-state conductivities σ_{DC} (under ambient pressure): Silver is the most conductive material with $6.3 \cdot 10^7$ S/m [2], iron is the 22nd most conductive elemental metal at $1.03 \cdot 10^7$ S/m [3]. Niobium has one order of magnitude lower conductivity than silver at $6.6 \cdot 10^6$ S/m, similar to many alloys such as carbon steel (type 1010), and Manganese, the least conductive metal, has another order of magnitude less ($6.9 \cdot 10^5$ S/m [4]). This is still about an order of magnitude more than any non-metallic element at room temperature. Many models [5–7] of conduction in metals only predict conductivities and especially variations between conductivities of metals “within an order of magnitude”. This is not accurate enough to be useful, given that the ambient conductivities of all elemental metals and most alloys lie within an order of magnitude of Niobium.

1.3 Using an optical technique to measure electrical currents

1.3.1 Equivalence between optics and electronics

Electrical field pulses can be applied as voltages over a wire or as free space propagating electromagnetic waves. The optical and electrical descriptions are equivalent; wires can be viewed as wave-guides and air gaps as capacitative elements. In general, the higher the frequency, the more convenient the optical description becomes. To investigate the small lag between current and field, I will use optical terahertz time domain spectroscopy in this thesis. The propagation of a wave through a medium is described by the refractive index of that medium. This index is connected to the complex conductivity.

1.3.2 Refractive index, dielectric function

The current density is merely the time derivative of the electrical polarisation. The (total) complex conductivity can thus be transformed into the dielectric function $\tilde{\epsilon}$.³

$$\tilde{\epsilon}(f) = 1 + \frac{i\tilde{\sigma}(f)}{2\pi f\epsilon_0} \quad (1.5)$$

ϵ_0 is the permittivity of vacuum. The complex refractive index \tilde{n} depends on the relative dielectric function and on the relative magnetic permeability μ . At terahertz frequencies, μ is considered 1 even in magnetic metals [8,9], though data to confirm this is scarce. Hence:

$$\tilde{n}(f)^2 = \tilde{\epsilon} = 1 + \frac{i\tilde{\sigma}(f)}{2\pi f\epsilon_0} \quad (1.6)$$

³Many works separate “bound” and “free” charges, using a “background” dielectric constant for one and a conductivity for the other. I refrain from making this distinction to avoid unnecessary confusion and because the free carrier response dominates for metals in the terahertz range almost by definition.

1 The concept of time-resolving conduction

The propagation p_j of an electromagnetic field \tilde{E} through a medium over a distance x is described by the refractive index \tilde{n}_j of the medium j as:

$$\tilde{E}(\omega, x) = e^{ik\tilde{n}_j x} \tilde{E}(\omega, 0) = p_j(x) \tilde{E}(\omega, 0) \quad (1.7)$$

Here $k = \frac{\omega}{c_0}$ is the magnitude of the free space wave vector, with c_0 the speed of light in vacuum. The meaning of the real and imaginary parts of the complex index \tilde{n} are quite straight forward: $\Re(\tilde{n})$ shows how much more the phase of the field changes per distance travelled compared to vacuum. $\Im(\tilde{n})$ describes the change in the amplitude of the field. A material absorbing light of the frequency f has a positive $\Im(\tilde{n})(f)$. If the current was instantaneous, the real and imaginary parts would be almost identical. Any lag between field and current will increase the imaginary and decrease the real part of the refractive index. Figure 1.3 illustrates this by comparing the refractive index of two materials with $10.3 \cdot 10^6$ S/m conductivity. One conducts instantaneously ($\tau_l(f) = 0$), the other has a constant lag of $\tau_l(f) = 30$ fs at all frequencies.

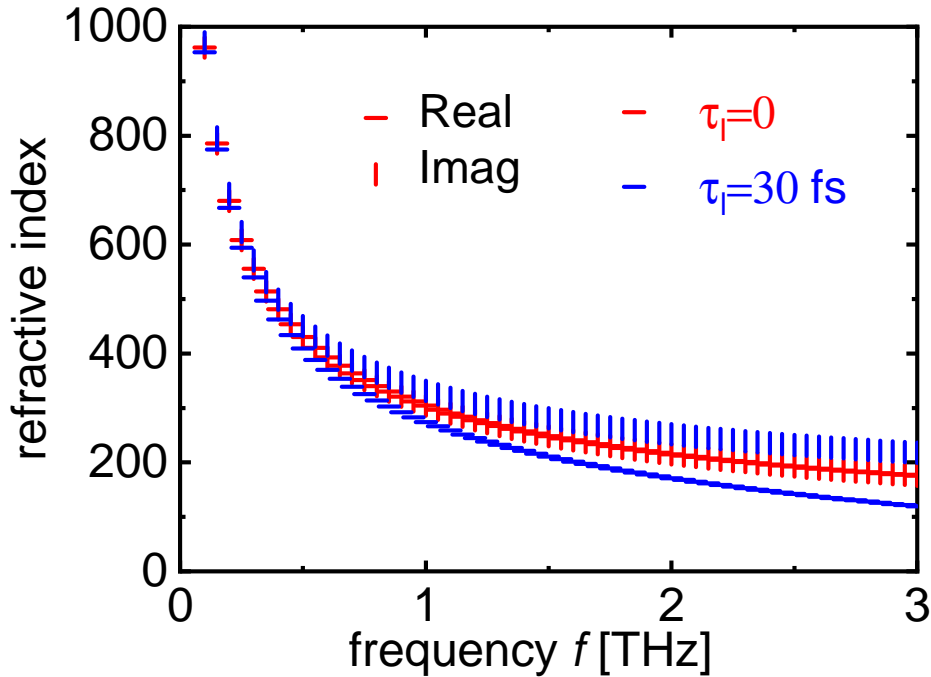


Figure 1.3: Real (-) and imaginary (|) parts of the refractive index for a $10.3 \cdot 10^6$ S/m conductive material without lag ($\tau_l=0$, red) compared to $\tau_l(f)=30$ fs of lag (blue). Without lag, real and imaginary part are virtually identical. With lag, the real part of the index decreases, the imaginary increases, while the magnitude of the index stays almost constant.

1.3 Using an optical technique to measure electrical currents

Under the unrealistic assumption of no lag between electric field and current, figure 1.4 depicts the refractive indices of iron and the most (silver) and least (manganese) conductive metals. The typical refractive index values for metals in the low THz range are on the order of 100 to 1000. This means the optical lengths $\tilde{n}x$ are roughly a factor 1000 larger than the physical dimensions x of the metal. This leads to the important observation that a metal film of 40 nm is no longer optically thin for a THz wave with 300 μm wavelength.

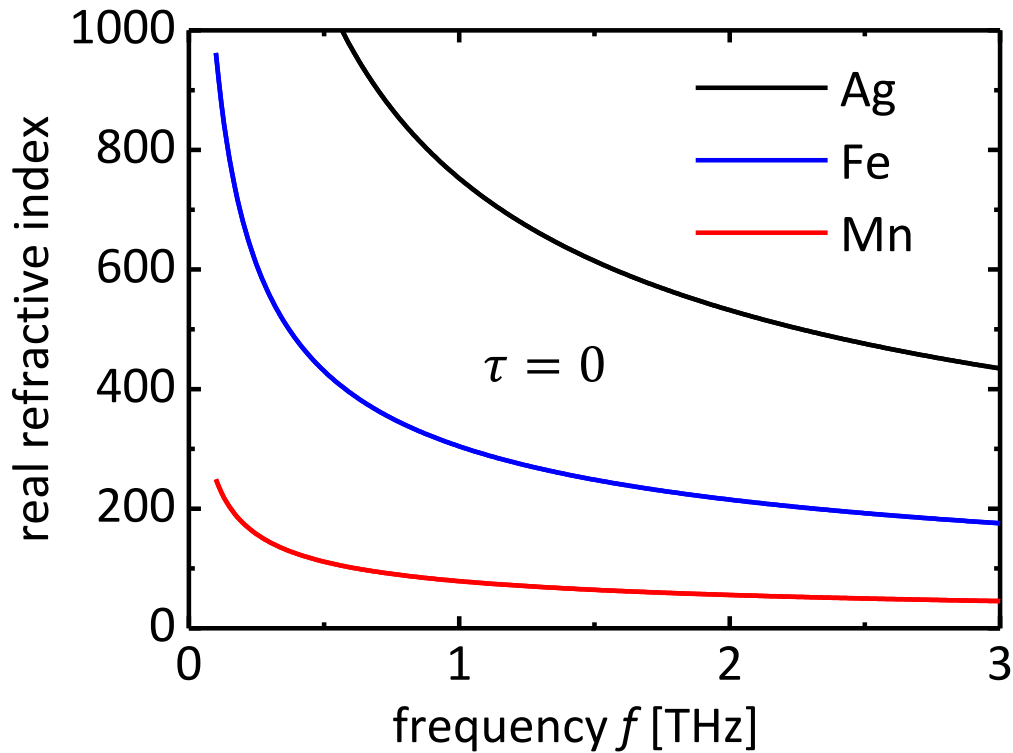


Figure 1.4: Terahertz spectra of the real part of the refractive index for three different conductivities, under the assumption of instantaneous conduction. The black curve corresponds to $63 \cdot 10^6$ S/m conductivity (bulk DC value of single-crystalline silver, the most conductive metal). Blue is for $10.3 \cdot 10^6$ S/m, which is the DC-conductivity of optimally annealed iron. Red corresponds to $6.9 \cdot 10^5$ S/m, the DC-conductivity of manganese, the least conductive metal. These refractive indices of metals are on the order of several 100 and increase with increasing wavelength. Therefore only few nanometre thin films can ever be “optically thin”.

2 Theory of electrical conduction in metals

2.1 Drude model

Only 3 years after J.J. Thompson [10] had discovered the electron, Paul Drude [11, 12] used the concept of an electron gas to describe the electrical conductivity of metals. The reasoning is quite simple: Consider a gas of n identical particles (per volume) of charge $-e$ and mass m . Drude reasoned that all valence electrons of a metal can be described this way. The particles can move anywhere in the metal like particles in a gas, but they will randomly scatter on certain obstacles in the material. Drude considered the ionic cores of metal atoms to be those obstacles. The random scattering on the obstacles causes each electron to loose velocity v at the same expected rate $\frac{1}{\tau_u}$. This friction force by scattering must be in equilibrium with the applied electric field. We can easily write down an equation of motion for such a system in an electric field E :

$$F_{el}(t) = nma(t) + \frac{nm}{\tau_u}v(t) \quad (2.1)$$

Here $a = \frac{dv}{dt}$ is the average acceleration of the particles. The electrical force F_{el} is given by $-neE$. Using these relations and Fourier transforming eq. (2.1), we obtain:

$$-en\tilde{E}(f) = -i\omega nm\tilde{v}(f) + \frac{nm}{\tau_u}\tilde{v}(f) \quad (2.2)$$

The spectral current density \tilde{j} is given by $-en\tilde{v}$. We solve eq. (2.2) for the conductivity $\tilde{\sigma}_D = \frac{\tilde{j}}{\tilde{E}}$ and obtain the frequency dependent version of Drude's result:

$$\tilde{\sigma}_D = \frac{ne^2}{m} \frac{\tau_u}{1 - i\omega\tau_u}. \quad (2.3)$$

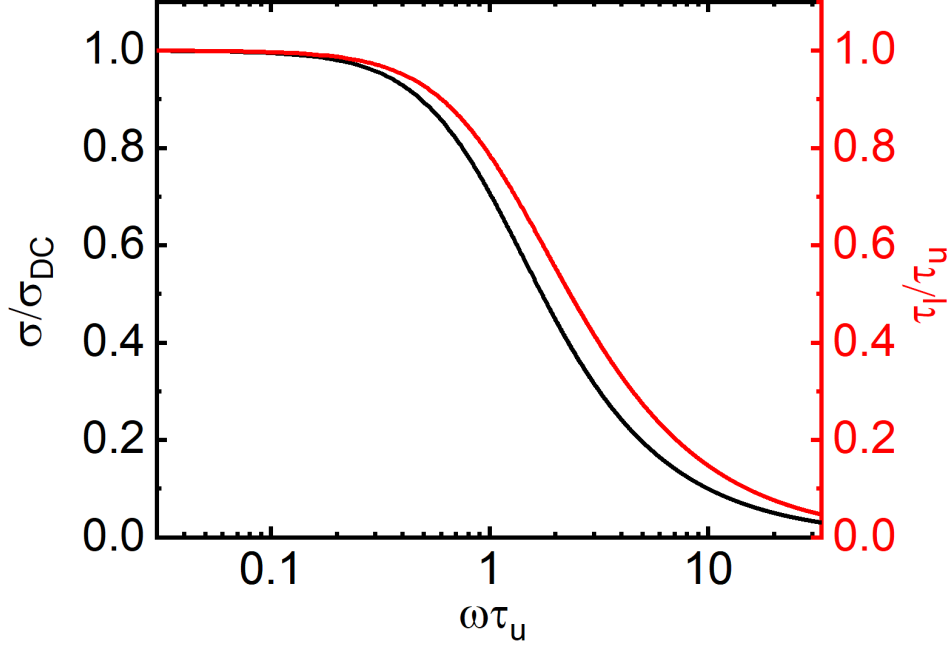


Figure 2.1: Spectrum of the amplitude σ (black, left axis) and lag τ_l (red, right axis) of the complex conductivity of the Drude model eq. (2.3). Both lag and amplitude stay constant for frequencies much lower than inverse of the universal relaxation time τ_u . The intercept values are the DC-conductivity σ_{DC} and the universal relaxation time τ_u respectively. As the (angular) frequency ω increases towards $1/\tau_u$, both amplitude and lag start decreasing; for frequencies much larger than $1/\tau_u$ they will both go to 0.

Spectra of the lag and amplitude are plotted in fig. 2.1. Drude's model gives a full description of the dynamics of conduction. Further it connects the macroscopic lag with the microscopic relaxation time of the charge carriers. Such a description and connection is what I aim for in this thesis. Looking at the dynamics in the time domain, the current response Ξ_D at time t to a field that acts at t_0 is in Drude's case is merely a single exponential decay

$$\Xi_D(t_0 - t) = \frac{ne^2}{m} \Theta(t - t_0) e^{-\frac{t-t_0}{\tau_u}} \quad (2.4)$$

The Heaviside function Θ enforces causality, i.e. the current only flows after the time of excitation t_0 .

However, Drude's model is outdated, because most of his assumptions have been by now proven wrong, for metals at least. Drude obviously had no way of knowing that electrons are fermions. Sommerfeld [13] did show that one obtains the same formula (though

2.1 Drude model

with potentially different parameters) when considering the electrons to follow the Fermi-Dirac distribution rather than the Maxwell-Boltzmann distribution of classical particles in a gas, as long as all particles relax momentum identically. With the Bragg’s discovery that metals are crystals and Bloch’s description of quantum states in a crystal, mass and number density had to be replaced by a combination of density of states and group velocity. The spectral shape stayed identical, as long as all electrons were considered to relax equally. Bloch also showed that the electrons would not scatter in a perfect crystal. Electrons only scatter when they encounter some deformation of the crystal potential in form of a defect or a phonon. As long as these scattering events still scatter every electron equally and randomly, the dynamics stay the same. A crystal is not isotropic, so the group velocity will usually depend on direction. For bulk conductivity, the average velocity can be used and the time dependence will stay the same as Drude’s as long as all electrons have the same relaxation time. Therefore, Drude’s description of electron dynamics is still very often used, both for the optical conductivity of metals [14, 15] and the terahertz (photo-)conductivity in long relaxation time materials such as semiconductors [16] and graphene [17]. The empirical observation of Drude-type dynamics is not surprising, since a single exponential decay eq. (2.4) describes or at least approximates many, if not most, relaxation processes in nature.

The problem with Drude’s assumption that all electrons relax the same way is: electrons are fermions. Every fermion in a system differs by at least one quantum number from every other. In a metal, we have typically 1 itinerant electron per atom. The electrons must, therefore, differ a lot among the very large population. The assumption that these differences between the electrons have no effect on their relaxation is not justified and has been disproven for several cases [5, 18–22]. But how do the dynamics look like when different electrons have different relaxation times? To illustrate, let us consider the next simplest case to all electrons having one universal relaxation time: two relaxation times. We assume a system comprised of two species of electron, each with their own relaxation time. One species is named “dash”; the other “dot”. The conductivity of each species is given by the classical Drude model eq. (2.3). Species “dot” has twice as many electrons as “dash”, but only a quarter of the relaxation time. Both have the same mass. The combined conductivity is the sum of both conductivities $\tilde{\sigma}_{dash}$ and $\tilde{\sigma}_{dot}$. It is plotted in fig. 2.2.

We can see that the amplitude of the total conductivity is merely the sum of the dash and dot conductivities. The lag, however, is neither the sum nor the mean of both lags τ_{dash} and τ_{dot} . At low frequencies, an effective single Drude model can approximate the total conductivity. Its DC-conductivity is obviously the sum of the two constituent DC-parameters. The response time in this effective Drude model is more complicated. I refer to this effective Drude parameter as current response time τ_C . The current response time is an average of the relaxation times of the species weighted by their respective conductivities. This weighted average will always be larger than the “normal” average, and the distance to the normal average will grow with increasing difference between the two relaxation times. We will see in the following chapter that the low-frequency limit in the more accurate Bloch-Boltzmann formalism can still be

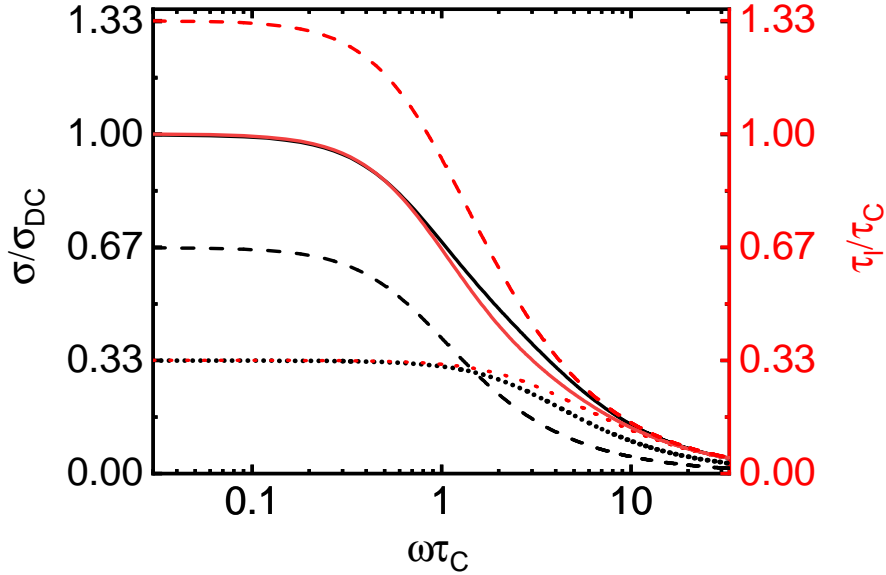


Figure 2.2: Spectrum of the amplitude σ (black, left axis) and lag τ (red, right axis) of the combined complex conductivity of two electron species “dash” and “dot”. The spectrum of the combined ensemble is shown as full lines, the two individual components as dashed and dotted lines, respectively. As in the single Drude picture in fig. 2.1, both lag and amplitude are constant for low frequencies ω . The y-intercepts are named DC-conductivity σ_{DC} and in this case current response time τ_C , as a universal relaxation time no longer exists. When approaching frequencies around $1/\tau_C$, the combined spectrum differs from the single Drude version, while still decreasing towards 0. Note that the DC-conductivity is merely the sum of the DC-conductivities of the components, while the current response time is an average of the response times of the components weighted by their contribution to conductivity.

described by a Drude spectrum and the current response time of this spectrum will still be a weighted average in the general case of an unknown distribution of relaxation times. In the case of a general distribution, the standard deviation of that distribution will be the measure that determines how different the relaxation times are and how much the weighted average of the relaxation times τ_C surpasses the “normal” average relaxation time.

2.2 Semiclassical Bloch-Boltzmann theory

The current theoretical framework describing conduction by electrons in metals is often referred to as Bloch-Boltzmann theory. The quantum mechanical description of

2.2 Semiclassical Bloch-Boltzmann theory

the electronic states as Bloch waves yields their dispersion relation. The dispersion relation describes the combinations of momentum and energy an electron can have. The Fermi-Dirac distribution then allows assessing how likely those states are occupied based on their energy. The occupied states can be represented as a phase space density function. From this point on, the electron system is treated as if the electrons were particles in a classical gas. The non-equilibrium behaviour of such a gas is described by the Boltzmann transport equation of the phase space density. The key ingredient of this equation is called collision integral, which accounts for the relaxation of the gas by scattering processes. Within the assumptions of identical particles, isotropy, small deviations from equilibrium, and elastic scattering, the collision term simplifies to a single time constant. This time constant is referred to as collision time, scattering time, mean free time or relaxation time of the ensemble. This time constant is both the expectation value of the microscopic time within which a single particle loses its momentum as well as the time it takes the entire ensemble to settle from one steady-state into another. Further the external force needed to drive the system out of equilibrium is directly anti-proportional to this time constant.

However, in metals there is more than one type of electron or electronic states with different momenta or spins relaxing at different speeds, therefore the relation between the macroscopic responses and the now various microscopic relaxation times becomes more complicated. It is not even directly obvious that a single macroscopic response time exists. My contribution to the solution to this problem is demonstrating that a single time constant defines the dynamics for low-frequency excitations and showing how this macroscopic time constant and the conductivity are connected to the distribution of microscopic scattering times. Therefore, I will proceed in the following order:

I will give a qualitative overview of the dispersion relation of Bloch waves, also known as band structure. Here I loosely follow the book of Abrikosov [7] and the overview by Pippard [23]. From there, I will show how to quantitatively connect the microscopic electronic structure and scattering with the macroscopic current and its dynamics via the Boltzmann transport equation. Then I will motivate that any more complicated collision term depending on properties of the electrons (such as spin, angular momentum, momentum or position or a combination thereof) can be approximated by relaxation times depending on these properties. Hence we can describe the conduction process as superposition of conduction channels of different relaxation times. I will show that the macroscopic conductivity dynamics of such a system with a distribution of microscopic relaxation times can be described by a single macroscopic current response time for slowly varying excitations. This current response time depends on the average and the standard deviation of the microscopic relaxation times, whereas the macroscopic DC-conductivity only depends on the average. The ratio of response time and DC-conductivity will depend on the standard deviation relative to the average. Therefore I can use this ratio to track the evolution of the variation when the scattering changes, which I will use to analyse the experimental results in the chapter "conduction dynamics in thin iron films". I will wrap up by discussing a few key assumptions of my relaxation-time-distribution model, some of the previous experiments showing the distribution of

microscopic relaxation times and previous frame works they were described in.

2.3 Bloch waves: electronic band structure in a crystal

2.3.1 Reciprocal lattice of a crystal

A crystal is a system whose microscopic constituencies are periodically ordered. Therefore the crystal can be described as a lattice of identical cells; the smallest of such cells are called unit cells. Each point in the lattice can be described by the position in a unit cell and a discrete number of translations of that unit cell. This is also called discrete translational symmetry. We can define such a unit cell by one vector per dimension, i.e. $\vec{a}_1, \vec{a}_2, \vec{a}_3$ in 3D. All physical properties of the crystal have the same periodicity as the crystal. A Fourier transformation simplifies the mathematical description of periodicity by transforming from real into reciprocal/Fourier space. The Fourier transformation allows even the longest range phenomena to be mapped into the unit cell of the lattice in reciprocal space. The vectors defining the reciprocal lattice in the 3D case are $\vec{K} = \vec{K}_1, \vec{K}_2, \vec{K}_3$. They can be derived from the real space lattice vectors. There is some choice in the shape of the unit cell. For the following, I consider the cell constructed by Voronoi partition, which is called Wigner-Seitz cell in the real lattice and Brillouin zone for the reciprocal lattice. A few general remarks about the symmetry properties of the crystal are that it by definition has discrete translational symmetry and may have discrete rotational symmetry, i.e. between directions \vec{b}_1, \vec{b}_2 . It can never have continuous rotational symmetry (also known as radial symmetry). In terms of unit cells, this can be understood, as these cells must be polygons, not spheres. That means the crystal lattice is by definition anisotropic. I point this out as the assumption of isotropy is often used in the (basic) theoretical description of conduction in crystalline solids. This assumption is usually rather motivated by the desire for simplicity than by physical reality.

2.3.2 Free electron gas

The Schroedinger equation (or even Dirac equation) can be written down for a single electron a system with N other charged particles.

$$\frac{\hat{p}^2}{2m}\psi + \sum_{i=1}^N V(r - r_i)\psi = \mathcal{E}\psi \quad (2.5)$$

Here \hat{p} is the momentum operator, ψ the wave function of the electron, m the electron mass, \mathcal{E} its energy, V the potential and r the position of the electron. The challenge in solving this equation is that the potential for a charged particle will depend on the positions r_i of all other charged particles, as the Coulomb interaction is long range. This interaction couples the solutions of each particle, such that one cannot easily find the solution for a single particle without solving for all particles, which is generally too complicated.

2.3 Bloch waves: electronic band structure in a crystal

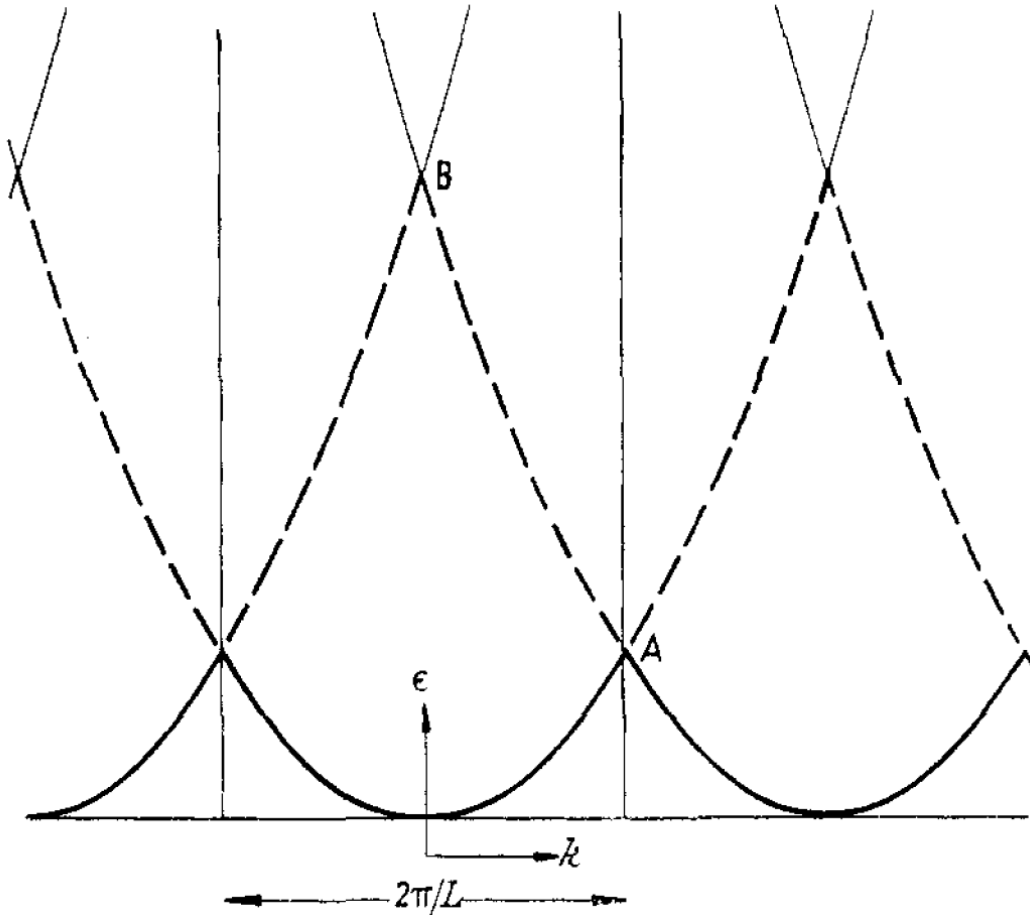


Figure 2.3: Sketch of the one-dimensional dispersion relation in the nearly free electron or Sommerfeld model, taken from Pippard [23]. Pippard uses L for the real space lattice constant. $k = p/\hbar$ is the coordinate in reciprocal space. Where the dispersion relation curve leaves the first Brillouin zone (which is a unit cell in reciprocal space), a curve from the neighbouring unit cell must also enter at the same point. Thereby dispersion in every cell can be mapped onto a single unit cell, the first Brillouin zone.

However, two theorems help to recover most of the information we need. First is the use of the symmetry in a crystalline system, which requires the single-particle solutions to be Bloch waves. Second is Landau's (proven) hypothesis [24] that a system of coupled fermions around its Fermi edge will behave like a system of uncoupled fermions (with potentially different group velocities) for a suitably chosen Fermi level of the uncoupled system. In practise this means the electronic structure can be calculated for a non-interacting electrons first and the interaction can be taken into account later by "renormalising" some properties like the group velocity by Landau parameters. So, let us consider a system of electrons not interacting with each other. Further, I assume

2 Theory of electrical conduction in metals

no interaction with the lattice of nuclei. This the free electron gas. The dispersion relation $\mathcal{E}(\vec{p})$ is given by:

$$\mathcal{E}(\vec{p}) = \frac{\vec{p}^2}{2m} \quad (2.6)$$

Here \vec{p} is the momentum of the electronic states.

2.3.3 The nearly free electron model

The next step is to impose the periodicity of the crystal lattice on the dispersion relation. The dispersion relation is folded back into the first Brillouin zone. This is the nearly-free electron model [23]. The momentum \vec{p} is now replaced by the quasi momentum (I still use \vec{p} to denote it). The quasi momentum is only defined up to multiples of the reciprocal lattice vectors. $p_i = p_i + n\hbar K_i$. This nearly-free electron model already gives rise to the complication that the band structure cannot be isotropic any more. The reason is: even when the dispersion relation is isotropic before it reaches the Brillouin zone boundary, the distance to the boundary is not isotropic since the Brillouin zone is not a sphere. Therefore the folding points are not isotropic. The dispersion relation can only ever be isotropic over a limited range of energies.

2.3.4 Band bending/Bragg reflection

When the potential $V(\vec{p})$ is different from 0 at the Brillouin zone boundary $\vec{p} = \hbar\vec{K}$ (point A in Pippard's sketch, shown in fig. 2.3), the electronic states close to the boundary must be stationary because they would undergo Bragg reflection in the crystal lattice if they had a finite group velocity. This band bending makes the band parabolic around the Brillouin zone boundary. The same holds for point B in Pippard's sketch fig. 2.3 at $\vec{p} = 0$, where an extremum must lie when the Fourier transformed potential at $V(\hbar 2\vec{K})$ is non zero.

2.3 Bloch waves: electronic band structure in a crystal

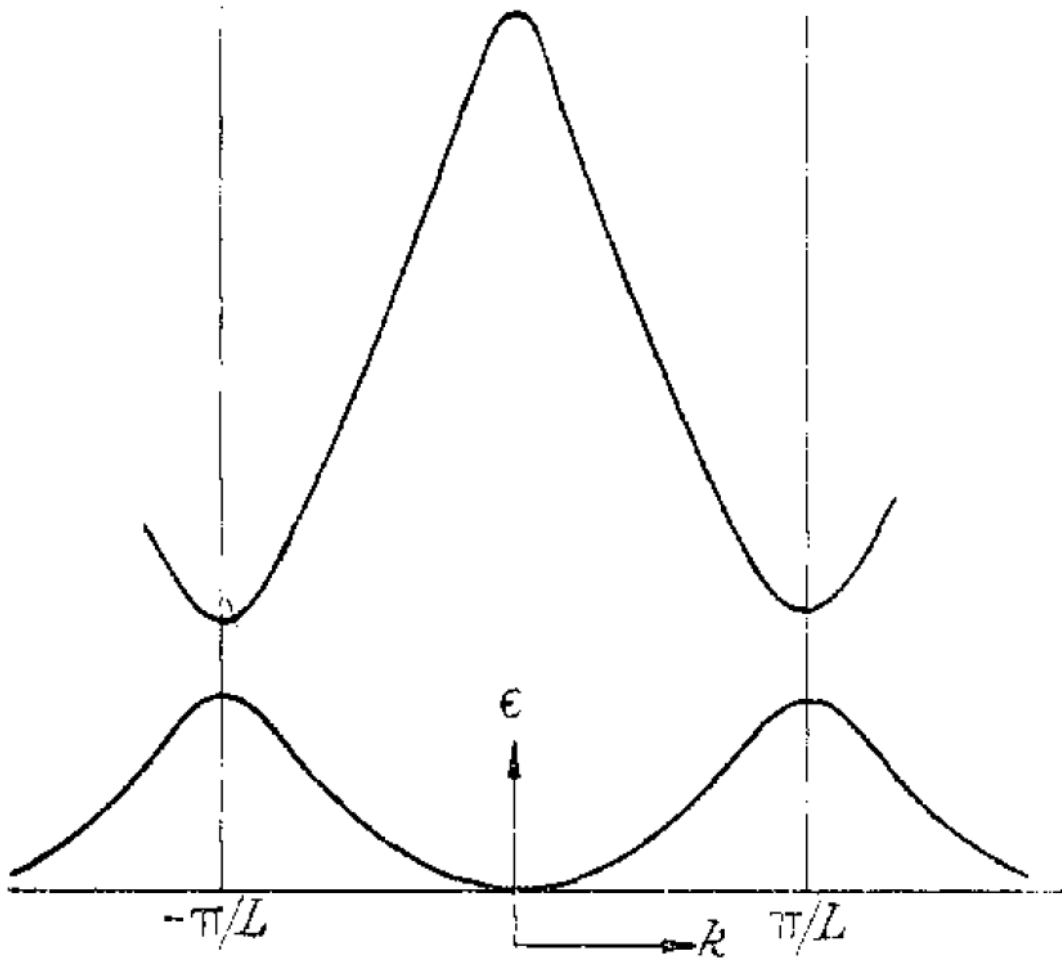


Figure 2.4: Sketch of the general one dimensional dispersion relation for almost free electrons in a periodic potential, taken from Pippard [23]. $k = p/\hbar$ is the coordinate in reciprocal space. The periodic potential causes band bending at the Brillouin zone boundary and at $k = 0$. At these points extrema occur, with parabolic band structure.

2.3.5 General band structure of a metal

The general shape of a band can be locally approximated by the above-mentioned models, as long as we take the mass in eq. (2.6) as a potentially direction dependent parameter rather than a constant. Locally, around a certain energy, the dispersion relation can be approximated by a Taylor series expansion. As long as the energy range considered is small enough, the dispersion can be classified by the order of the first term in this expansion. The extrema of a band (usually at $\vec{K} = 0$ and the Brillouin Zone boundary) do not have a first-order term, so here the energy-momentum relation is

2 Theory of electrical conduction in metals

quadratic. Away from the extrema, the first-order term will suffice, and the dispersion is locally linear. This approximation is best for the middle of a band. For almost all metals, the Fermi energy lies in the middle of at least one band. Therefore the dispersion in metals is usually linear close to the Fermi edge.

2.3.6 Fermi energy and surfaces

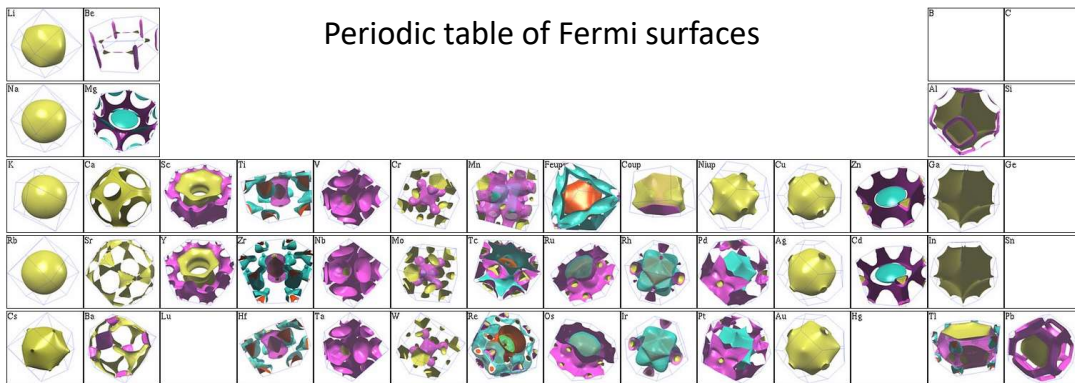


Figure 2.5: Periodic table of the Fermi surface of crystalline metals. The colours indicate different bands. With the potential exception of Potassium, none of the surfaces appears isotropic, that is spherical. Images taken from the university of Florida website [25,26], http://www.phys.ufl.edu/fermisurface/periodic_table.html.

I have by now mentioned that only the electronic states close to the Fermi energy are relevant for conduction. The detailed reason why only these states contribute is given on page 36 in eq. (2.27). Here I will just explain the Fermi-Dirac statistics, and define the terms chemical potential, Fermi energy and Fermi surface.

Any particle of half-integer spin is a fermion. No two fermions in a system can have the exact same state; at least one quantum number must be different between any two fermions. Therefore the fermions cannot all condense into the state of lowest energy in a system, rather they fill up all states up to a certain energy (at 0 Kelvin). This energy is called Fermi energy \mathcal{E}_f . At finite temperatures, the occupation probability g of a state of energy \mathcal{E} is given by the Fermi distribution:

$$g(\mathcal{E}) = \frac{1}{e^{\frac{\mathcal{E}-\mu}{k_B T}} + 1} \quad (2.7)$$

k_B is Boltzmann's constant, and μ is the chemical potential. At temperature $T = 0$, the chemical potential and the Fermi energy are identical, at higher temperatures they might differ, but for room temperature in metals, this difference is small.

The electronic structure is usually displayed in terms of the dispersion relation $\mathcal{E}(p)$ along a certain axis, for example in fig. 2.4. Since we know that only the states close

2.4 Boltzmann equation: The role of scattering in transport

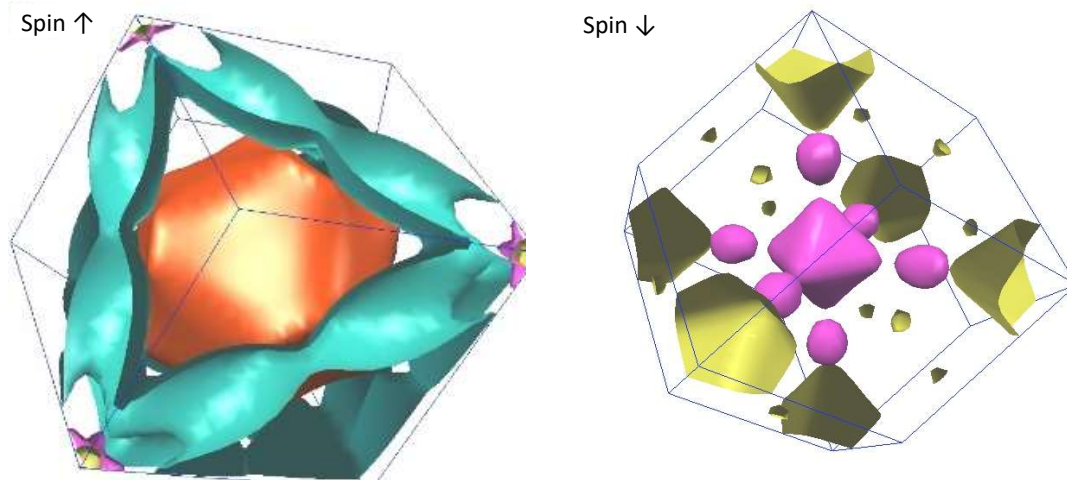


Figure 2.6: Fermi surface for iron spin- \uparrow (left) and spin- \downarrow (right). Different colours represent different bands. Iron has one of the most complicated Fermi surfaces, with 6-8 bands (depending on assignment) at the Fermi surface. Images taken from the university of Florida website [25,26].

to the Fermi energy contribute to conduction, the surface of all states at the Fermi energy in reciprocal space is a key property to consider for a metal. This surface is called Fermi surface. Fig. 2.5 gives an overview of the Fermi surfaces of most metals. The spin-split Fermi surface of iron is illustrated in fig. 2.6.

2.4 Boltzmann equation: The role of scattering in transport

2.4.1 Scattering processes

Bloch waves will not scatter in a perfectly periodic potential. Any distortion of the lattice however, may scatter them. Two sources of scattering are usually distinguished: Thermal vibrations of the lattice (phonons) and defects in the structure, comprising interstitials, vacancies, grain boundaries, dislocations, impurities and possibly more microscopic sources. I focus on the overall rates of scattering, rather than its microscopic sources. In principle, all the above sources can be expressed in terms of a scattering potential or cross section. The probability of a (quasi-)electron scattering on any of those obstacles will depend on the cross section of an obstacle, but it is also proportional to the number of unoccupied states to scatter into, also known as the available phase space. The more unoccupied states, the more scattering. This is the reason metals typically have an order of magnitude shorter relaxation times than (doped) semiconductors: the number of unoccupied states close to the Fermi surface is 10^5 to 10^{10} times higher in metals. In the following, all scattering processes will be summed up in the collision

2 Theory of electrical conduction in metals

term of the Boltzmann equation eq. (2.8).

2.4.2 From Bloch waves to quasi-particle plasma

The Landau hypothesis allows treating the strongly interacting electrons as a gas of non-interacting quasi-particles. Note: The non-interacting part holds only for the microscopic interactions and phase relations. When the particles accumulate, we still have to take into account that they are charged and therefore change the electrical potential. This allows describing the electronic system in terms of a classical plasma, albeit with a dispersion relation derived from Bloch's quantum mechanical picture, expanded by Landau's Fermi liquid parameters and obeying Fermi-Dirac statistics. The dispersion relation gives all possible states in phase space (p^3x^3). The state of the plasma is described by its phase space density $g^{(b,s)}(\vec{p}, \vec{x})$. Here b and s indicate the band and spin of the electrons, as each band and (in magnetic materials) each spin will have a different dispersion relation. Boltzmann's kinetic equation describes the plasma taking into account external forces and dissipation by collisions.

$$\frac{\partial g^{(b,s)}}{\partial t} + \frac{\partial g^{(b,s)}}{\partial \vec{x}} \vec{v}_g^{(b,s)}(\vec{p}, \vec{x}) + \frac{\partial g^{(b,s)}}{\partial \vec{p}} \vec{F}(\vec{x}, t) = I_C^{(b,s)}(\vec{p}, \vec{x}, g^{(b,s)}) \quad (2.8)$$

Here t is time, \vec{F} is the total force, $\frac{\partial}{\partial \vec{x}}$ and $\frac{\partial}{\partial \vec{p}}$ are the gradients with respect to spatial and momentum coordinates and I_C is the collision integral. Since we are interested in electrical conduction, we consider only the electrical force $\vec{F} = -e\vec{E}$ on the quasiparticles of charge e . Since the particles are charged, the electric field $\vec{E}(x)$ will depend on the particle density $\rho(x)$, which is the integral $\int_{Bz} g^{(b,s)} \frac{dp^3}{h^3}$ of the phase space density g over the entire Brillouin zone (normalised by Planck's constant h). This makes the equation extremely complicated to deal with.

2.4.3 From plasma to gas

With a few assumptions we can simplify the description of the plasma to that of a gas. First, the phase space density can be written as a combination of an equilibrium density $g_0^{(b,s)}$ and a perturbation $g_1^{(b,s)}$ as response to an external force; $g^{(b,s)} = g_0^{(b,s)} + g_1^{(b,s)}$. Now, when the system is spatially homogeneous, $g_0^{(b,s)}$ and $I_C^{(b,s)}$ will not depend on position \vec{x} . Further, the perturbation of the density $g_1^{(b,s)}$ is assumed to be small and locally spatially homogeneous, which can be justified when the external field \vec{E} varies little along the direction it acts. This means we now treat the electron system like a very compressible gas, because we assume that no compression should occur in a homogeneous system.¹

¹The fact that the non-interacting quasi-electrons are still charged and form a plasma rather than a gas seems to me somewhat ignored in many discussions of transport in metals [7, 27].

2.4.4 Collision integral to relaxation times

With the above assumptions, Boltzmann's equation simplifies to:

$$\frac{\partial g_1^{(b,s)}}{\partial t} - e \frac{\partial g_0^{(b,s)}}{\partial \vec{p}} \vec{E}(\vec{x}, t) = I_C^{(b,s)}(\vec{p}, g_1^{(b,s)}, t) \quad (2.9)$$

To solve Boltzmann's transport equation (eq. (2.8)) for the response g_1 to the external field \vec{E} we need to know the collision integral I_C .

2.4.4.1 Relaxation times assumption

A simple form of the collision integral is

$$I_C^{(b,s)} = -\frac{g_1^{(b,s)}(\vec{p}, t)}{\tau^{(b,s)}(\vec{p})}. \quad (2.10)$$

Here τ is the relaxation time. This time can depend on spin, band and momentum. To distinguish this assumption from the assumption of a single, universal relaxation time, I refer to it as relaxation times assumption. This "relaxation times form" of the collision integral is quite often just assumed rather than derived [23] and quite often motivated by convenience rather than physical considerations².

However, there are several different sets of assumptions that justify eq. (2.10). Ashcroft and Mermin [27] give the following set of assumptions

1. "The distribution of electrons emerging from collisions at any time does not depend on the structure of the non-equilibrium distribution function just prior to the collision." In other words, the collisions are a memory-free process, that is a Poisson process. Such processes are also assumed for example in Brownian motion [28].
2. "If the electrons in a region ... have the equilibrium distribution appropriate to a local temperature, then collisions will not alter the form of the distribution function." Basically the collisions will maintain or restore thermal equilibrium.
3. Small electric and magnetic fields.

Point 3 will be fulfilled, I will go into detail what "small" means for a metal on page 43. Point two is also physically reasonable, since the collision integral sums up all dissipation processes. Point one remains as a critical assumption.

Similarly, eq. (2.10) can be vindicated if the scattering is assumed to be isotropic [7, 27]. I strive to put the relaxation times approach on a more general and formal footing, since this is key to describing the time dependence of conduction.

²"As a result the displacement at any region of the Fermi surface ultimately reaches a steady limit, and it is not uncommon to assume for convenience that the approach to the limit is exponential" [23]

2.4.4.2 Relaxation times approximation

The problem is that the collision term is the integral I_{In} over all electrons scattering from other states \vec{p}' into a state \vec{p} minus all electrons I_{Out} scattering out of of state \vec{p} into any other state \vec{p}' . Therefore the distributions $g^{(b,s)}(\vec{p}')$ of all states \vec{p}' influence the dissipation of $g^{(b,s)}(\vec{p})$ at position \vec{p} . Mathematically, the collisions couple all states within the entire momentum space. In tune with the red line of the previous derivations, we search for a way to decouple the system.

$$I_C^{(b,s)} = I_{\text{In}}^{(b,s)} - I_{\text{Out}}^{(b,s)} \quad (2.11)$$

$$I_{\text{Out}}^{(b,s)} = \sum_{b',s'} \int \left(\frac{dp'}{h} \right)^3 g^{(b,s)}(\vec{p}, t) V_{\vec{p},b,s,\vec{p}',b',s'} (1 - g^{(b',s')}(\vec{p}', t)) \quad (2.12)$$

$$I_{\text{In}}^{(b,s)} = \sum_{b',s'} \int \left(\frac{dp'}{h} \right)^3 g^{(b',s')}(\vec{p}', t) V_{\vec{p}',b',s',\vec{p},b,s} (1 - g^{(b,s)}(\vec{p}, t)) \quad (2.13)$$

Here $V_{\vec{p},b,s,\vec{p}',b',s'}$ is the probability for an electron occupying state $\{\vec{p}, b, s\}$ to scatter into an unoccupied state $\{\vec{p}', b', s'\}$. I will briefly simplify the notation, using $g'(t)$ for $g^{(b',s')}(\vec{p}', t)$ as well as $V \equiv V_{\vec{p},b,s,\vec{p}',b',s'}$; $V' \equiv V_{\vec{p}',b',s',\vec{p},b,s}$. Further $g(t)$ is expressed in terms of g_0 and g_1 . I further will refrain from explicitly stating the sum over all bands b' and spins s' .

$$I_{\text{Out}} = \int \left(\frac{dp'}{h} \right)^3 V (g_0(1 - g'_0) + g_1(t)(1 - g'_0) - g_0 g'_1(t) - g_1(t) g'_1(t)) \quad (2.14)$$

$$I_{\text{In}} = \int \left(\frac{dp'}{h} \right)^3 V' (g'_0(1 - g_0) + g'_1(t)(1 - g_0) - g'_0 g_1(t) - g'_1(t) g_1(t)) \quad (2.15)$$

By the previous assumption of spatial homogeneity, $I_C(\vec{p}, g)$ must be 0 in equilibrium, that is when $g = g_0$. Further, the density of excited states g_1 is considered small compared to the equilibrium densities g_0 and $1 - g_0$ of occupied and unoccupied states. Therefore the product $g'_1 g_1$ can be neglected. Using this when inserting eqs. (2.14) and (2.15) into eq. (2.11) yields

$$I_C = \int \left(\frac{dp'}{h} \right)^3 V' (g'_1(t)(1 - g_0) - g'_0 g_1(t)) - V (g_1(t)(1 - g'_0) + g_0 g'_1(t)) \quad (2.16)$$

$$I_C = \underbrace{-g_1(t) \int \left(\frac{dp'}{h} \right)^3 (V' g'_0 + V(1 - g'_0))}_{I_1} + \underbrace{\int \left(\frac{dp'}{h} \right)^3 g'_1(t) (V'(1 - g_0) + V g_0)}_{I_2} \quad (2.17)$$

The first integral I_1 contains change in scattering at \vec{p} due to the perturbation g_1 at point \vec{p} . It has the form of the relaxation time approximation. The second term I_2

2.4 Boltzmann equation: The role of scattering in transport

describes the change in scattering due to the perturbation at all other momenta \vec{p}' . The following observations can be made: $\int \left(\frac{dp'}{h}\right)^3 g_1'(t)$ must be 0 due to the conservation of phase space density (conservation of particles). $g_1(\vec{p})$ will be antisymmetric along an axis defined by the external field. g_0 should be symmetric. If V and V' are also symmetric along this axis, the entire integral I_2 will cancel. This is basically the Poisson process case. Otherwise I_2 will only partially cancel. This will still make I_2 smaller than $I_1 \cdot g_1(\vec{p})$, except the cases of points \vec{p} in phase space where g_1 is particularly small. Since such points contribute little to the overall excitation dynamics, we can disregard these cases. Since we can assume $g_1(\vec{p}', t)$ and $g_1(\vec{p}, t)$ to be linear responses to the same field. We can write $g_1(\vec{p}', t) = a(\vec{p}', t)g_1(\vec{p}, t)$. We can express I_2 in this notation

$$I_2 = g_1(t) \int \left(\frac{dp'}{h}\right)^3 a(t)(V'(1 - g_0) + Vg_0). \quad (2.18)$$

When the relaxation dynamics are isotropic, $a(\vec{p}', t)$ is time independent and the integral can be added to I_1 to compute the relaxation time. When the system reaches a non-equilibrium steady state $a(\vec{p}', t)$ will reach the steady state value $a_0(\vec{p}')$. Unless the relaxation times are differing extremely, we can express $a(t) = a_0 + \delta a(t)$, where $\delta a(t)$ is a small time dependent perturbation. This will work at least in the ‘‘almost steady’’ case of low frequencies compared to the relaxation rates.

$$\begin{aligned} I_C = & -g_1(t) \int \left(\frac{dp'}{h}\right)^3 (V'g_0' + V(1 - g_0')) \\ & + g_1(t) \int \left(\frac{dp'}{h}\right)^3 a_0(V'(1 - g_0) + Vg_0) \\ & + g_1(t) \int \left(\frac{dp'}{h}\right)^3 \delta a(t)(V'(1 - g_0) + Vg_0) \end{aligned} \quad (2.19)$$

The first two terms can be combined into a relaxation time because they are independent of time t . The third term will only be a small correction to the second, and the second is smaller than the first in all points that matter for conduction, hence discarding the third term is justified in most cases. The key difference of this motivation for the relaxation times approximation to derivations like that presented by Ashcroft and Mermin [27] is that I do not have rather unrealistically assume that the perturbation g_1 only changes I_{Out} but not I_{In} . I would also like to remind that the relaxation time $\tau(\vec{p})$ given by

$$\tau(\vec{p}) = - \left(\int \left(\frac{dp'}{h}\right)^3 (V'g_0' + V(1 - g_0')) - \int \left(\frac{dp'}{h}\right)^3 a_0(V'(1 - g_0) + Vg_0) \right)^{-1}, \quad (2.20)$$

is the time constant describing the exponential relaxation of the distribution $g(\vec{p})$ towards any steady state. It is not the microscopic mean free time between collisions,

2 Theory of electrical conduction in metals

since the number of collisions (per electron) needed to establish a steady state depends on the microscopic scattering mechanism. This relaxation time is a mesoscopic constant which may sum up any number of microscopic interactions. From now on, I will resume writing band and spin indices and the sum over them explicitly.

The above treatment arrives at the same definition of the anisotropic relaxation time as Sorbello [29]. Sorbello showed that this definition of the anisotropic relaxation time is physically meaningful, rather than merely a parameter in the theory with the dimension of time. It describes the relaxation dynamics at the start of the transition between a non-equilibrium steady-state and equilibrium. However, we have to note that as long as integral I_2 contributes, the relaxation time will depend on the type of excitation shaping $a(\vec{p}')$. I present an alternative, less formal derivation of the relaxation times assumption in section 7.1.

2.4.4.3 Relaxation times for specific excitations

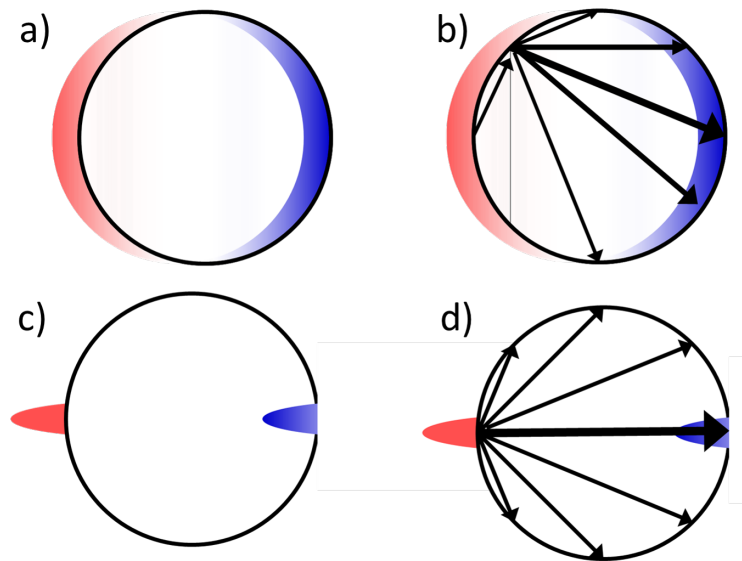


Figure 2.7: Sketch of the influence of the excitation type on the relaxation time. The Fermi surface is idealised as a black circle. Regions, where the density of states is increase by the excitation (positive g_1) are coloured red, decreased density depicted in blue. Panels a) and b) show the excitation by an electric field, c) and d) the excitation of a certain point/orbit on the Fermi surface. The black arrows in sketch b) and d) illustrate the net transfer of electrons between a selected point and the rest of the Fermi surface by scattering. Thicker arrows allude to higher rates. Key here is that due to the different final densities of states, the transfer rates and therefore the relaxation times may be different between the normal electrical excitation and the point excitation.

2.4 Boltzmann equation: The role of scattering in transport

In the relaxation times approximation eq. (2.20), the relaxation time at each point depends on the shape a_0 of the excited phase space density g_1 . Therefore a process exciting different regions of the phase space density may result in different relaxation times $\tau(\vec{p})$. Figure 2.7 depicts sketches of the excitation for a DC electric field and a single point excited by a resonance. Unfortunately, these might not be identical to the relaxation times relevant for electrical conduction [22].

2.4.5 From relaxation times to conductivity

So far, a classical phase space density g has been constructed from the quantum-mechanical electron dispersion relation and Fermi-statistics and relaxation times $\tau^{(b,s)}(\vec{p})$ have been derived to sum up the effects of microscopic scattering events on the phase space density g . Now we need to derive the macroscopic conductivity from the phase space density and the relaxation times.

The electrical current density (in real space) \vec{j} is simply:

$$\vec{j}(t) = -e \sum_{b,s} \int \left(\frac{d\vec{p}}{h} \right)^3 g^{(b,s)}(\vec{E}, \vec{p}, t) \vec{v}_g^{(b,s)}(\vec{p}). \quad (2.21)$$

Since j is 0 in equilibrium, only the perturbation g_1 will contribute to the current. We can solve Boltzmann's equation eq. (2.9) for g_1 . We start with

$$\frac{\partial g_1^{(b,s)}(\vec{p}, t)}{\partial t} - e \frac{\partial g_0^{(b,s)}(\vec{p})}{\partial \vec{p}} \vec{E}(t) = -\frac{g_1^{(b,s)}(\vec{p}, t)}{\tau^{(b,s)}(\vec{p})} \quad (2.22)$$

The solution for this equation will be an exponential decay of g_1 . In Fourier domain the entire equation reads:

$$-i\omega \tilde{g}_1^{(b,s)}(\vec{p}, \omega) - e \frac{\partial g_0^{(b,s)}(\vec{p})}{\partial \mathcal{E}} \frac{\partial \mathcal{E}(\vec{p})}{\partial \vec{p}} \tilde{\vec{E}}(\omega) = -\frac{\tilde{g}_1^{(b,s)}(\vec{p}, \omega)}{\tau^{(b,s)}(\vec{p})} \quad (2.23)$$

Here I have used the chain rule to expand $\frac{\partial g_0}{\partial \vec{p}}$. $\frac{\partial g_0^{(b,s)}(\mathcal{E}(\vec{p}))}{\partial \mathcal{E}}$ is the derivative of the Fermi-Dirac distribution. $\frac{\partial \mathcal{E}(\vec{p})}{\partial \vec{p}}$ is the group velocity \vec{v}_g . Eq. (2.23) merely has to be rearranged for $\tilde{g}_1(\vec{p}, \omega)$.

$$\tilde{g}_1^{(b,s)}(\vec{p}, \omega) = e \frac{\partial g_0}{\partial \mathcal{E}} \vec{v}_g^{(b,s)} \tilde{\vec{E}}(\omega) \frac{\tau^{(b,s)}(\vec{p})}{1 - i\omega\tau^{(b,s)}(\vec{p})} \quad (2.24)$$

The spectral current density $\tilde{\vec{j}}$ follows from eq. (2.21):

$$\tilde{\vec{j}}(\omega) = -e^2 \sum_{b,s} \int \left(\frac{d\vec{p}}{h} \right)^3 \vec{v}_g^{(b,s)}(\vec{p}) \left(\vec{v}_g^{(b,s)} \tilde{\vec{E}}(\omega) \right) \frac{\partial g_0}{\partial \mathcal{E}} \frac{\tau^{(b,s)}(\vec{p})}{1 - i\omega\tau^{(b,s)}(\vec{p})}. \quad (2.25)$$

In a general case, the current $\tilde{\vec{j}}$ does not have to be parallel to the electric field $\tilde{\vec{E}}$, and the magnitude of the current may also depend on the direction of $\tilde{\vec{E}}$. In the case of a

2 Theory of electrical conduction in metals

cubic crystal, the symmetry forces an isotropic conductivity and eq. (2.25) simplifies to [23, 27, 30]

$$\tilde{j}(\omega) = -\frac{e^2 \tilde{E}(\omega)}{3} \sum_{b,s} \int \left(\frac{d\vec{p}}{h}\right)^3 v_g^{(b,s)}(\vec{p}) v_g^{(b,s)}(\vec{p}) \frac{\partial g_0}{\partial \mathcal{E}} \frac{\tau^{(b,s)}(\vec{p})}{1 - i\omega\tau^{(b,s)}(\vec{p})}. \quad (2.26)$$

We have arrived at a scalar conductivity ($\tilde{j} = \tilde{\sigma} \tilde{E}$). One can rewrite the above integration over phase space in terms of an integration over energy \mathcal{E} .

$$\tilde{\sigma}(\omega) = -\frac{e^2}{3h^3} \int_0^\infty d\mathcal{E} \frac{\partial g_0}{\partial \mathcal{E}} \sum_{b,s} \iint_{S^{(b,s)}(\mathcal{E})} dS \cdot v_g^{(b,s)}(\vec{S}, \mathcal{E}) \frac{\tau^{(b,s)}(\vec{S}, \mathcal{E})}{1 - i\omega\tau^{(b,s)}(\vec{S}, \mathcal{E})}. \quad (2.27)$$

Here $S(\mathcal{E})$ is the iso-energy surface of $g(\vec{p}(\mathcal{E}))$ in momentum space. \vec{S} is a point on the surface, and dS the surface area around that point. As $\frac{\partial g_0}{\partial \mathcal{E}}$ is only non-zero in a $k_B T$ wide region about the chemical potential μ , the integral will only need to be evaluated around the chemical potential. This reduces the volume of phase space for which $\tau^{(b,s)}(\vec{p})$ and $v_g^{(b,s)}(\vec{p})$. Nevertheless, maps of τ and v_g across the surfaces $S(\mathcal{E})$ are still necessary to compute the conductivity.

2.4.5.1 Frequency limit of the semiclassical theory

The treatment of the electric field is purely classical, hence the discrete energy a photon transfers to the (quasi-) electron it interacts with is not accounted for. As long as the thermal broadening $k_B T$ of the electron distribution is larger than the photon energy hf , the quantised energy transfer is indeed negligible. Therefore the thermal broadening of the Fermi distribution gives a frequency limit of $k_B T/h \approx 6$ THz for this semiclassical approach. At higher photon energies, the photo-excited electrons will have a wider range of energies than the thermally excited electrons contributing to DC-transport and the distribution of the photo-electrons will no longer resemble the Fermi-Dirac distribution until they thermalise. Thermalisation times can be assumed to be longer than the momentum relaxation times; in the case of gold electrons close to the Fermi surface take more than 1 ps to thermalise [31], while they relax momentum within ca. 20 fs [32]. Therefore any energy dependence of the group velocity or the relaxation time or the size of the iso-energy surface makes conduction at higher frequencies no longer strictly comparable to steady-state conduction.

2.4.6 Maps of relaxation times and group velocities

Equation (2.27) permits calculating the conductivity dynamics, provided the iso-energy surfaces around the Fermi energy are known and detailed maps of the velocity and the relaxation times across these surfaces exist. Unfortunately, few maps exist, especially for the relaxation times. There are currently no maps for iron at room temperature, therefore no quantitative prediction of the dynamics of conduction will be possible.

2.5 Macroscopic conductivity of a relaxation time distribution

Connecting the observed dynamics with some gross properties of the unknown maps will hence give some insight into the maps.

2.5 Macroscopic conductivity of a relaxation time distribution

I want to retrieve information on the microscopic relaxation times from the macroscopic dynamics of the electrical conduction. It will be impossible to recover the entire maps $\tau_{b,s}(\vec{p})$, since two different maps may lead to the same macroscopic conductivity. I will define a function containing all the gross properties of the relaxation time maps relevant to the conduction dynamics. This function is the relaxation time distribution. The idea is very similar to the density of states per energy. Basically, we sort all states by their relaxation time. We then weight the states by their contribution to the conductivity for a unit relaxation time. The density of the weighted states on the relaxation time axis gives the relaxation time distribution $\mathfrak{w}(\tau)$. This relaxation time distribution governs the time evolution. More mathematically, we transform the integral over iso-energy surfaces S and energy \mathcal{E} eq. (2.27) into an integral over relaxation times.

$$\tilde{\sigma}(\omega) = -\frac{e^2}{3h^3} \int_0^\infty d\mathcal{E} \frac{\partial g_0}{\partial \mathcal{E}} \sum_{b,s} \iint_{S^{(b,s)}(\mathcal{E})} dS \cdot v_g^{(b,s)}(\vec{S}, \mathcal{E}) \frac{\tau^{(b,s)}(\vec{S}, \mathcal{E})}{1 - i\omega\tau^{(b,s)}(\vec{S}, \mathcal{E})} \quad (2.28)$$

$$= -\frac{e^2}{3h^3} \int_0^\infty d\tau \frac{\tau}{1 - i\omega\tau} \sum_{b,s} \iint_{\zeta^{b,s}(\tau)} d\zeta J_{\tau,\zeta}^{\mathcal{E},\vec{S}} \frac{\partial g_0}{\partial \mathcal{E}}(\vec{\zeta}, \tau) v_g^{(b,s)}(\vec{\zeta}, \tau) \quad (2.29)$$

$$= \int_0^\infty d\tau \frac{\tau}{1 - i\omega\tau} \mathfrak{w}(\tau) \quad (2.30)$$

Here $\zeta(\tau)$ are iso-relaxation time surfaces in phase space, $\vec{\zeta}$ the points on those surfaces and J is the appropriate Jacobian determinant. These quantities were only helpers on the way to the relaxation time distribution $\mathfrak{w}(\tau)$. Normalising it via

$$W^{-1} = \int_0^\infty d\tau \mathfrak{w}(\tau), \quad w(\tau) = W\mathfrak{w}(\tau) \quad (2.31)$$

creates a distribution $w(\tau)$ which can be understood as a probability distribution density; $w(\tau)d\tau$ gives the probability that a state of unit weight in the conduction process has a relaxation time between τ and $\tau + d\tau$. The total weight of conduction W^{-1} only depends on the band structure and hence is a material constant, similar to Drude's $\frac{ne^2}{m}$. We can approximate the complex conductivity $\tilde{\sigma}(\omega)$ for low frequencies by expanding eq. (2.30) around $\omega = 0$.

$$\tilde{\sigma}(\omega) = W^{-1} \sum_{l=1}^{\infty} (i\omega)^{(l-1)} \int_0^\infty w(\tau) \tau^l d\tau = W^{-1} \sum_{l=1}^{\infty} (i\omega)^{(l-1)} \langle \tau^l \rangle \quad (2.32)$$

2 Theory of electrical conduction in metals

The $\langle \rangle$ denote the average over the relaxation time distribution $w(\tau)$. Therefore the line shape of the complex conductivity is expressed in terms of the moments of the relaxation time distribution $w(\tau)$. As any probability distribution is fully characterised by its moments, in theory an exact measurement of the complex conductivity allows extracting the entire distribution of relaxation times. The Taylor series eq. (2.32) converges for angular frequencies ω lower than $\frac{1}{\tau}$. In practice, that means the higher moments of the distribution will be hard to recover experimentally.

The first two moments can be disentangled at low frequencies in properly phase-resolved data, because the second moment $\langle \tau^2 \rangle$ only affects the imaginary conductivity and therefore the phase. At low frequencies, the lag τ_l I am primarily searching for, reads simply:

$$\tau_l \underset{\omega \rightarrow 0}{=} \frac{\langle \tau^2 \rangle}{\langle \tau \rangle}. \quad (2.33)$$

2.5.1 Introducing the current response time

The lag τ_l is empirically easy to define (see fig. 1.2), but it steadily decreases with increasing frequency, ultimately converging towards 0 (see fig. 2.8). I will now introduce the current response time τ_C , which will be constant over a larger frequency range and converge at high frequencies towards a finite value that can be smaller, but similar in magnitude to the low frequency limit. The current response time is defined in such a way that it would be constant and equal to Drude's universal relaxation time, if such a universal relaxation time existed. This definition facilitates explaining the measurement of spectra of the shape predicted by Drude's universal relaxation time approximation, even though the relaxation times are not universal. Indeed, the spectral shape of the conductivity can be approximated up to second order in $\omega\tau$ as an effective Drude model:

$$\tilde{\sigma} \underset{\omega \rightarrow 0}{=} W^{-1} \frac{\langle \tau \rangle}{1 - i\omega \frac{\langle \tau^2 \rangle}{\langle \tau \rangle}}, \quad (2.34)$$

it has the same functional form as Drude's original equation (2.3).

We can define the observable current response time τ_C so that it will coincide with the time constant describing this effective Drude curve:

$$\tau_C(\omega) = \frac{\tan(\phi(\tilde{\sigma}))}{\omega} = \frac{\Im(\tilde{\sigma}(\omega))}{\omega \Re(\tilde{\sigma}(\omega))}. \quad (2.35)$$

In the low frequency range where eq. (2.34) applies, τ_C will be frequency independent and eq. (2.34) may be expressed as:

$$\tilde{\sigma} \underset{\omega \rightarrow 0}{=} \frac{\sigma_{DC}}{1 - i\omega\tau_C}, \quad (2.36)$$

with the steady state limit of the conductivity σ_{DC} . This means at low frequencies, the spectral shape of a distribution of relaxation times is the same as the one predicted by

2.5 Macroscopic conductivity of a relaxation time distribution

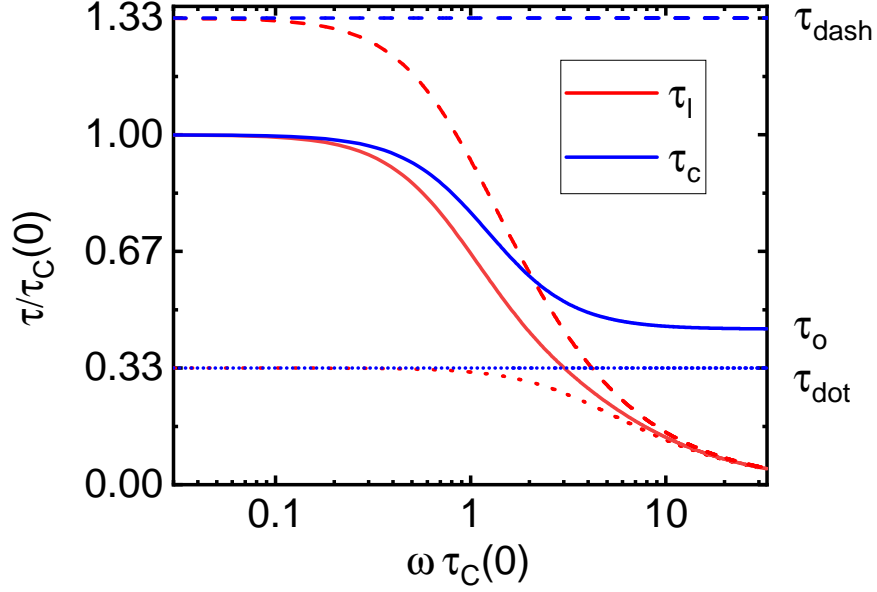


Figure 2.8: A comparison between the lags τ shown in fig. 2.2 and the corresponding response times τ_C , shown as a function of frequency. The times and frequency are expressed relative to the response time of the combined system at 0 frequency $\tau_C(0)$. The lines denote three different systems. The dotted line represents an ensemble of electron which all have the same momentum relaxation time τ_{dot} . The “dash” electrons also have a universal relaxation time τ_{dash} , which is four times larger than τ_{dot} . The solid line denotes a system comprised of 2/3 “dot” and 1/3 “dash” electrons; in distribution terms $w(\tau) = 2/3 \cdot \delta(\tau - \tau_{dot}) + 1/3 \cdot \delta(\tau - 4\tau_{dot})$. This system has a variation of $C \approx 0.7$. Red lines denote the observable lag of each system, blue lines denote the observed current response times. At low frequencies, lags and current response times are identical. The current response time stays constant over a wider frequency range; for the two homogeneous systems for all frequencies. For the mixed system, the response time decreases around $\omega\tau_C(0) = 1$ and then converges to the optical response time τ_O defined in eq. (2.42).

Drude (see eq. (2.3)). This effective Drude shape at low frequencies was also derived in a bit less detail by Kamal *et al.* [33] considering various relaxation rates in a metal oxide.

I will use the response time τ_C to replace the lag τ to describe the time evolution of conduction. In the low frequency regime both quantities are almost identical and their qualitative meaning is very similar, but on the background of the relaxation

time distribution picture, the response time τ_C has some advantages. While the lag has a more straight forward empirical meaning (see fig. 1.2), the response time τ_C is more closely connected to the microscopic relaxation times. Figure 2.8 shows that the response time will be constant over a larger range of frequencies. This allows a simpler description of the conduction dynamics.

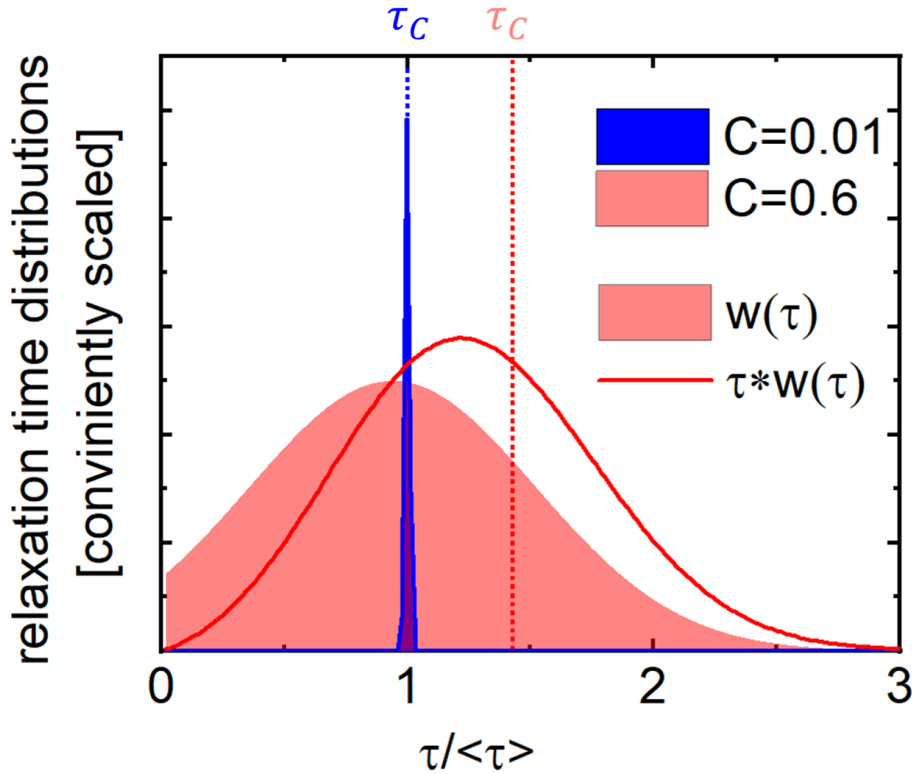


Figure 2.9: Two example distributions $w(\tau)$ of the relaxation times. The red area indicates a distribution of medium variation ($C=0.6$), the blue area a distribution close to no variation ($C=0.01$), which approximates a universal relaxation time. The solid lines indicate the relative contribution to the total current as a function of the relaxation time. For a universal relaxation time, the current distribution is identical to the relaxation time distribution. For the wider distribution, the electrons with larger relaxation time contribute more to the total current. The current distribution shifts to larger relaxation times. The mean of the current distribution is indicated by a dotted vertical line. This is the current relaxation time τ_C .

The expressions eqs. (2.32) to (2.34) and (2.36) connect the macroscopic measurement of the conductivity and the lag with the mesoscopic distribution of relaxation times. The most important moments are the first moment $\langle\tau\rangle$ also known as mean relaxation

2.5 Macroscopic conductivity of a relaxation time distribution

time and the second centralised moment $\langle (\tau - \langle \tau \rangle)^2 \rangle = \langle \tau^2 \rangle - \langle \tau \rangle^2 = \mathfrak{V}$ also known as variance. The mean $\langle \tau \rangle$ gives the general magnitude of the relaxation times and is the relevant quantity for direct current (DC) conduction. The standard deviation $s = \sqrt{\mathfrak{V}}$ is a measure how much the relaxation times $\tau(\vec{S}, \mathcal{E})$ vary across the map. The standard deviation s is the second key descriptor, as it allows identifying whether the entire map has to be taken into account or the mean value suffices. Relevant for this consideration is the standard deviation s relative to the mean $\langle \tau \rangle$. This quantity is called coefficient of variation C .

$$C = \frac{s}{\langle \tau \rangle} = \sqrt{\frac{\langle \tau^2 \rangle - \langle \tau \rangle^2}{\langle \tau \rangle^2}}. \quad (2.37)$$

$$\Rightarrow \tau_C = \frac{\langle \tau^2 \rangle}{\langle \tau \rangle} = \langle \tau \rangle (1 + C^2) \quad (2.38)$$

When the diversity of relaxation times is negligible, C goes to 0, and only the mean $\langle \tau \rangle$ is important. When $C = 0.5$, the distribution is about as wide as the mean value is large, implying a maximum relaxation time that is at least three times bigger than the minimum relaxation time.

From observed DC-conductivity σ_{DC} and current relaxation time τ_C , and a calculated electronic structure, the variation C can be derived from the ratio of the two observables.

$$\frac{\tau_C}{\sigma_{\text{DC}}} = W \frac{\langle \tau^2 \rangle}{\langle \tau \rangle^2} = \frac{1}{W} (1 + C^2) = R \quad (2.39)$$

Even if W is unknown, we can still track the change of the ratio R in a certain material when introducing a new scattering process. This will tell us how the scattering process changes the variation C of the relaxation times, even if we do not know the absolute value of C .

2.5.2 High-frequency limit of the semiclassical picture

We note that for high frequencies the photon energy will be too large to justify the semiclassical picture. Nevertheless, we can learn two important facts by looking at the high-frequency limit of the relaxation time distribution formalism. Similarly to the low-frequency expansion around $\omega\tau = 0$ in eq. (2.32), we can also expand eq. (2.30) around the limit $\frac{1}{\omega\tau} = 0$.

The result is

$$\tilde{\sigma}(\omega) \underset{\omega \rightarrow \infty}{=} W^{-1} \sum_{l=1}^{\infty} \frac{1}{(-i\omega)^l} \int_0^{\infty} w(\tau) \frac{1}{\tau^{l-1}} d\tau = W \sum_{l=1}^{\infty} (-i\omega)^{-l} \langle \tau^{1-l} \rangle \quad (2.40)$$

The first two terms of the expansion are

2 Theory of electrical conduction in metals

$$\tilde{\sigma}(\omega) \underset{\omega \rightarrow \infty}{=} W^{-1} \left[i \frac{1}{\omega} + \frac{1}{\omega^2} \left\langle \frac{1}{\tau} \right\rangle + O \left(\left(\frac{1}{\omega} \right)^3 \right) \right]. \quad (2.41)$$

Up to second order in $\frac{1}{\omega\tau}$, eq. (2.41) is identical to

$$\tilde{\sigma}_{op}(\omega) = \frac{\sigma_{HF}}{1 - i\omega\tau_o}; \quad (2.42)$$

With the high frequency conductivity $\sigma_{HF} = W_o^{-1} \left\langle \frac{1}{\tau} \right\rangle^{-1}$ and an optical current relaxation time $\tau_o = \left\langle \frac{1}{\tau} \right\rangle^{-1}$. This tells us the following:

1. It is not surprising to observe ‘Drude shape’ optical complex conductivities in the high-frequency limit, since the limiting expansion might hardly change for a non-thermal distribution.
2. Even though the same approximate model is observable, the parameters are fundamentally different. They are probably going to be on the same order of magnitude, but not directly comparable.

Only if band velocity was energy independent, W_o and W would be equal; and only if all electrons had the same relaxation time, optical and low-frequency conductivity would have the same response time. I refer to the assumption that all electrons experience identical momentum relaxation as ‘universal relaxation time assumption’.

2.5.3 Universal relaxation time assumption

The assumption of a universal relaxation time dates back to Paul Drude. For Drude’s gas of identical, classical particles, the assumption is very reasonable. For a gas of fermions, which must all differ in at least one quantum number from another, it is not. Mathematically, the assumption of all electronic states relaxing with the same time constant τ_u is expressed as:

$$\tau_{b,s}(\mathcal{E}, \vec{S}) = \tau_u \quad \forall \quad b, s, \mathcal{E}, \vec{S} \quad (2.43)$$

This relaxation time τ_u will also be universal for all different kinds of excitations [27]. Therefore also the point relaxation rates $\frac{1}{\tau_P(\vec{S})}$ in fig. 2.10 would have to be constant across the map. Again, the universal relaxation time assumption appears motivated by simplicity rather than reality. It is extremely common.

In the distribution picture we have just developed, the relaxation time distribution $w(\tau)$ reduces to $\delta(\tau - \tau_u)$ and the complex conductivity results in the shape of Drude’s original model:

$$\tilde{\sigma} = \frac{W^{-1}\tau_u}{1 - i\omega\tau_u} = \frac{\sigma_{DC}}{1 - i2\pi f\tau_u} \quad (2.44)$$

Comparing to eq. (2.36) we notice that in the low frequency region $\omega \ll \frac{1}{\tau}$, the shape of the conductivity spectra will be identical for a universal relaxation time and a wide

2.6 Assumptions for the relaxation time distribution model

distribution of relaxation times. The parameters will be different: In the universal relaxation time scenario σ_{DC} is strictly proportional to $\tau_C = \tau_u$. For a relaxation time distribution of relative width C , σ_{DC} is proportional to $\tau_C/(1 + C^2)$.

2.6 Assumptions for the relaxation time distribution model

2.6.1 Linearity of the response

An important assumption done throughout this thesis is the linearity of all responses. I will motivate this assumption in the background of the phase space density and Boltzmann's equation eq. (2.9). The key property of a metal that the size of the iso-energy surfaces around the chemical potential is large; larger than in all other conducting systems (such as semiconductors, Dirac-materials or topological insulators) and of similar surface area as the primitive unit cell. Putting it in a different perspective, very many states contribute to conduction. Hence, unless specific resonances are triggered, the energy and momentum from an applied electric field will be distributed among very many states, that is, across a very large volume of phase space. It requires extreme amounts of energy to alter the entire volume so that the change in the phase space density g_1 becomes comparable to the equilibrium phase space density g_0 . By similar reasoning, since the number of internal states is so large, the number of particles that have to be added to affect significant changes in the chemical potential is huge. It is therefore impossible to change the chemical potential of a metal by doping.

2.6.2 Neglecting magnetic fields

I have neglected the magnetic field in the Boltzmann equation eq. (2.9), despite dealing with iron in this thesis. This is justified by two circumstances:

1. The magnetisation in iron is static on the time scale of the dynamics of electronic conduction in room temperature.
2. The cyclotron frequency from the magnetisation is small compared to the scattering rates $\frac{1}{\tau_{b,s}(\vec{p})}$.

Time-scale of magnetisation dynamics

The characteristic frequency for the rotation of magnetic domains from the Landau-Lifschitz-Gilbert equation is about 1 GHz. This is also the frequency scale for magnon-resonances in ferro-magnetic systems. Large fields with amplitudes of 6 T are required to change magnetisations on a picosecond or femtosecond time-scale [34].

Cyclotron frequency

The cyclotron frequency ω_C is the angular frequency with which a moving particle of charge q and mass m orbits in a constant magnetic field B .

$$\omega_C = \frac{qB}{m} \tag{2.45}$$

Magnetic fields force electrons to move on cyclotron orbits, both restricting the available phase space and forcing the electron to cycle through its orbit. If the electron is much more likely to be scattered into a different position, potentially on a different orbit than completing the original orbit, the effects of the magnetic field will be negligible. Also, any resonances associated with the cyclotron frequency will be so overdamped that they are irrelevant. The cyclotron frequency for a free electron in a field of 2 Tesla (approximately the saturation magnetisation of iron) is ca. 0.3 THz, while the expected scattering rates are roughly 30 THz, about 100 times higher. Therefore I will neglect any effects of the magnetisation of the iron samples.

2.7 Evidence for the distribution of relaxation times

2.7.1 Maps of point relaxation times

Radio frequency finite-size effects [22] such as the De Haas-van Alphen [35] effect and similar methods based on the cyclotron resonance [36,37] can map the Fermi velocity and point relaxation time along certain orbits on the Fermi surface.

Whereas data on the relaxation times for electrical conduction are hard to find, the so-called point relaxation times or point scattering rates [19,22] can be determined in radio frequency size effects, which are again based on the cyclotron resonance and similar effects. These effects allow selectively exciting electrons from resonant orbits or even points on the Fermi surface. The relaxation times for these excitations can be extracted [19,22,36].

In the “golden age of fermiology”³ [22], point relaxation times were mapped for noble metals [18,36] at liquid hydrogen temperatures where defect scattering dominates [38]. The point relaxation times are highly anisotropic, even for single-band noble metals such as gold shown in fig. 2.10.

Since the excitation g_1 by radio frequency size effects is markedly different from that (quasi) DC-electric fields, these point relaxation times may be different from the relaxation times governing the dynamics of electrical conduction, as explained in fig. 2.7. If and how much these two types of relaxation times are different is an open question. Time-resolving the conduction will give us insight into some gross properties of the map of relaxation times relevant for electrical conduction.

³Term used by Gasparov *et al.* [22] to describe a boom in measurements of the Fermi surface between ca. 1970 and 1975

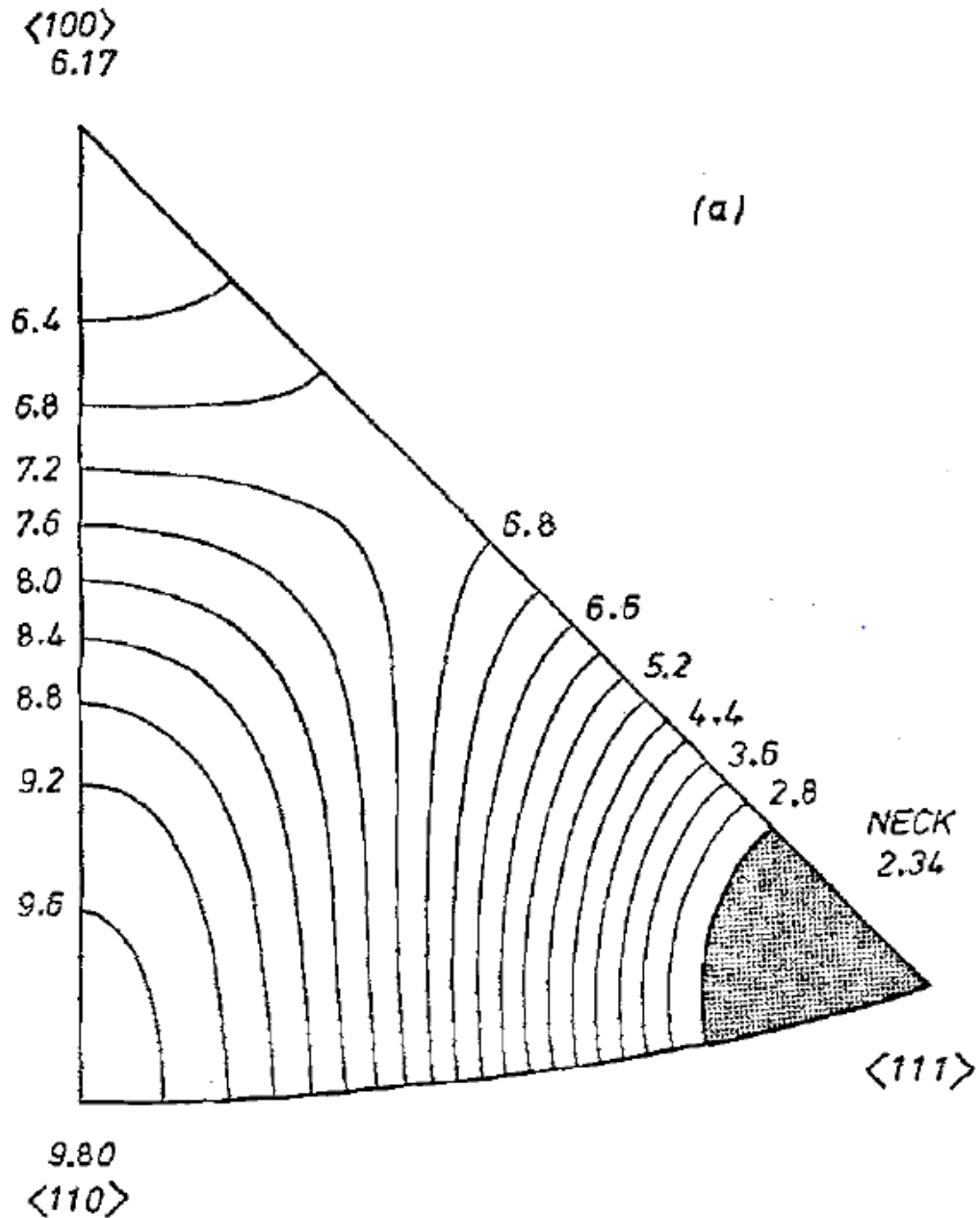


Figure 2.10: Map of the point relaxation rates in gold from impurity scattering on silver per % of silver content. The map has been calculated from de Haas-van Alphen effect measurements by Lowndes et. al. [38]. Figure taken from Springford's 1975 overview [19]. The map shows a stereographic projection of 1/48th of the Fermi surface, from which the rest of the surface can be deduced by symmetry operations. The unit of the relaxation rates is THz/%. Note the large anisotropy between the "neck" region and the corner in <110> direction.

2.7.2 Deviations from Mathiessen's rule

In 1864, before the discovery of atomic structure and electrons, Mathiessen and Vogt [39] measured the resistivity of alloys depending on temperature T and substituent metal concentration K . For most alloys, Mathiessen and Vogt could calculate the resistivity of a pure metal from the resistivity scaling of the alloy. Their formula can be rearranged as:

$$\rho_{tot} = \rho(T) + \rho(K) \quad (2.46)$$

Here ρ_{tot} is the total resistivity of the alloy. This formula is known as Mathiessen's rule. Since already Mathiessen and Vogt [39] found it only to work for most, not all, alloys they investigated, it is rather a rule of thumb. A more generalised version of this rule permits to add any dimensions of resistivity scaling in addition to temperature and concentration. The scaling dimensions often relate to the microscopic scattering mechanisms, for example the temperature scaling relates to phonon scattering. Sommerfeld [13] showed that if the mean free path is universal and the scattering cross sections of the different mechanisms do not correlate, Mathiessen's rule follows. In this case of a universal rate and uncorrelated scattering mechanisms, a rate $\frac{1}{\tau_u(j)}$ can be attributed to each scattering mechanism j , such that for the universal scattering time τ_u

$$\frac{1}{\tau_u} = \sum_j \frac{1}{\tau_u(j)} \quad (2.47)$$

follows. Since the relaxation time is assumed to be universal, the relaxation time is directly proportional to the total conductivity.

3 conditions must be met to result in Mathiessen's rule:

1. The electronic structure remains the same, only the scattering changes
2. The probabilities for scattering by different mechanisms do not correlate
3. The relaxation time is universal

When point 1 and 2 are presumably fulfilled, any deviation from Mathiessen's rule must stem from the variety of the relaxation times [19,21]. This phenomenon has been used in several ways to gain insight into the distribution of relaxation times. Springford et al. [19] compared the deviations from Mathiessen's rule to the variety of point relaxation times they had mapped. Fert and Campbell [20] used the deviations from Mathiessen's rule in iron and nickel alloys to derive their spin-split two-current model. This two-current model was the basis for Fert's subsequently discovering the giant magnetoresistance effect [40,41]. The first explanation for non-Mathiessen conductivity scaling came from Sir Neville Mott [5].

2.8 Previous models for diverse relaxation times

2.8.1 Mott model

Already Mathiessen and Vogt [39] notice that iron behaved oddly, and subsequent measurements of the temperature scaling of the resistivity of ferromagnets showed an inexplicably strong increase of resistivity when approaching the Curie temperature. Around 1890, the $\text{Co}_{55}\text{Ni}_{45}$ and $\text{Co}_{84}\text{Mn}_{12}\text{Ni}_4$ alloys trade named Constantan and Manganin were discovered. These two alloys have constant resistivity for a temperature range from 40 to 400 K. Mott [5] showed both phenomena may occur when electrons with different relaxation times contribute to conduction.

2.8.1.1 Energy dependent relaxation times

For the case of Constantan and Manganin, the density of states per unit energy is large at the Fermi surface. Therefore a large number of final states is available for electrons at the Fermi energy. As the probability that an electron scatters is proportional to the number of states it can scatter into, the relaxation time for electrons with energies close to the Fermi energy is low. But only slightly above the Fermi energy, the density of states becomes much smaller, as the d-bands are filled up. Here the relaxation time is much higher. When the alloys are heated, two processes compete: More electrons are excited into high energy states with higher relaxation time. More phonons are created, increasing the electron-phonon scattering rate. The exact alloy composition is the sweet spot where both processes cancel each other.

2.8.1.2 Spin dependent relaxation times

For ferromagnets, Mott examined the case of Nickel. Here only d spin \downarrow states are located at the Fermi edge; while d \uparrow are at lower energies. When spin-flip scattering is unlikely, this means that spin \uparrow electrons have much fewer final states to scatter into, hence a much longer relaxation time. These electrons conduct the majority of the current, not only in spite, but because of having a smaller density of states at the Fermi level. As the temperature approaches the Curie temperature, spin \uparrow and \downarrow states shift towards each other. This leads to a strong increase in final states for the \uparrow electrons, resulting in the observed strong increase in resistivity.

2.8.2 Two-current models

When faced with the realisation that relaxation times in metals are diverse, one can proceed in two ways. I have introduced the general way, describing the conductivity for an arbitrary distribution of relaxation times. The other approach is to reduce complexity as much as possible by choosing the next simplest distribution to a single relaxation time: two relaxation times. The idea is that all states will be grouped into two species, one with short and one with long relaxation time.

2.8.2.1 Neck-belly two band model

Springford *et al.* [19] tried to compare the variety of point relaxation times they observed to the deviations from Mathiessen's rule by dividing their maps of the Fermi surface (fig. 2.10) into two regions, "neck" and "belly". They then calculated a single time for each region and estimated the deviations from Mathiessen's rule expected from this. The agreement was rather qualitative than quantitative, reasons for this could either be the neck-belly simplification or the disparity between point relaxation times and the relaxation times of "normal" electrical transport.

2.8.2.2 Spin-split two-current model

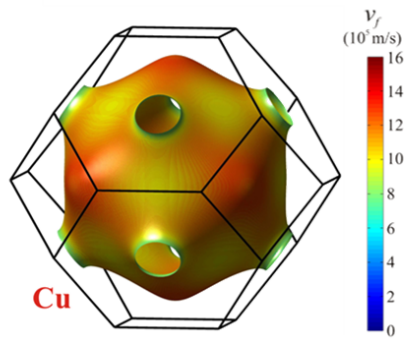
Fert and Campbell [20] interpreted the non-Mathiessen resistivity scaling of iron and nickel alloys by elaborating the idea of spin-split transport proposed by Mott. The understanding that relaxation times depend on spin led to Fert's discovery of the giant magnetoresistance [40] when manipulation of the magnetisation/spin became feasible in magnetic multilayers [41]. The giant magnetoresistance shows how understanding the differences in relaxation times paves the way for manipulating the relaxation to obtain useful physical effects.

2.9 Summarising

2.9.0.1 Calculating current dynamics from basic principles

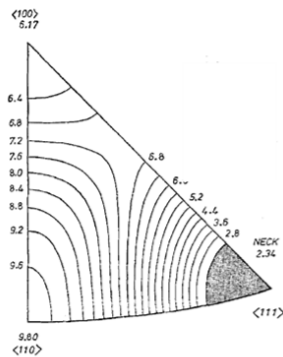
I summarise the necessary steps one would have to take to calculate conduction dynamics in a metal from first principles. Calculating the electronic band structure would merely be the first step. Using this dispersion relation, the relaxation times have to be calculated for each scattering mechanism in a second step. Thirdly, combining these relaxation times may require assessing correlations between different mechanisms. This has to be repeated for each point around the Fermi surface, resulting in a map of relaxation times in step 4. In a 5th step, the crucial information from the maps of Fermi velocities and relaxation times is condensed into a distribution of relaxation times. From this distribution of relaxation times one can calculate the conduction dynamics; the mean $\langle\tau\rangle$ and variation C of the distribution of relaxation times suffice for the low frequency limits of conductivity and current response time. Figure 2.11 illustrates this summary.

1. Band structure at the Fermi Surface

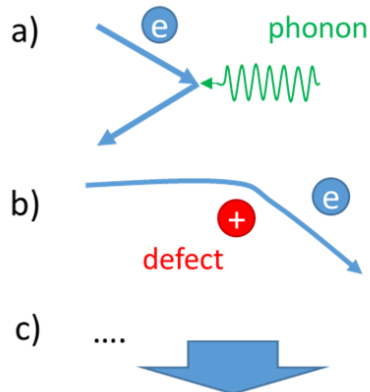


$$W^{-1} \propto \iint_S v_f dS$$

4. Map of relaxation times



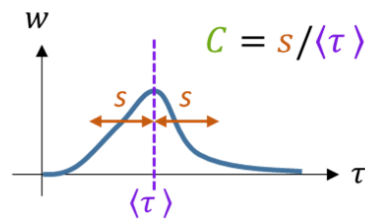
2. Scattering mechanisms



3. Combining scat. mech.

$$\frac{1}{\tau} = \frac{1}{\tau_a} + \frac{1}{\tau_b} + \overbrace{\frac{1}{\tau_{ab}}}^{\text{correlation}} + \dots$$

5. Distribution of relaxation times



6. Conduction dynamics

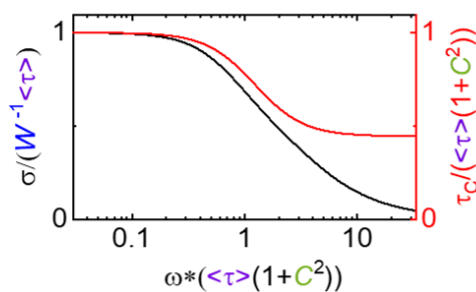


Figure 2.11: Necessary steps to calculate conduction dynamics. As an example map of the Fermi velocities, I took the map calculated by Gall [30] for copper. Springford [19] originally published the map of relaxation rates in gold shown in step 4.

2.9.0.2 Time constants describing conduction dynamics

The key point to understand the dynamics of conduction in metals is that very many electronic states contribute to conduction and these states differ in their relaxation times τ . Given that a multitude of relaxation times τ exists, more than one time constant appears in the description of time-dependent conduction. The related macroscopic observables lag τ_l and response time τ_C can be connected to mean $\langle \tau \rangle$ and the variation C of the microscopic relaxation times τ . In the following, I will discuss the experimentally observed dynamics in terms of the current response time τ_C ; the observed DC conductivity σ_{DC} will be proportional to the average of the microscopic relaxation times $\langle \tau \rangle$. Comparing τ_C to σ_{DC} yields information about the coefficient of variation C of the distribution of microscopic relaxation times. The table below gives an overview of the time constants used in this thesis:

name	symbol	math. def	type	explanation
lag	$\tau_l(\omega)$	$\phi(\tilde{\sigma})(\omega)/\omega$	macro. observable	lag between applied field and resulting current
current response time	$\tau_C(\omega)$	$\tan(\phi(\tilde{\sigma}))/\omega = (\Im(\tilde{\sigma})/\Re(\tilde{\sigma}))/\omega = \langle \tau \rangle (1+C^2)$ $\omega \rightarrow 0$	macro. observable	time constant for an exponentially decaying current
point relaxation time	$\tau_p(\vec{p}, u)$	–	meso. obs.	dissipation constant of a resonance u of point/limited area \vec{p} of the Fermi surface
relaxation time	$\tau(\vec{p})$	$-\frac{g_1(\vec{p})}{I_C(g_1, \vec{p})}$	theo. approximation (possible micro. obs.)	approximation of the collision integral at position \vec{p} for constant electric field
mean relaxation time	$\langle \tau \rangle$	$\int_0^\infty w(\tau)\tau d\tau = \sigma_{DC}W = \frac{\tau_C(\omega)}{1+C^2}$ $\omega \rightarrow 0$	macroscopic average, not observable	average over the relaxation time distribution, relevant for DC-conductivity
universal relaxation time	τ_u	$\tau_u = \tau(\vec{p}) \forall \vec{p} \Rightarrow \tau_u = \langle \tau \rangle = \tau_p = \tau_C$	oversimplifying assumption	Drude's original assumption that all relaxation times are equal.

Table 2.1: List of the different relaxation time constants relevant for the description of the current dynamics.

3 Thickness scaling of conduction dynamics

I aim to time resolve conduction in 2.2 to 100 nm thick iron films. For such thin films, the thickness is similar to the distance an electron is expected to travel before scattering. This distance is usually referred to as mean free path, though I will use mostly use the term expected free path. Since the films are so thin, a large fraction of the electrons may hit one of the surfaces between any two scattering events in bulk. Since the surfaces are imperfect, electron wave packets reaching the surface may not be reflected like light hitting a mirror, but rather scattered randomly, like diffuse reflection. These scattering events also randomise in-plane momentum, reducing the relaxation time also in the in-plane direction. This leads to a reduced in-plane conductivity for thin, mono crystalline films. Thomson [42] first proposed this effect. His basic picture is a good basis, but his mathematical model oversimplified too much to be useful. Fuchs [43] improved upon Thomson's model using the Bloch-Boltzmann formalism introduced in chapter 2. The problem is that Fuchs's model is still both mathematically complicated and has a large number of free parameters. Further, the model cannot be easily appended to predict dynamics. Last but not least, Fuchs presumes all electrons to have the same, universal mean free path. This contradicts both our knowledge of the anisotropic Fermi velocity and the distribution of relaxation times. On the other hand, experimental data for the same system as investigated here (iron epitaxially grown on MgO) also varies strongly between different studies. Different results on the same system indicate that sufficient experimental control over the system may not yet have been achieved. Therefore, I focus on a qualitative rather than quantitative description of the effects of surface scattering here. The focus is on how surface scattering may influence the distribution of relaxation times, not only in terms of lowering the average $\langle \tau \rangle$, but also the variation C . To start of, we have to understand the concept of a mean free path.

3.1 Mean free path

By mean free path of an electron we refer to the expected distance the electron travels before its velocity is randomised. The name mean free path leads to a bit of confusion when looking at an ensemble of different particles whose expectation values for this distance are different from one another. The confusion arises when looking at the ensemble average of the expectation values, which could then be called 'mean of mean free paths'. Obviously mean free path and 'mean of mean free paths' are different

3 Thickness scaling of conduction dynamics

quantities. I will use expected free path in the following for the expectation value of a single particle (conventionally 'mean free path') and average of expected free paths for 'mean of mean free paths' when necessary to avoid confusion. The expected free path \bar{l} of a certain state $(b, s, \mathcal{E}, \vec{S})$ in direction \hat{e}_j is the product of the group velocity \vec{v}_g and the relaxation time of that state. When the relaxation time τ depends on the direction \vec{S} in momentum space, τ also depends on direction \hat{e}_j .

$$\bar{l}^{(b,s)}(\mathcal{E}, \vec{S}) = \sum_j \tau_j^{(b,s)}(\mathcal{E}, \vec{S}) \left(\vec{v}_g^{(b,s)}(\mathcal{E}, \vec{S}) \hat{e}_j \right) \hat{e}_j \quad (3.1)$$

3.1.1 Universal mean free path assumption

Again, often the assumption is made that the mean free path is universal and isotropic.

$$\bar{l}_j^{(b,s)}(\mathcal{E}, \vec{S}) = l_u \quad \forall \quad b, s, \mathcal{E}, \vec{S} \text{ and } j \quad (3.2)$$

This assumption implies that the magnitude of the group velocity is the same for all states at the Fermi-surface. This contradicts our knowledge of the Fermi-surface, but it is simple. This 'universal mean free path' assumption is used for all common thickness scaling models [6, 42–44].

3.2 Thomson model

Four years after discovering the electron, J.J. Thomson [42] described electrons inside a metal scattering of the surface and predicted a thickness scaling from it. Like Drude, he treats the electrons like as identical classical particles. Thomson assumes the electrons have an expected free path l_∞ in bulk and to scatter when they hit the surface. In a thin film, the expected free path then depends on the distance of the electron from the surface and the velocity towards the surface. Fuchs [43] gives a good illustration of Thomson's model. My adaptation of Fuchs's sketch is displayed in fig. 3.1. I will use the notation of z for the direction perpendicular to the film plane, and the film extending from $z = 0$ to $z = a$. Thomson made extreme assumptions to keep computation simple, such as assuming that each electron would scatter exactly at the point where it had travelled a distance equal to the bulk mean free path. This unfortunately caused conceptual problems and large inaccuracies.

3.3 Fuchs model

Fuchs [43] assumed a similar picture of electrons scattering at the surface. Contrary to Thomson, he started with Boltzmann's equation. Rather than introducing a position dependent collision integral, Fuchs introduced boundary conditions at the interfaces to model the scattering. Fuchs's conditions are static, therefore his model cannot predict dynamics. Fuchs's model is still the go-to model to which any newer model is compared to.

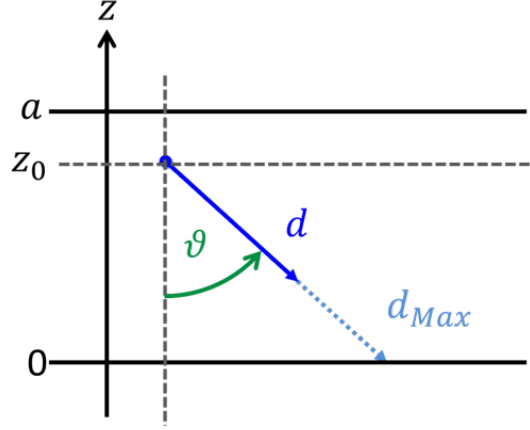


Figure 3.1: Sketch of Thomson's basic idea. The thin metal film goes from $z = 0$ to $z = a$. The free path of the electron is either given by the mean free path in bulk or the distance to the surface d_{Max} , which depends on initial position z_0 of the electron and the angle ϑ at which it travels towards the surface.

Fuchs derives a static version of Boltzmann's equation where the phase space density g depends on the z position:

$$v_z \frac{\partial g_1(\vec{v}, z)}{\partial z} + \frac{1}{\tau_u} g_1(\vec{v}, z) = \frac{-eE}{m} \frac{\partial g_0(\vec{v}, z)}{\partial v_x} \quad (3.3)$$

I have used the E for the electric field, τ_u for the universal relaxation time, $-e$ and m for the electron charge and mass and g_0 and g_1 for the equilibrium phase space density and its perturbation by the applied field, the same notation as in eq. (2.22). Note that Fuchs's phase space comprises velocity v instead of momentum p . The general solution to eq. (3.3) is

$$g_1(\vec{v}, z) = \frac{-eE\tau_u}{m} \frac{\partial g_0(\vec{v}, z)}{\partial v_x} \left[1 + \Phi(\vec{v}) e^{-\frac{z}{\tau_u v_z}} \right]. \quad (3.4)$$

Fuchs assumes the equilibrium density g_0 to be constant in space, independent from z . This is not obvious and rather contradictory to the idea that the scattering is not homogeneous but concentrated at the surfaces. The function $\Phi(\vec{v})$ must be determined by boundary conditions. Further one must differentiate between upward moving ($v_z > 0$) and downward moving electrons ($v_z < 0$), effectively dividing the phase space into two halves. The density in the upward moving half of phase space is denoted with a plus, as g_1^+ . The density of the $v_z < 0$ half is g_1^- .

The assumption then is that electrons hitting a surface are either perfectly specularly reflected or completely diffusively scattered. The fraction ε of all electrons is reflected. This leads to the following boundary condition for the density of electrons leaving the bottom surface at $z = 0$ [6]:

$$g_0 + g_1^+(v_z, z = 0) = \varepsilon [g_0 + g_1^-(-v_z, z = 0)] + (1 - \varepsilon)g_0 \quad (3.5)$$

3 Thickness scaling of conduction dynamics

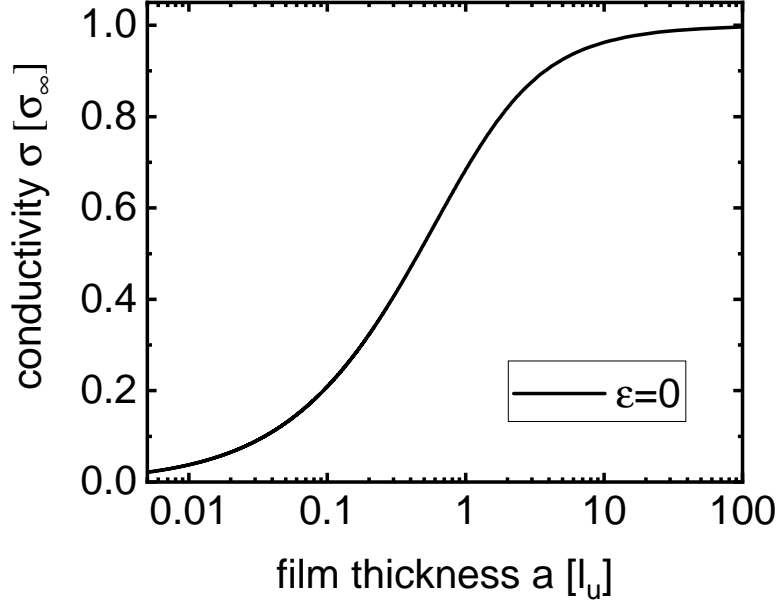


Figure 3.2: Plot of the conductivity scaling according to the Fuchs model for 0 specular reflection ($\varepsilon = 0$). The conductivity is expressed relative to the bulk conductivity σ_∞ ; the film thickness relative to the universal mean free path l_u .

and similarly at the top surface $z=a$:

$$g_0 + g_1^-(v_z, z = a) = \varepsilon [g_0 + g_1^+(-v_z, z = a)] + (1 - \varepsilon)g_0. \quad (3.6)$$

eqs. (3.5) and (3.6) applied to eq. (3.4) yields a z -dependent distribution g_1 of the velocity phase space.

$$g_1^+(\vec{v}, z) = \frac{-eE\tau_u}{m} \frac{\partial g_0}{\partial v_x} \left[1 + \frac{1 - \varepsilon}{1 - \varepsilon e^{-\frac{a}{\tau_u v_z}}} e^{-\frac{z}{\tau_u v_z}} \right], \quad (3.7)$$

$$g_1^-(\vec{v}, z) = \frac{-eE\tau_u}{m} \frac{\partial g_0}{\partial v_x} \left[1 + \frac{1 - \varepsilon}{1 - \varepsilon e^{\frac{a}{\tau_u v_z}}} e^{-\frac{z-a}{\tau_u v_z}} \right]. \quad (3.8)$$

The current is then the integral of the perturbation g_1 over the velocity phase space and the z -direction (see eq. (2.21)). This rather complicated integral yields a direct current conductivity σ_{DC} relative to the bulk value σ_∞ of [6]:

$$\frac{\sigma_{DC}(a)}{\sigma_\infty} = 1 - \frac{3}{2} \frac{l_u}{a} (1 - \varepsilon) \int_1^\infty (x^{-3} - x^{-5}) \frac{1 - e^{-\frac{a}{l_u x}}}{1 - \varepsilon e^{-\frac{a}{l_u x}}} dx. \quad (3.9)$$

Here $l_u = v_F \tau_u$ is a universal mean free path implying an isotropic Fermi velocity v_F and universal relaxation time τ_u . This is obviously quite far away from reality. The

specularity parameter ε might depend quite arbitrarily on film thickness, which may give the model more than one free parameter per observable data point. Fig 3.2 shows the scaling relation for total catastrophic scattering ($\varepsilon = 0$).

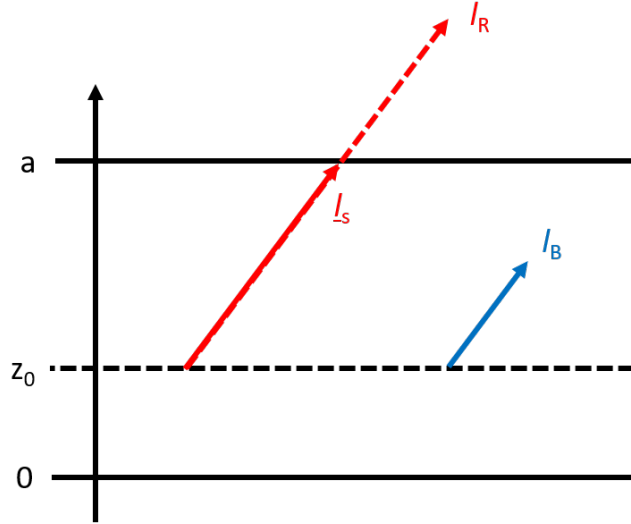


Figure 3.3: Sketch illustrating the anticorrelation between bulk and surface scattering. An electron which hardly scatters in bulk (red) will have a long expected free path l_R (red dashed line). The long bulk free path electron is hence very likely to reach the surface and scatter off it. Surface scattering hence limits the free path of the electron to l_S . A different electron with a short expected free path l_B (blue) is unlikely to reach the surface. Its free path stays unaffected. Hence the less likely electrons scatter in bulk, the more likely they are to scatter off a surface. Bulk and surface scattering are anticorrelated.

A couple of things can be learned from Fuchs's model which will generally hold true for most, if not all, thickness scaling models assuming a universal mean free path:

1. The universal mean free path l_u gives the length scale for the thickness scaling. The scaling only depends on the fraction a/l_u .
2. The relative propensity of surface scattering depends on the mean free path in bulk. This means bulk and surface scattering correlate.

In reality, metals cannot be described by a universal mean free path l_u , even less so than by a universal relaxation time τ_u . This means the universal mean free path has to be replaced by a distribution w_l of expected free paths l . Further, surface and bulk scattering probabilities are statistically dependent: The lower the bulk scattering probability of a given electron, the more likely this electron reaches the surface, hence the higher the probability of scattering on the surface. This anticorrelation between

3 Thickness scaling of conduction dynamics

bulk and surface scattering has the potential of narrowing the distribution of expected free paths, and therefore the distribution of relaxation times.

3.4 Scaling of the relaxation time distribution

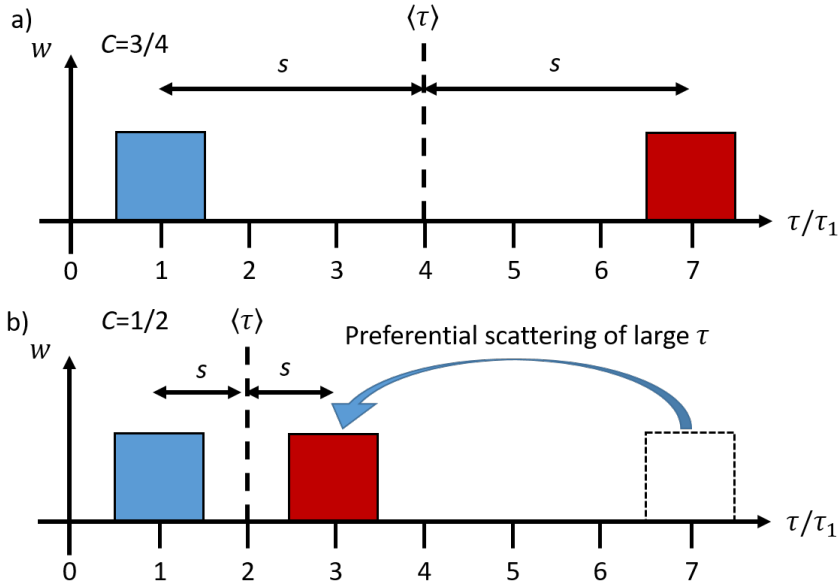


Figure 3.4: Sketch of narrowing of a distribution by a scattering mechanism preferentially scattering electrons with otherwise large relaxation times τ . Panel a) shows an example distribution without this scattering mechanism. The distribution is composed of extremely long relaxation time component (red) and an equally large short relaxation time component (blue). The variation $C = s / \langle \tau \rangle$ of this distribution is large. b) The scattering mechanism is assumed to be extremely preferential, only scattering long relaxation time (red) electrons. This drastically reduces the red relaxation time. Therefore the standard deviation s decreases drastically. The mean relaxation time $\langle \tau \rangle$ is also reduced, but to a lesser extend, which leads to a reduction in the coefficient of variation C .

The relevant quantity for the surface scattering probability of a microscopic state is its expected free path. This microscopic expected free path is directly proportional to the microscopic relaxation time of this state, the proportionality is given by the group velocity of that state eq. (3.1). When we now look at an ensemble different states, this direct proportionality is no longer valid for the quantities of the ensemble: Each microscopic state may have a different group velocity. For the sake of simplicity, I will still assume a one-to-one correlation between the distribution of expected free paths

3.4 Scaling of the relaxation time distribution

and the distribution of relaxation times. This will provide a qualitative understanding of the mechanisms by which a distribution may either be narrowed or widened by surface scattering.

3.4.1 Narrowing by anticorrelated scattering mechanisms

An electron travelling towards a surface in a metal film will only reach that surface if it does not scatter in the bulk before. Therefore bulk and surface scattering must be anticorrelated, see fig. 3.3. This means that surface scattering may narrow the distribution; mathematically narrower means smaller variation C ; illustrated in fig. 3.4.

3.4.2 Broadening by direction dependent relaxation times

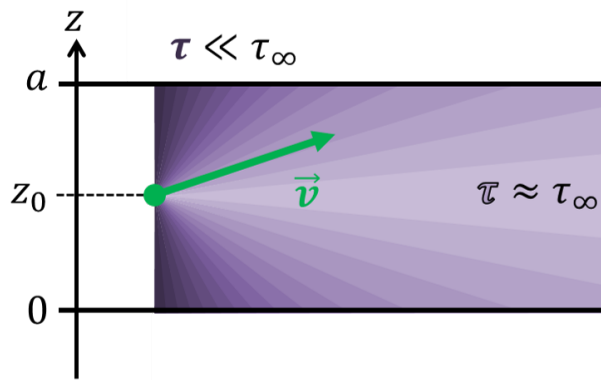


Figure 3.5: Sketch of the dependence of the relaxation time τ of an electron on the direction it travels. An electron travelling parallel to the surface cannot scatter on the surface and will therefore retain the bulk relaxation time τ_∞ . Electrons travelling directly towards the surface will encounter the strongest decrease in the expected free time. This process increases the variation of the distribution of relaxation times.

An electron moving parallel to the surface will not reach it, and therefore cannot scatter on the surface, only in the bulk. An electron moving directly towards the closest interface has a high chance of scattering on that interface. In general, the probability that a certain electron will scatter on a surface rather than in bulk depends on its distance and direction of travel relative to the surface, illustrated in fig. 3.5. This means even if there was only a single, universal microscopic relaxation time in bulk, surface scattering will induce variation in relaxation times by discriminating electrons based on position and velocity. This additional variation will lead to a broadening of the relaxation time distribution. In general, this effect will become stronger the stronger the relative propensity of surface scattering becomes. Therefore this broadening will out-compete any narrowing by anticorrelated scattering mechanisms when the films become so thin that surface scattering dominates.

3 Thickness scaling of conduction dynamics

I note that the relaxation time approximation becomes far less justified in the surface scattering case, since the potential time of impact of a given electron/state is not random, but rather entirely determined by speed towards and distance to the surface. As long as speed and distance are somewhat random within a given group of electrons of similar relaxation time, the scattering events for the whole group will also appear mostly random, giving some legitimacy to the approximation. Further quantum mechanical effects like the uncertainty principle induce at least some randomness in the surface scattering of an individual state.

3.5 Namba's roughness effect

3.5.1 Roughness effect on measured conductivity

When dealing with a rough film, the roughness will lower the thickness relevant for conduction compared to the measured thickness. To illustrate, consider the two dimensional (2D) scenario of a material of varying height a conducting in direction x . The direct current resistance Z over a distance D of the wire is given by:

$$Z = \frac{1}{L_B} \int_0^D \frac{1}{a(x)\sigma_{DC}(a(x))} dx \quad (3.10)$$

Here L_B is the constant width of the wire. Our macroscopic DC-conductivity estimate $\langle \sigma \rangle_a$ is an average over all thickness a , computed assuming a universal thickness equal to the average thickness $\langle a \rangle_a$:

$$\langle \sigma \rangle_a = \frac{D}{Z L_B \langle a \rangle} \left(\int_0^D \frac{1}{a(x)\sigma_{DC}(a(x))} dx \right)^{-1} = \frac{1}{\langle a \rangle_a} \left\langle \frac{1}{a\sigma_{DC}(a)} \right\rangle_a^{-1} \quad (3.11)$$

The harmonic average $\langle \frac{1}{a\sigma_{DC}(a)} \rangle^{-1} = D \left(\int_0^D \frac{1}{a(x)\sigma_{DC}(a(x))} dx \right)^{-1}$ over the sheet conductance $\sigma \cdot a$ is always smaller than the arithmetic mean $\langle a\sigma_{DC}(a) \rangle$, especially because the conductivity decreases with decreasing thickness. Even if we neglect the thickness dependence of the microscopic conductivity ($\sigma_{DC}(a)$), we still use the arithmetic mean for the estimate, while we would need the harmonic mean, see fig. 3.6. Since the harmonic mean is always smaller than the arithmetic mean, this means we are underestimating the actual conductivity. The rougher the film, the more this deviation between harmonic mean and arithmetic mean increases. When one wants to compute the size of the effect, one needs to know the actual distribution of thicknesses $\eta(a)$. Namba [45] assumed a sinusoidal variation of thicknesses which allowed him to calculate a correction factor for the 2D case. Namba's analytical model is used for real 3D films [46], as all realistic 3D calculations must be numeric. I note that in the 3D case, the current will take the path of least resistance which will reduce the roughness effect. Namba's model (combined with an intrinsic model for $\sigma_{DC}(a)$) does manage to explain strong reductions in the conductivity for extremely thin films that intrinsic models like Fuchs's fail to predict. However one might criticise that at this point the actual model

might have enough free parameters to fit almost any scaling relation, and, since the assumptions are not realistic for a 3D film, the parameters are of limited meaning.

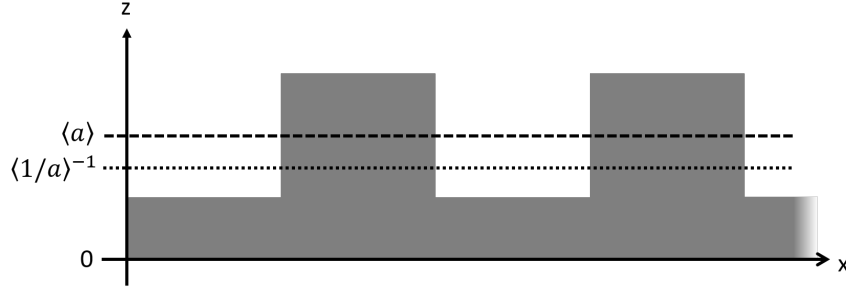


Figure 3.6: Sketch of a very rough film. The measured thickness a of this film will be equal to the arithmetic mean $\langle a \rangle$. In the 2D scenario, the thickness relevant for conduction is the harmonic mean $\langle 1/a \rangle^{-1}$. Since the harmonic mean is always smaller, the average conductivity estimated by assuming $\langle a \rangle$ will be lower than the true conductivity.

3.5.2 Roughness effect on the current response time

Of particular interest is how the roughness of the film affects the measurement of the current response time. For at least a qualitative picture, I extend Namba's model to alternate current conductivity. The AC version of eq. (3.10) yields

$$\tilde{Z} = Z + iX = \frac{1}{B} \int_0^D \frac{1}{a(x)\tilde{\sigma}(a(x))} dx \quad (3.12)$$

Here Z is the real resistance and the reactance X gives the imaginary part of the impedance. With a little complex calculus and eq. (2.35), we find the macroscopic, thickness averaged current response time τ_C extracted from the conductivity phase will be

$$\langle \tau_C \rangle_a = \frac{-1}{\omega} \frac{X}{Z} \quad (3.13)$$

Now, assuming we have effective Drude responses $\tilde{\sigma} = \frac{\sigma_{DC}(a)}{1-i\omega\tau_C(a)}$ with thickness dependent parameters, we get the following expressions for Z and X :

$$Z = \frac{1}{L_B} \int_0^D \frac{1}{a(x)\sigma_{DC}(a(x))} dx = \frac{D}{L_B} \left\langle \frac{1}{a\sigma_{DC}(a)} \right\rangle_a \quad (3.14)$$

$$X = \frac{1}{L_B} \int_0^D \frac{-\omega\tau_C(a(x))}{a(x)\sigma_{DC}(a(x))} dx = \frac{-\omega D}{L_B} \left\langle \frac{\tau_C(a)}{a\sigma_{DC}(a)} \right\rangle_a \quad (3.15)$$

$$\langle \tau_C \rangle_a = \frac{\left\langle \frac{\tau_C(a)}{a\sigma_{DC}(a)} \right\rangle_a}{\left\langle \frac{1}{a\sigma_{DC}(a)} \right\rangle_a} = \frac{\left\langle \frac{R(a)}{a} \right\rangle_a}{\left\langle \frac{1}{a\sigma_{DC}(a)} \right\rangle_a} \quad (3.16)$$

3 Thickness scaling of conduction dynamics

We can see that $\langle \tau_C \rangle_a$ is a combination of averages, whose effects somewhat cancel each other out. The measurement of τ_C is hence relatively unaffected by roughness.

3.5.3 Roughness effect on apparent variation

The ratio $R = \tau_C / \sigma_{DC}$ is connected to the variation C via $R = \frac{1}{W}(1 + C^2)$. Since σ_{DC} will be underestimated in case of a rough film, R and therefore the variation C may be overestimated.

$$\langle R \rangle_a = \frac{\langle \tau_C \rangle_a}{\langle \sigma_{DC} \rangle_a} = \frac{\left\langle \frac{R(a)}{a} \right\rangle_a}{\left\langle \frac{1}{a\sigma_{DC}(a)} \right\rangle_a} \frac{\langle a \rangle_a}{\left\langle \frac{1}{a\sigma_{DC}(a)} \right\rangle_a^{-1}} = \left\langle \frac{R(a)}{a} \right\rangle_a \langle a \rangle_a \quad (3.17)$$

Even when R would not depend on thickness because the variation of relaxation times remained constant, eq. (3.17) shows that the measured ratio $\langle R \rangle_a$ will increase as long as the roughness relative to the mean thickness increases, since we would compare an arithmetic mean to a harmonic one.

3.5.4 Size of the roughness effect

We can quickly estimate the size and scaling of the roughness effect. We assume a model even simpler than Namba's: A wire that is half of height $\langle a \rangle + h$ and half of height $\langle a \rangle - h$, as seen in fig. 3.6. In the 2D case, the effect comes from the comparison of the arithmetic $\langle a \rangle_a$ to the harmonic mean $\left\langle \frac{1}{a} \right\rangle_a^{-1}$. For our simple model, the ratio between these two means is

$$\frac{\left\langle \frac{1}{a} \right\rangle_a^{-1}}{\langle a \rangle_a} = 1 - \left(\frac{h}{\langle a \rangle_a} \right)^2 \quad (3.18)$$

Hence the roughness size effects become important once the roughness h approaches the average thickness $\langle a \rangle_a$. The size of the effect will further be reduced since in 3D, the current will take the path of least resistance, hence thickest portions of the film. We will need to consider the roughness effect only for the thinnest films, but there it will easily dominate any possible quantum effects for realistic roughnesses.

3.6 Summary

In general, the thinner a metal film is, the smaller both its conductivity and its current response time will be. However, the conductivity and current response time will not be exactly proportional, because surface scattering will change the variation of microscopic relaxation times. When the films get so thin that the thickness becomes comparable to the roughness, the intrinsic conductivity may be underestimated.

4 Substrate referenced transmission terahertz time domain spectroscopy

4.1 Accessing conduction dynamics in thin metal films by substrate referenced transmission terahertz time domain spectroscopy

The overall goal of this thesis is to time-resolve the conduction in metals film. I want to gain information that can be directly applied to DC transport at room temperature. Therefore the distribution of electrons probed by the electromagnetic radiation should not deviate strongly from the Fermi distribution present at room temperature in equilibrium. This is ensured by keeping the photon energy below the typical energy of a thermal excitation. This thermal excitation energy corresponds to 6 THz. Relaxation times in metals are believed to be on the order of 10 fs. Hence the necessary time-resolution is on the order of a femtosecond (10^{-15} s). Terahertz time domain spectroscopy has this resolution. Reflection measurements only depend on the conduction quite directly at the surface. Further they have experimental disadvantages in achieving the time-resolution.

Therefore I perform transmission measurements. Free-space terahertz spectroscopy needs samples of an area larger than the THz beam size in the focus, that is larger than ca. 3×3 mm². Few-nanometre metallic films cannot be prepared free standing over such a large area. However, the films can be measured on the substrate they are grown on, as long as substrate transmits terahertz radiation in the desired frequency window. In this case a transmission through a blank substrate must be measured as a reference. I refer to this method as substrate referenced transmission terahertz time domain spectroscopy (SRT THz TDS).

4.1.0.1 Outline

In the following, I will give a brief introduction of terahertz time domain spectroscopy and the experimental set-up I used. Then I will show how the time traces of the terahertz radiation passing the metal film on the substrate can be combined with the measurement of the reference substrate to yield the THz optical properties of the metal film. I will show the general case and derive the analytical formula for the commonly used approximation that the film is in air/vacuum and thin [47]. Here I will start with the general case. Then I will show how much the inevitable difference between the thicknesses of two substrates will influence the recovered conduction dynamics.

4 Substrate referenced transmission terahertz time domain spectroscopy

The thickness difference can be calculated very accurately when the first echo of the terahertz pulse is taken into account for both reference and sample. The trick is to derive a quantity which does not depend on the unknown sample film, leaving the thickness difference as the only unknown variable. I have shown this thickness difference determination for a “thin” film in an optics letter [48]. Here I will expand this method for a thin stack of multiple layers (i.e. the sample film and a capping layer) and for a “thick” metal film. The high refractive index of metals (see fig. 1.4) means that above ca. 20 nm, metal films are no longer “thin” for the 300 μm terahertz waves. The properties optically thin and (highly) conductive are hence almost mutually exclusive. I refer to this fact as the “thin-conductive oxymoron”, and show how the approximation of a thin film can fail quite spectacularly for metal films as thin as 40 nm.

4.2 Terahertz time domain spectroscopy

Terahertz time domain spectroscopy (THz TDS) is based on measuring pulses in the electrical field composed of frequencies around 1 THz as a function of time. This is achieved by splitting a femtosecond laser pulse in two. One pulse generates the terahertz pulse, the other gates the detection of the terahertz radiation. This technique samples the electric field of the terahertz radiation as a function of the delay between the generating and detecting pulses. THz TDS successfully bridges the frequency region of the “Terahertz gap”. This gap appears around 1 THz as signals around this frequency are too high for efficient electrical generation and detection but outside the range of efficient direct optical sources and detectors such as lamps, lasers, and photo-conductors. In this region THz TDS beats the Fourier transformed infrared spectroscopy in terms of dynamic range [49].

However, THz time domain spectroscopy is more than a gap-filler. Since it measures the electrical field as a function of time, it can time-resolve electrical processes. Here, I have to distinguish two limits of time-resolution: First the fastest variation in the electrical signal measurable, which is limited by the highest measurable frequency. Second the smallest measurable difference in lag between two frequency components, either within the same THz pulse or between different pulses. The accuracy of determining these lags depends on how well the delay between the generating and detecting laser pulses is controlled. This timing precision is conceptually independent of the frequency and may exceed the frequency limitation by 3 orders of magnitude or more in a standard THz TDS set-up. This is the precision needed to time-resolve conduction in metal films at room temperature.

4.2.1 Specific set-up used

The set-up I used for the measurements presented in this thesis was designed by Zoltan Mics and Ivan Ivanov. For a detailed description, I refer the reader to Ivan Ivanov’s thesis [50]. The set-up is based on an amplified Ti:Sapphire laser. The laser emits 1000 pulses of 800 nm central wavelength per second. Each pulse is 40 fs long and has a pulse

4.2 Terahertz time domain spectroscopy

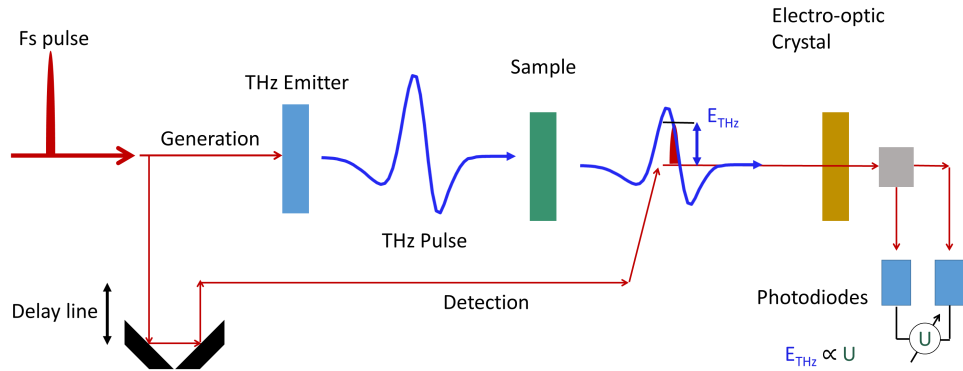


Figure 4.1: Schematic of a terahertz time domain spectroscopy experiment. A femtosecond laser pulse is split into a generation and detection pulse. The generation pulse is converted into a THz pulse in a THz emitter. The THz pulse propagates through a sample and then to a detection crystal. In the detection crystal, the instantaneous field of the THz pulse changes the polarisation state of the detection pulse. The polarisation of the detection pulse is read out as the difference between the voltages of two photodiodes.

energy of ca. $100 \mu\text{J}$. After the pulses are split, the pulse generating the terahertz retains 90 % of the energy, while the detecting laser pulse retains 10 %. Optical rectification of the stronger laser pulse in a 1 mm ZnTe crystal generates a terahertz pulse. The laser pulse is collected, expanded, directed and focussed by a set of parabolic mirrors, first onto the sample position and then onto the detection crystal. The detection crystal is another 1 mm ZnTe crystal. The Pockels effect changes the refractive index of the crystal along the electro-optic axis of this crystal linearly with the applied electric field. By choosing a suitable polarisation of the detection laser pulse with respect to the crystal and the THz axis, the THz electric field co-propagating with the detecting laser pulse through the crystal induces a change in phase in the polarisation component along the electro-optic axis. This adds a circular component to the polarisation of the laser pulse. The pulse then passes a quarter-wave plate. The wave plate turns the linear component into a circular one while the circular component is turned into a linear polarised beam. The polarisation angle of this beam depends on the phase shift received in the detection crystal. A Wollaston prism then analyses the polarisation by directing ordinary and extraordinary beams towards separate photodiodes. The difference in intensity between ordinary and extraordinary beams are directly proportional to the phase shift in the detection crystal as long as those phase shifts are small. The linear relation between phase shift and field means that the intensity difference between the diodes is proportional to the electric field. To increase detection sensitivity, every second THz pulse is blocked by a chopper. This allows to lock onto the modulation of every second detection laser pulse and selectively amplify it. The modulation is integrated over 1 second in the lock-in amplifier before read out. This measurement is

4 Substrate referenced transmission terahertz time domain spectroscopy

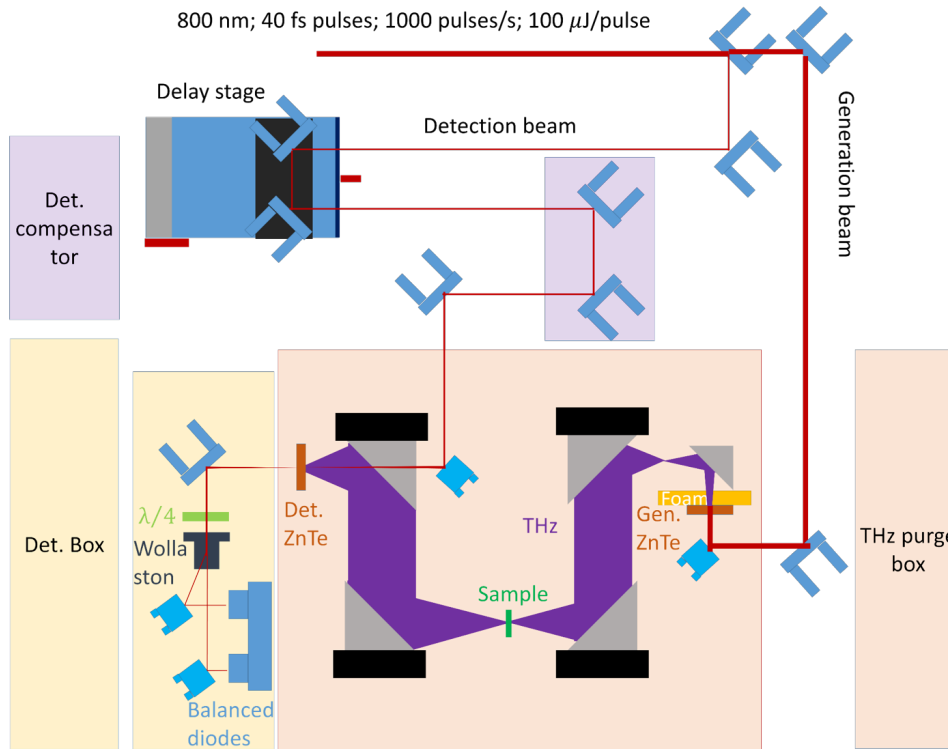


Figure 4.2: Sketch of the terahertz time domain set-up used. The set-up is based on two 1 mm (110) ZnTe crystals to generate and detect THz pulses with femtosecond pulses from an amplified 800 nm laser. The THz pulses are collimated and focussed by parabolic metal mirrors. The sample and the detection crystal sit in the focus points of the THz beam. The entire THz part is enclosed with a box and flushed with dry nitrogen to purge any water vapour from the THz path.

repeated for a range of delays between the generating and detecting laser pulses. The delay is set with a delay stage in the path of the detecting beam. The time steps for the measurements in this thesis are always 50 fs. Figure 4.1 shows the principle of a time domain spectroscopy experiment, fig. 4.2 the specific set-up for this thesis.

4.2.1.1 Time trace of a terahertz pulse

The data recorded with the above-described experiment are voltage differences as a function time delay between THz and detection pulses. I refer to these raw data as time traces. Two typical time traces are shown in fig. 4.3.

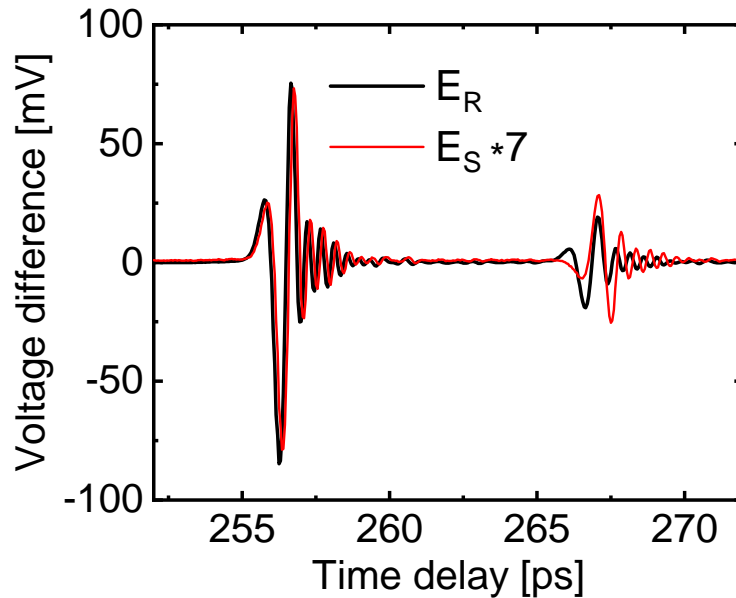


Figure 4.3: Display of two terahertz time traces. The traces represent the voltage difference between the photodiodes as a function of delay line position, expressed in time of flight for light. E_R is a trace taken through a bare 0.5 mm MgO substrate, E_S is the trace acquired after passing through a sample of 10.3 nm iron on top of a similar MgO substrate. E_S was multiplied by 7 for comparability. Two pulses are visible. The first, larger pulse is directly transmitted through the specimen. The smaller pulse arrives ca. 10 ps later. This echo pulse once went back and forth within the MgO substrate. The direct transmissions have the same shape and E_S appears slightly delayed compared to E_R . This delay results from the sample substrate being slightly thicker than the bare reference. The delay is more pronounced for the echo, as the influence of the thickness difference multiplies here. The echo of the reference E_R pulse is smaller but otherwise similar to the directly transmitted pulse. The echo in the sample trace is inverted with respect to the other pulses because it was reflected from the metal film with higher refractive index than the substrate. Since the metal interface is more reflective than the substrate air interface, it is also stronger relative to the direct transmission when compared to the reference.

4.2.1.2 Frequency domain spectra

The spectroscopy part, that is the frequency resolution, is achieved by applying a fast Fourier transformation algorithm to the time domain data ¹. Normally only the first 10 ps window containing the direct pulse is Fourier transformed to avoid Fabry-Perot interference fringes from the echo. As an example, the amplitude spectra for the time traces from figure 4.3 is shown in figure 4.4.

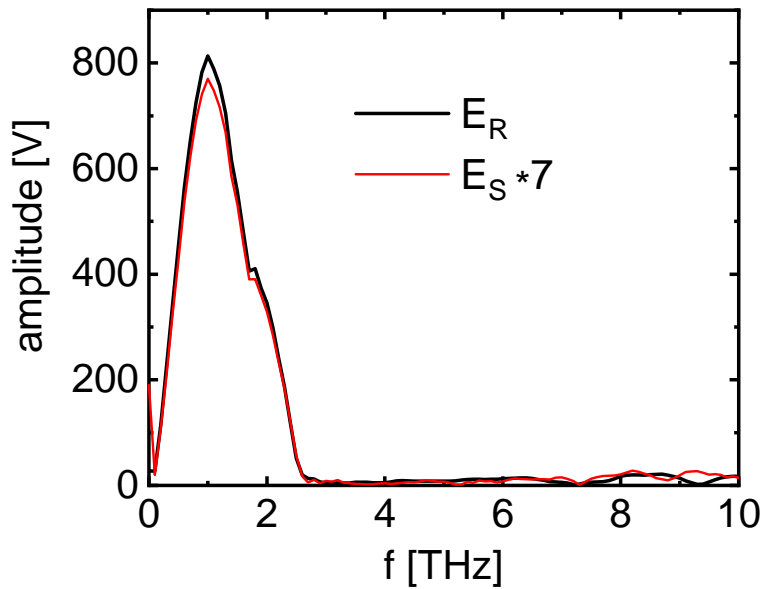


Figure 4.4: Display of two terahertz amplitude spectra from the direct transmission part of the traces shown in fig. 4.3. The sample spectrum is again multiplied by 7. The shapes are almost identical. Only the region between 0.3 and 2.3 THz shows significant amplitude. The reduction of intensity for the spectrometer at low frequencies stem from diffraction effects. The decrease after 1 THz mainly results from worsening phase matching between the laser pulses and the THz pulse. Small features in the spectra are absorption lines of the ZnTe crystals and residual water in the spectrometer. All in all, the spectral shape depends more on the spectrometer than on the samples.

4.2.1.3 Relative transmission

The measured individual spectra are only proportional to the electric field. Further, their shape is mainly determined by the spectrometer response function. In order to

¹Again note the programs written for engineers and mathematicians such as MatLab use conventions leading to an opposite sign of the complex phase. A complex conjugation is necessary to retain the sign conventional in physics.

4.3 Inverting the transfer function

obtain data that has meaning beyond the specific set-up used, any sample spectrum needs to be divided by a reference spectrum. Thereby the detector response function is divided out. Only the complex ratio between the THz fields of the sample and reference experiments remains. This complex-valued relative transmission \tilde{Y} is the most primitive quantity that one can universally compare between different measurement techniques. Figure 4.5 shows the complex THz transmission of the 10.3 nm iron sample relative to the bare MgO reference.

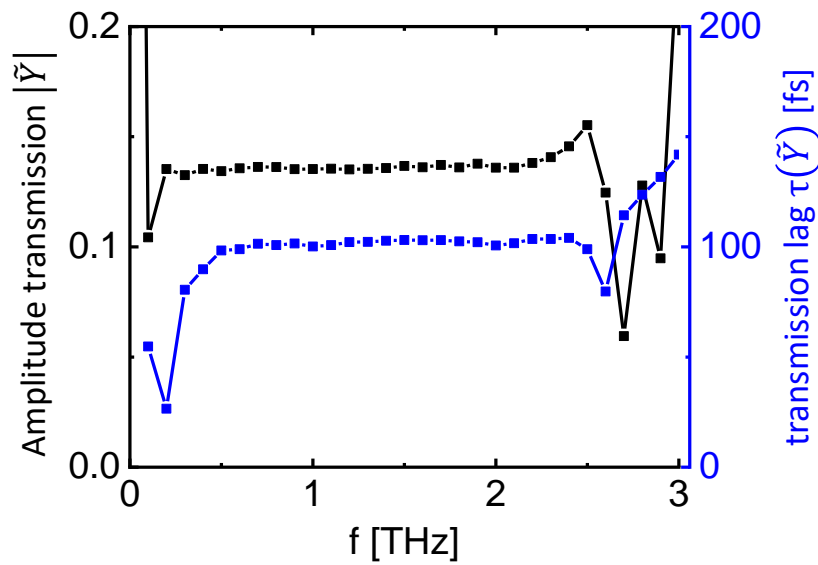


Figure 4.5: Amplitude (left axis, black) and lag (right axis, blue) of the complex transmission \tilde{Y} through a sample relative to a reference. The reference is a bare MgO substrate, the sample a 10.3 nm iron film supported by MgO. The lag is the complex phase divided by the angular frequency. Over a range from ca. 0.6 to 2 THz, both amplitude and lag are almost constant, the amplitude even at a bit lower frequencies. Both quantities fluctuate strongly above 2.3 THz when the end of the spectral range of the spectrometer is reached. From 2.0 to 2.3 THz a slight increase in amplitude is visible. This may be the result of approaching the minimum measurable transmission of the spectrometer.

4.3 Inverting the transfer function

The goal of the measurements is to retrieve material parameters ($\tilde{\sigma}$) from the complex terahertz transmission \tilde{Y} . The general approach is to model the measured samples. The model (characterised by parameters \vec{G}) allows constructing a transfer function $\tilde{Y}(\tilde{\sigma}, \vec{G})$. The transfer function allows predicting the measurement for an accurate

4 Substrate referenced transmission terahertz time domain spectroscopy

model \vec{G} and known material parameters $\tilde{\sigma}$. The challenge is then to invert this transfer function, that is to find the set of parameters $\tilde{\sigma}, \vec{G}$ that have resulted in the measured data. This can be attempted numerically by guessing parameters (in this thesis only $\tilde{\sigma}$), comparing $\tilde{Y}(\tilde{\sigma}, \vec{G})$ with the measured data, improving the guess and iterating to convergence. For some special cases, the transfer function $\tilde{Y}(\tilde{\sigma}, \vec{G})$ can be approximated by a simple algebraic function, which can be analytically inverted. In the case of substrate referenced spectroscopy, the assumption of a film so thin that the phase change during transit is negligible permits the inversion. The assumption that the film is conductive then allows recovering the conduction dynamics and the sheet conductance without knowledge of the exact film thickness a .

4.3.1 Geometry

4.3.1.1 The sample

In substrate referenced spectroscopy the electro-optic properties (refractive index / conductivity) of a supported thin film are measured. The film may be part of a stack of layers on top of the supporting substrate. I will refer to the stack (or film) and the substrate as “sample” and use “sample film” when I address the film only. Figure 4.6 gives a sketch of the general sample. In case a stack is measured, the thicknesses of all layers and the THz refractive indices of all materials except the sample film have to be known or known to be negligible. The measurement of the refractive index of the substrate is described in the appendix section 7.3. This a general description of a sample stack, the specific iron samples investigated in this thesis are described in section 7.2 and sketched in fig. 7.1.

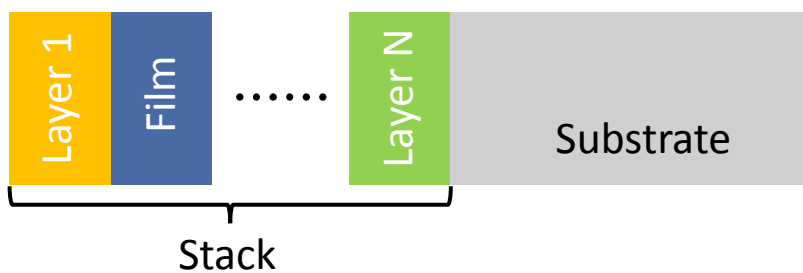


Figure 4.6: Sketch of the type of sample investigated with substrate referenced THz spectroscopy: A sample film whose THz properties are to be determined, supported by a substrate. The film may be part of a stack of other materials whose THz properties are known.

4.3.1.2 Path of the pulse through the sample

In a THz TDS measurement, the electric field recorded after transmission through the sample is compared to the field recorded through a known reference. For substrate

referenced spectroscopy, a bare substrate is used as a reference. I will refer to it simply as reference or reference substrate.

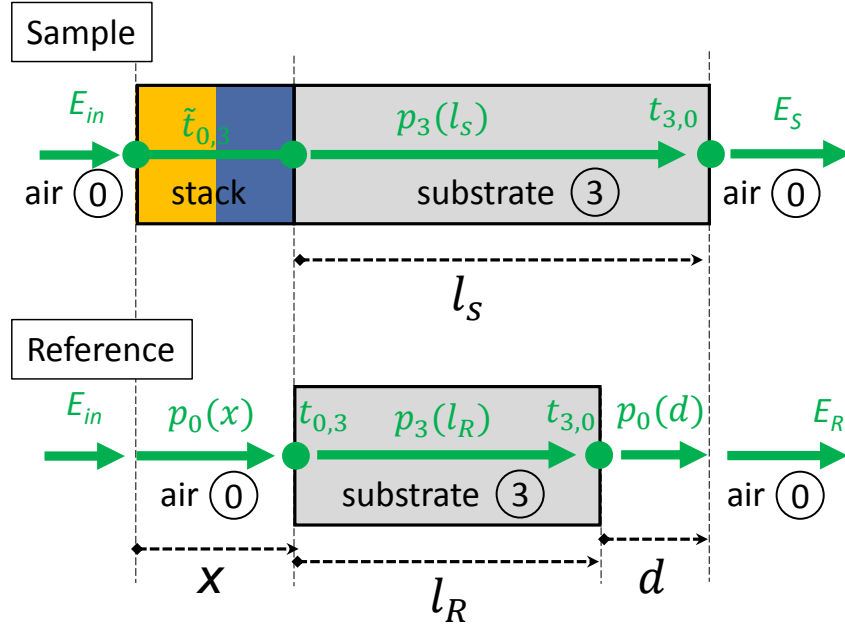


Figure 4.7: Sketch of the beam path through a sample and a bare reference substrate. The transfer functions between the incoming electric field E_{in} and the transmitted fields for sample E_S and reference E_R are the product of the transfer functions of the individual components. Important dimensions are indicated. The figure is not to scale.

The transfer functions of sample and reference give the ratio between the incoming terahertz electric field E_{In} and the transmitted electric field through the sample $E_{S,I}$ and the reference $E_{R,I}$, respectively. The I indicates that only the direct transmissions through the substrates are considered, the echoes can be separated by temporal windowing in time domain spectroscopy when they do not overlap. The transfer function of the entire system can be written as the product of the transfer functions of the components encountered in the path of the terahertz pulse. Fig. 4.7 depicts this path for sample and reference. In the sample, the pulse is reflected multiple times in the iron film and MgO capping layer. I use $\tilde{t}_{0,3}$ to describe this transmission. I denote the propagation factor the substrate as $p_3(l_s)$. Here we only consider the direct transmission. The index 3 indicates the substrate material while l_s is the relevant length. The final transmission from the substrate (3) to air (0) is $t_{3,0}$.

For the reference, the pulse will travel through air (0) for the thickness x of the stack on the sample, marked as $p_0(x)$. $t_{0,3}$ gives the in-coupling from air into the substrate, $p_3(l_R)$ the propagation through the reference and $t_{3,0}$ is again the out-coupling factor. An additional path d is travelled through air to arrive at the same point as the out-

4 Substrate referenced transmission terahertz time domain spectroscopy

coupling position of the sample. This is $p_0(d)$. Note that d can be negative if the sample substrate is thinner than the reference. This yields the following two equations eqs. (4.1) and (4.2):

$$\tilde{E}_{S,I} = \tilde{t}_{0,3} \cdot p_3(l_s) \cdot t_{3,0} \cdot \tilde{E}_{In} \quad (4.1)$$

$$\tilde{E}_{R,I} = p_0(x) \cdot t_{0,3} \cdot p_3(l_s) \cdot t_{30} \cdot p_0(d) \quad (4.2)$$

Here \tilde{E} denotes the spectral densities of the respective E -fields, obtained via Fourier transform (eqs. (1.2) and (1.3)).

With eq. (1.7) this the relative transmission \tilde{Y}_I of the directly transmitted THz pulses is:

$$\tilde{Y}_I = \frac{\tilde{E}_{S,I}}{\tilde{E}_{R,I}} = \frac{\tilde{t}_{0,3}}{t_{0,3}} p_3(d) p_0(-(d+x)) \quad (4.3)$$

While I took care to account for the different distance travelled in the sample with respect to the reference, I will neglect Gouy shifts. Gouy shifts arise because the samples are placed in a focus of the THz beam between two parabolic mirrors, which means that the incident wave is not a plane wave. This leads to Gouy shifts proportional to the differences in the optical lengths of sample and reference [51]. However, the differences in optical lengths are very small compared to the focal lengths of the set up and thus Gouy shifts should be negligibly small.

4.3.2 Transfer matrix method

The transfer matrix gives the general description of a wave propagating through a stack of layers, taking into account all multiple reflections inside the layers. This is necessary when these reflections do not appear as separate echos which we can simply cut out in the time domain. This is the case for the sample stack, which may include capping and buffer layers in addition to the sample layer of interest.

4.3.2.1 Fresnel coefficients

For normal incidence and relative magnetic permeability $\mu=1$, the Fresnel coefficients for transmission $t_{l,m}$ and reflection $r_{l,m}$ for a pulse travelling from material l into material m are [52]

$$t_{l,m} = \frac{2\tilde{n}_l}{\tilde{n}_l + \tilde{n}_m} \quad (4.4)$$

$$\text{and } r_{l,m} = \frac{\tilde{n}_l - \tilde{n}_m}{\tilde{n}_l + \tilde{n}_m}. \quad (4.5)$$

Here \tilde{n}_j is the refractive index of medium j .

4.3.2.2 Transfer matrix

The following section is based on a paper of Katsidis and Siapkas [52]. Please note that they use a Fourier transform convention in which a later signal has a decreased phase, the opposite of what I use here. The transfer matrix \vec{T} yields reflection and transmission of a multi-layered stack taking into account the multiple reflections within the stack. A stack of N layers will have $N + 1$ interfaces. Each layer and each interface is assigned its own transfer matrix. The transfer matrix of the entire stack is the ordered product of all those matrices. The stack commences with an interface. This interface is assigned the index 0. The first layer is denoted as layer 1, the interface between it and the following layer 2 is interface 1. The final N th layer ends with interface N . Such a stack is sketched in figure 4.8.

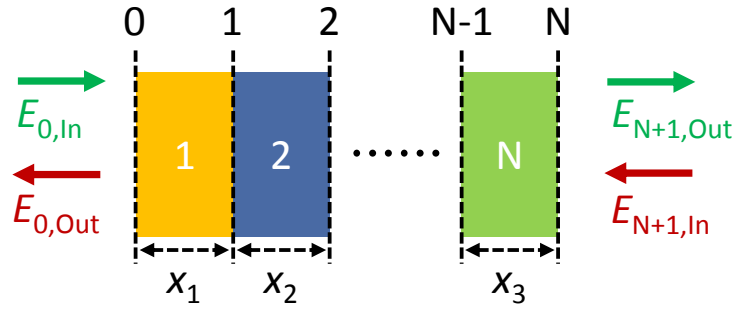


Figure 4.8: Sketch of a stack of N layers with $N + 1$ interfaces. Each layer and each interface is described by a transfer matrix. The transfer matrix of the entire stack is the product of all those matrices. x is the thickness of each layer. E_{In} and E_{Out} mark the incoming and outgoing fields. All fields travelling to the right are marked in green. They will be noted in the first row of the field transfer vector. The red fields are travelling to the left and noted in the second row. The transfer matrix gives the relation between the field transfer vectors directly in front and behind it. Each interface and layer is assigned its own transfer matrix. The transfer matrix of the total stack is the left to right product of the matrices of the components within it.

The transfer matrix $\vec{T}^{(0,N)}$ relates the propagation of the electric fields travelling into (E_{In}) and out of (E_{Out}) the stack on the left (E_0) of the stack to those on the right E_{N+1} . In this formalism, the fields travelling towards the right are denoted in the first row, those travelling to the left in the second row of a field transfer vector². The relation between these two vectors in front of and behind the stack is

$$\begin{pmatrix} E_{0,\text{In}} \\ E_{0,\text{Out}} \end{pmatrix} = \vec{T}^{(0,N)} \cdot \begin{pmatrix} E_{N+1,\text{Out}} \\ E_{N+1,\text{In}} \end{pmatrix} \quad (4.6)$$

²This is NOT the vector of the electric field! I consider only one polarisation here.

4 Substrate referenced transmission terahertz time domain spectroscopy

Reflection and transmission coefficients of the stack are then given by the elements of the transfer matrix

$$\tilde{t}_{0,N+1} = \frac{E_{N+1,\text{Out}}}{E_{0,\text{In}}} = \frac{1}{\tilde{T}_{1,1}^{(0,N)}} \quad (4.7)$$

$$\tilde{r}_{0,N+1} = \frac{E_{0,\text{Out}}}{E_{0,\text{In}}} = \frac{\tilde{T}_{2,1}^{(0,N)}}{\tilde{T}_{11}^{(0,N)}} \quad (4.8)$$

$$\tilde{r}_{N+1,0} = \frac{E_{N+1,\text{Out}}}{E_{N+1,\text{In}}} = -\frac{\tilde{T}_{1,2}^{(0,N)}}{\tilde{T}_{1,1}^{(0,N)}} \quad (4.9)$$

$$\tilde{t}_{N+1,0} = \frac{E_{0,\text{Out}}}{E_{N+1,\text{In}}} = \frac{\text{Det}(\tilde{T}^{(0,N)})}{\tilde{T}_{1,1}^{(0,N)}}. \quad (4.10)$$

Equation (4.7) gives the coefficient \tilde{t}_f needed for the relative transmission in equation (4.3). Reflection and transmission at each interface j are represented by a matrix $\tilde{S}^{(j)}$ and the matrix $\tilde{P}^{(j)}$ gives the propagation through the layer j . The transfer matrix of the entire stack is the product of the transfer matrices of each component of the stack:

$$\tilde{T}^{(0,N)} = \tilde{S}^{(0)} \prod_{j=1}^N \tilde{P}^{(j)} \tilde{S}^{(j)}. \quad (4.11)$$

The propagation transfer matrix $\tilde{P}^{(j)}(x)$ describes the transfer of electro-magnetic radiation between two points spaced by a distance x in substance j . The propagation matrix is connected via the propagation factor p_j (eq. (1.7)) to the refractive index \tilde{n}_j and the thickness x_j of layer j :

$$\tilde{P}^{(j)} = \begin{pmatrix} p_j(-x) & 0 \\ 0 & p_j(x) \end{pmatrix} = \begin{pmatrix} p_j^{\star} & 0 \\ 0 & p_j \end{pmatrix} = \begin{pmatrix} e^{-ik\tilde{n}_j x} & 0 \\ 0 & e^{ik\tilde{n}_j x} \end{pmatrix}. \quad (4.12)$$

The transfer matrix through an interface j between layers j and $j+1$ can be built from Fresnel coefficients. For the transfer matrix I use a shorthand notation assigning only the interface indices to the Fresnel coefficients (eqs. (4.4) and (4.5)), that is $t_{j,j+1} = t_j$ and $r_{j,j+1} = r_j$:

$$\tilde{S}^{(j)} = \begin{pmatrix} 1/t_j & r_j/t_j \\ r_j/t_j & 1/t_j \end{pmatrix}. \quad (4.13)$$

4.3.3 Transfer function

Combining eqs. (1.7), (4.4), (4.5), (4.7) and (4.11) to (4.13) yields the transmission through the stack $\tilde{t}_{0,3}$ as a function of the index of the sample film \tilde{n}_2 .

4.3 Inverting the transfer function

$$\tilde{Y}_{I,calc}(\tilde{n}_2) = \tilde{Y}_{I,Measured} \quad (4.14)$$

$$\tilde{t}_{0,3}(\tilde{n}_2) \frac{p_3(d)p_0(-(d+x))}{t_{0,3}} = \tilde{Y}_{I,Measured} \quad (4.15)$$

Under the assumption that all other parameters are known, this equation can usually be solved numerically for the refractive index of the sample film \tilde{n}_2 . I use a simple procedure by finding the minimum of

$$|\tilde{Y}_{I,calc}(\tilde{n}_2) - \tilde{Y}_{I,Measured}|. \quad (4.16)$$

More sophisticated approaches weighting amplitude and phase differently can be used when needed [53, 54].

I will now consider the more specific case of only a single layer: the sample film with a thickness a . In this case, the transfer function $\tilde{t}_{0,3}$ through the film is [48, 55]

$$\tilde{t}_{0,3} = \frac{2\tilde{n}_0\tilde{n}_2}{\cos(k\tilde{n}_2a)\tilde{n}_2(\tilde{n}_0 + \tilde{n}_3) - i\sin(k\tilde{n}_2a)(\tilde{n}_0\tilde{n}_3 + \tilde{n}_2^2)}. \quad (4.17)$$

This leads to the equation

$$\tilde{Y}_I(\tilde{n}_2) = \frac{\tilde{n}_2(\tilde{n}_0 + \tilde{n}_3)e^{ik(\tilde{n}_3 - \tilde{n}_0)d}e^{-ik\tilde{n}_0a}}{\cos(k\tilde{n}_2a)\tilde{n}_2(\tilde{n}_0 + \tilde{n}_3) - i\sin(k\tilde{n}_2a)(\tilde{n}_0\tilde{n}_3 + \tilde{n}_2^2)} \quad (4.18)$$

for the direct transmission \tilde{Y}_I . I will now show how to retain an analytical formula based on the approximation that the sample film is thin.

4.3.3.1 Thin film approximation

The relevant thickness for this approximation is the optical thickness \tilde{n}_2a of the film. When this is small compared to the THz wavelength, the cosine and sine expressions in eq. (4.18) can be approximated by Taylor expansion to the first order of $k\tilde{n}_2a$ around zero:

$$|k\tilde{n}_2a| < 0.09 \quad \rightarrow \quad |\cos(k\tilde{n}_2a) - 1| < 0.01; \quad (4.19)$$

$$|k\tilde{n}_2a| < 0.39 \quad \rightarrow \quad |\sin(k\tilde{n}_2a) - k\tilde{n}_2a| < 0.01. \quad (4.20)$$

Further the exponential $e^{-ik\tilde{n}_0a}$ is approximated as $1 - ik\tilde{n}_0a$. This will almost always be a good approximation if equations (4.19) and (4.20) hold, since \tilde{n}_2 is typically larger than \tilde{n}_0 . This yields the expression

$$\tilde{Y}_I = \frac{(\tilde{n}_0 + \tilde{n}_3)e^{ik(\tilde{n}_3 - \tilde{n}_0)d}(1 - ik\tilde{n}_0a)}{(\tilde{n}_0 + \tilde{n}_3) - ika(\tilde{n}_0\tilde{n}_3 + 1) + Z_0\tilde{\sigma}a}. \quad (4.21)$$

4 Substrate referenced transmission terahertz time domain spectroscopy

Here I have used eq. (1.6) to replace the refractive index \tilde{n}_2 of the sample film by the complex conductivity $\tilde{\sigma}$ of the film. $Z_0 = \frac{1}{\epsilon_0 c_0}$ is the impedance of free space.

$$\tilde{\sigma} = \frac{\tilde{n}_0 + \tilde{n}_3}{Z_0 a} \left[\left(\frac{e^{ik(\tilde{n}_3 - \tilde{n}_0)d}}{\tilde{Y}_I} - 1 \right) - ika \left(\tilde{n}_0 \frac{e^{ik(\tilde{n}_3 - \tilde{n}_0)d}}{\tilde{Y}_I} - \frac{1 + \tilde{n}_0 \tilde{n}_3}{\tilde{n}_0 + \tilde{n}_3} \right) \right]. \quad (4.22)$$

This formula is not given in the usual overviews and derivations [56–58]. It is, however, more general and helps to illuminate the additional approximation of the film being highly conductive.

4.3.3.2 Thin conductive film approximation

I will use the case of the surrounding medium being air or dry nitrogen ($\tilde{n}_0 = 1$) to simplify eq. (4.22)

$$\tilde{\sigma} Z_0 a = (1 + \tilde{n}_3) \left[\left(\frac{e^{ik(\tilde{n}_3 - 1)d}}{\tilde{Y}_I} - 1 \right) (1 - ika) \right]. \quad (4.23)$$

Here the conductive film approximation assumes that ka is negligible while $\tilde{\sigma} Z_0 a$ is not. Therefore $|Z_0 \tilde{\sigma}| \gg k$ must be fulfilled, which is the same as $|\tilde{n}_2| \gg 1$. Using this approximation (keeping \tilde{n}_0 general) yields

$$\tilde{\sigma} = \frac{\tilde{n}_0 + \tilde{n}_3}{Z_0 a} \left(\frac{e^{ik(\tilde{n}_3 - \tilde{n}_0)d}}{\tilde{Y}_I} - 1 \right). \quad (4.24)$$

This equation, often referred to as “thin film equation” or “Tinkham approximation” [57], is very commonly used for thin films. The equation provides a simple formula to calculate the conductivity $\tilde{\sigma}$ from the measured field transmission \tilde{Y}_I . I will use this approximation in the following to obtain starting values for the numerical solution of eq. (4.16). Within this approximation, the exact film thickness a is not important for recovering the dynamics of the sheet conductance $\tilde{\sigma} a$. Note that the combination of the approximations that the film is thin concerning the optical phase shift ($|k\tilde{n}_2 a| \ll 1$) and that it is conductive $|\tilde{n}_2| \gg 1$ means that $ka \ll |k\tilde{n}_2 a| \ll 1$. Therefore this thin conductive film formula (4.24) only applies to extremely thin metal films. The section “Thin conductive oxymoron” shows how quickly this approximation fails and what errors arise from failure.

4.4 Substrate thickness correction

In the following section, I will present how to obtain the thickness difference with a precision of better than 100 nm from the same THz transmission measurement I use to extract the conductivity³. The only requirement is that in addition to the direct transmission, the time trace of the first echo is recorded.

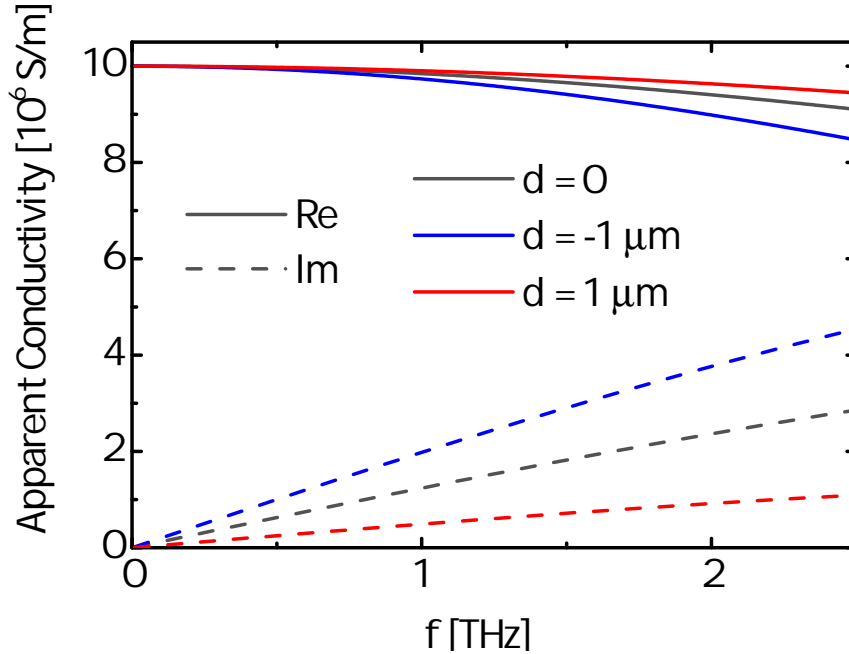


Figure 4.9: Influence of $1 \mu\text{m}$ thickness difference on the apparent conductivity of a 10 nm film with 100 ms DC sheet conductance. Full lines denote the real, dashed the imaginary part of the conductivity. The black lines indicate the true spectrum, blue the conductivity spectrum recovered when neglecting $-1 \mu\text{m}$ thickness difference and red results from neglecting $1 \mu\text{m}$ of thickness difference

4.4.1 Substrate thickness difference

I will illustrate the effect of the substrate thickness difference on the apparent complex conductivity by a simple method:

1. Chose a sample reference pair of a certain geometry, complex conductivity and thickness difference.
2. Compute the field transmission of this pair using eq. (4.14).
3. Neglect the thickness difference when recovering the complex conductivity.

I consider a sample stack of thickness a as the only layer on top of a substrate that is d thicker than the reference. I assume a measurement in air ($\tilde{n}_0 = 1$) and use $\tilde{n}_3 = 3.24$ for the substrate index (see section 7.3). This value is an approximation of the index spectrum of magnesium oxide. I keep the thickness of the film a at a constant 10 nm within this section. The conductivity is assumed to be of a Drude spectral shape, eq. (2.44), with a DC-conductivity σ_{DC} and a response time τ_D .

³in the case of the MgO substrates I investigated

4.4.1.1 Basic impact of variations in substrate thickness

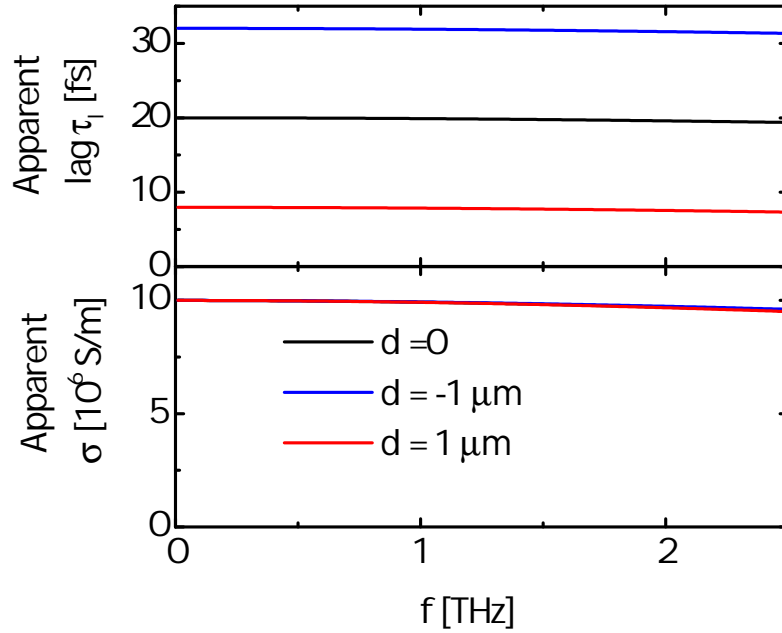


Figure 4.10: Influence of $1 \mu\text{m}$ thickness difference on the apparent conductivity of a 10 nm film with 100 ms DC sheet conductance. The top graph displays the measured lag τ_l , the bottom graph the conductivity amplitude σ . The black lines indicate the true spectra, dashed blue the lag τ_l and amplitude σ spectra recovered when neglecting $-1 \mu\text{m}$ thickness difference and dashed red results including the systematic error from neglecting $1 \mu\text{m}$ of thickness difference.

Figures 4.9 and 4.10 illustrate the impact of a sample substrate $1 \mu\text{m}$ thicker or thinner than the reference ($d = 1 \mu\text{m}$ respectively $-1 \mu\text{m}$) on the measurement of a sample film with a σ_{DC} of 10^7 S/m and $\tau_D = 20 \text{ fs}$. I chose the conductivity close to that of perfect bulk iron, $\tau_D = 20 \text{ fs}$ is a realistic estimate for a thin metal film. Figure 4.9 shows the resulting apparent complex conductivity in terms of its real and imaginary parts. Figure 4.10 displays the same conductivities in terms of conductivity amplitude σ and lag τ_l . 4.10. Here the impact of the thickness difference on the measured timing τ_l becomes directly obvious. The thickness difference basically shifts the recovered lag by a constant time, roughly 12 fs in this example. The effect on the apparent amplitude is hardly visible and probably too small to be resolved within experimental accuracy.

4.4.1.2 Thickness difference indistinguishable from response time

The change in lag by thickness difference seen in 4.10 is almost indistinguishable from a different current response time. I illustrate this by comparing the lag measured for a film with 20 fs response time neglecting 1 μm thickness difference to the true lag of a film with 8 fs response time in fig. 4.11. Both films have a DC-conductivity of 10^7 S/m.

The absolute conductivity is even less distinguishable since it is hardly affected by response time or thickness difference. The following problems arise from this difficulty to distinguish Drude response times from thickness difference effects:

1. Response time⁴ data reported without the thickness difference determined may not be trustworthy.
2. The uncertainty of the thickness difference limits the accuracy of the measured response time. The current state of the art precision leaves at least 10 fs systematic error [32, 59].
3. Even if a Drude shape conductivity is assumed, fitting the apparent conductivity with the thickness difference as a free parameter will leave several fs of uncertainty on the response time, since thickness difference and current response time correlate strongly.

A possible example of this be seen in comparing literature data from Hilton *et.al.* [60] and Bonetti *et.al.* [9]. In both cases the THz transmission experiments are only side notes, not key to the papers. Nevertheless Hilton's 70 fs Drude response time for a 12 nm iron film do not agree well with Bonetti's 30 fs for a 9 nm iron film, especially considering Hilton's film is less than half as conductive as Bonetti's and hence would be expected to have a shorter Drude response time. Neither work makes any statement regarding the expected precision of their measurements.

The slight differences between true lag of the 8 fs film and the distorted lag of the 20 fs film increase with frequency (see fig. 4.11). The differences result from terms proportional to $(\omega\tau_D)^2$. Therefore a larger bandwidth is always helpful to distinguish the two cases. Further very large distortions will be more obvious. Still ca. 1 fs precision on the response time measurements will be required. I will, therefore, give a brief overview of how much systematic error to expect for a given thickness difference. This will depend on the (DC) conductivity σ_{DC} and thickness a of the film. I will limit this discussion to thin films where only the sheet conductance $\sigma_{DC} \cdot a$ matters⁵.

⁴often referred to as relaxation time or scattering time in the respective publications

⁵These are thicknesses below 20 nm for typical metals, see page 89 *f.*

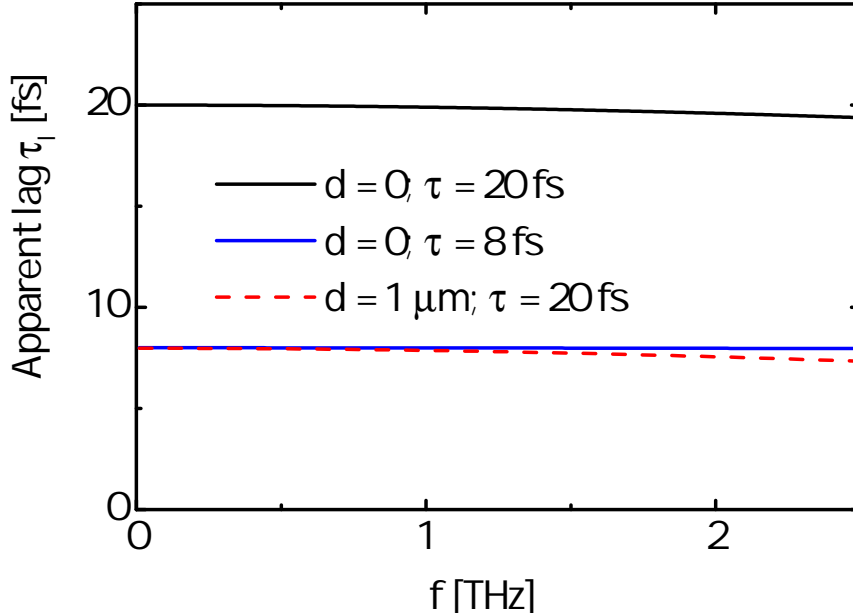


Figure 4.11: The systematic error from 1 μm thickness difference makes a film with 20 fs current response time almost indistinguishable from a conductivity with 8 fs response time. The film is a 10 nm thick with 100 mS DC sheet conductance. The true lag τ_l for 20 fs current response time τ is indicated by a black line. The blue line indicates the true lag for 8 fs response time. The dashed red line results from neglecting 1 μm of thickness difference when recovering the conductivity shown in black.

4.4.1.3 Sheet conductance impacts thickness difference effect

Staying with 10 nm thick films, a silver film retaining bulk properties would have the highest possible sheet conductance of 630 mS. The lowest sheet conductance of any film presented in this thesis is ca. 4 mS for 2.2 nm of iron. However, other samples under investigation by THz time domain spectroscopy include graphene sheets with typical sheet conductances of 0.1 to 1 mS and topological insulators with even lower sheet conductances. Figure 4.12 shows how differently $d = 1 \mu\text{m}$ thickness difference affects the apparent lag in films of different sheet conductance.

The general trend is that the lower sheet the conductances the larger the thickness difference error will become. Between 4 and 1 mS a drastic change happens, where the apparent lag stays no longer flat and the apparent amplitudes sky rockets. This threshold coincides with the value of $\frac{1}{Z_0} \approx 2.7 \text{ mS}$, which is not surprising considering eq. (4.24).

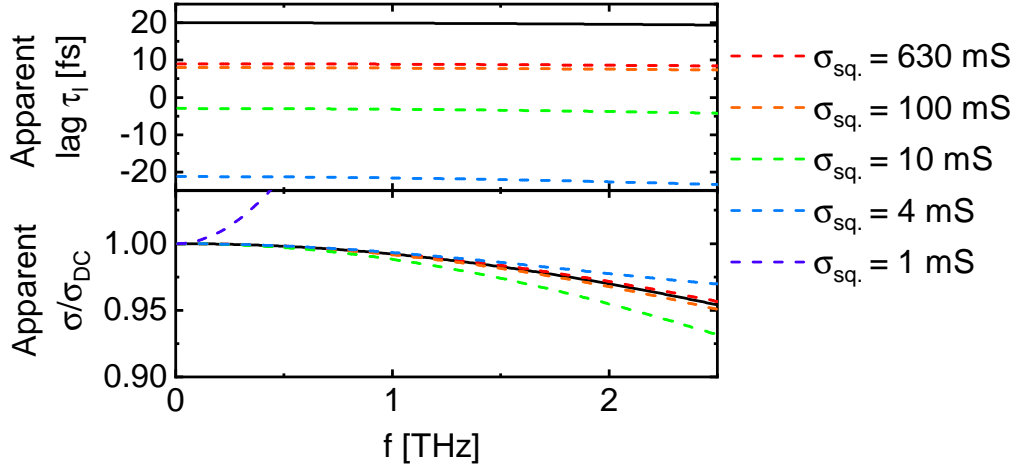


Figure 4.12: The systematic error from 1 μm thickness difference changes for different sheet conductances. The film is a 10 nm thick with 20 fs response time. The true lag τ_l and conductivity amplitude are indicated by black lines. The dashed colourful lines denote the apparent lags and conductivity amplitudes resulting from neglecting 1 μm thickness difference for films from 630 to 1 mS of sheet conductance. The lower the sheet conductance the larger the resulting error on the lag. For 1 ms the apparent lag is off the chart at less than -100 fs and the apparent amplitude also quickly deviates beyond the frame.

4.4.1.4 Necessary precision

I aim for 1 fs precision on the measurement of the lag. The sheet conductance of each film will impact how precise the thickness difference measurement needs to be for the respective sample. In general, better than 100 nm precision is necessary. For the lowest sheet conductance measured for this thesis (4 mS), 20 nm precision on the thickness difference suffice. Fig. 4.13 illustrates this point. The figure is based on the same film parameters as fig. 4.12 except for reducing d to 20 nm.

Note that the impact of the thickness difference also depends on the substrate index \tilde{n}_3 . The additional lag of the relative field transmission due to the thickness difference d is $(\tilde{n}_3 - \tilde{n}_0)kd$. In addition, the relative impedance of the film $Z_0\tilde{\sigma}a$ is compared to that of the substrate in eq. (4.24). I remind that the above estimations have been made for metal films on MgO. In case films of much lower sheet resistance or substrates of very different refractive index were to be used, estimations for the impact of the thickness difference should be redone.

For error estimates on the complex conductivity, I propagate the uncertainties of the respective thickness difference using the geometry of the respective sample. Note that uncertainties on the refractive index of the substrate will change the estimated thickness

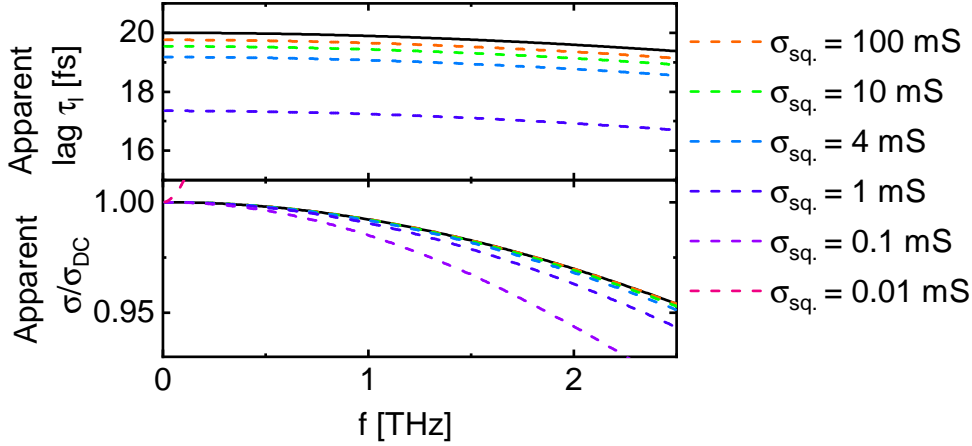


Figure 4.13: The systematic error from 20 nm thickness difference changes for different sheet conductances. The film is a 10 nm thick with 20 fs response time. The true lag τ_l and conductivity amplitude are indicated by black lines. The dashed colourful lines denote the apparent lags and conductivity amplitudes resulting from neglecting 20 nm thickness difference for films from 100 to 0.01 mS of sheet conductance. Between 100 and 4 ms, neglecting 20 nm of thickness difference results in less than 1 fs error on the lag. For 1 ms the apparent lag is already off by 4 fs, for all lower conductances the apparent lag lies below the limits of the graph. Conductivity amplitudes are less affected, only for 0.01 mS the apparent amplitude severely deviates from the true one.

difference by a much larger degree than they change the thickness corrected response time.

4.4.2 Measuring the substrate thickness difference with the echo

I need better than 100 nm accuracy on the thickness difference to obtain the 1 fs timing resolution on the conductivity dynamics. Several methods exist in literature to obtain accurate thickness differences, though exact accuracy estimates are rarely published.

1. Manufacturing sample and reference on the same piece of substrate, tightly spaced [58]. In an advanced step, two reference areas on both sides of the sample film allow a correction to any linear skewness of the substrate.
2. Measuring the thickness of the bare sample and reference substrates with THz-TDS before the deposition of the sample film [33].
3. Measuring the thickness difference afterwards by a different method, i.e visible optical metrology [61].

4.4 Substrate thickness correction

The accuracy of option 1 depends on the local thickness variation of the substrate. Typically the accuracy on the response time is limited to 10 fs or more [32, 59]. Option 2 requires to track any possible changes to the optical thickness of the sample during sample deposition, i.e. by polishing, etching, buffer layers, and heat treatment. Mechanical measurements are usually not precise enough for option 3 and every optical measurement has the difficulty that the influence of the capping layer has to be discounted. Options 1 and 2 need samples purpose-built for THz spectroscopy. The thickness difference needs to be known prior to the THz measurement with the required accuracy. The required accuracy for a target response time again depends on the (THz) properties of the sample film (see fig. 4.12). This is a complicated, possibly recursive process. Option 3 allows measuring the thickness difference even after the measurement of the THz transmission. However it requires a separate experimental technique, and there may not be a universal technique for every type of sample. The echo method of thickness difference determination I developed works with the same THz time domain transmission measurement that will be used to obtain the terahertz properties of the sample film. Therefore my echo method requires neither a different type of measurement nor additional THz measurements nor purpose-built samples. The echo method merely requires that the first echo from the reflection within the substrate must be measurable and distinct. This method has the potential to measure large amounts of sample films in a short time and to be used easily in addition to other methods on the same samples.

4.4.2.1 Beam path of the echo

Comparing echo and direct transmission allows eliminating the sample film properties from the transfer function and hence measure the thickness difference. The paths of the terahertz pulses E_{Out} for echo (index II) and direct transmission (index I) are shown in fig. 4.14.

4.4.2.2 Transfer function of the echo

Tracing the path of the pulse, the relative transfer function of the echo is derived similarly to the direct transmission eq. (4.3). Here, I repeat the eq. (4.3) for the sake of comparability.

$$\tilde{Y}_I = \frac{\tilde{E}_{S,I}}{\tilde{E}_{R,I}} = \frac{\tilde{t}_{0,3}}{t_{0,3}} p_3(d) p_0(-(d+x)) \quad (4.25)$$

$$\tilde{Y}_{II} = \frac{\tilde{E}_{S,II}}{\tilde{E}_{R,II}} = \tilde{Y}_I \frac{\tilde{r}_{3,0}}{r_{3,0}} p_3(2d) \quad (4.26)$$

4 Substrate referenced transmission terahertz time domain spectroscopy

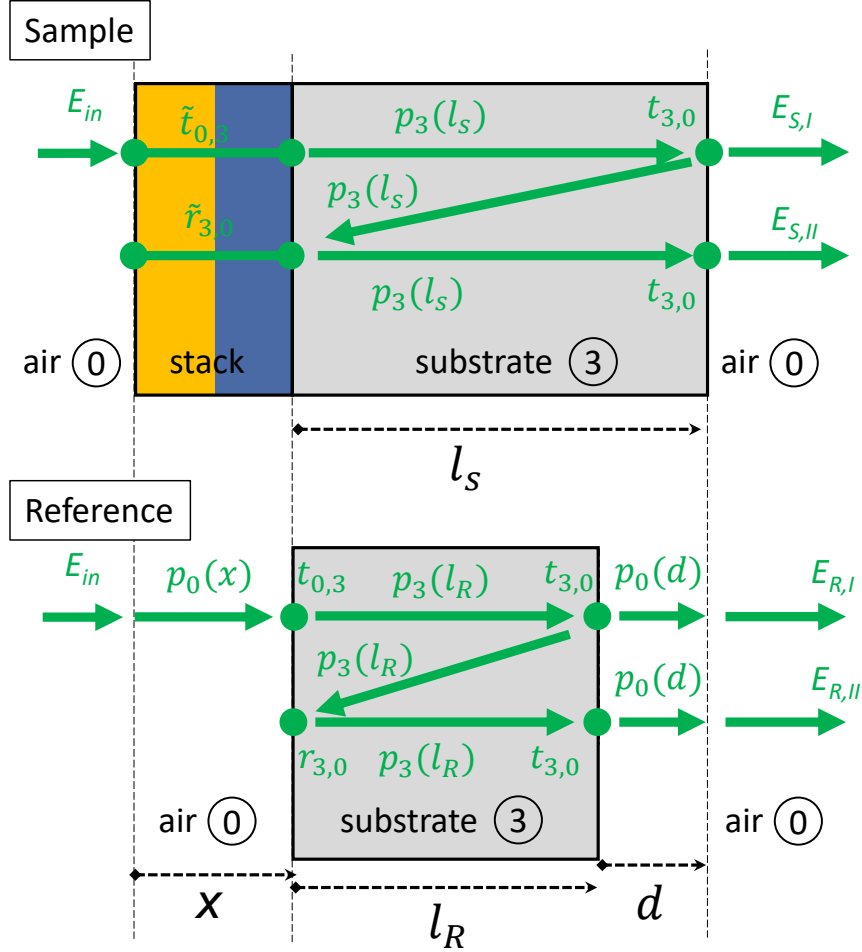


Figure 4.14: Sketch of the beam path of the direct transmission (I) and the first echo (II). The additional path of the echo is shifted down for display. The important lengths are indicated.

4.4.3 Thin stack approximation

Two relations exist for transmission and reflection from a single interface between layers l and m :

$$t_{l,m} = t_{m,l} \frac{\tilde{n}_l}{\tilde{n}_m} \quad (4.27)$$

$$r_{l,m} = t_{l,m} - 1 \quad (4.28)$$

When the stack is thin enough, these relations also apply to the transmission \tilde{t} and reflection \tilde{r} through the stack. When this is the case, eq. (4.25) yields an expression for $\tilde{t}_{0,3}$. With eqs. (4.27) and (4.28), this expression can be inserted into eq. (4.26). This yields

4.4 Substrate thickness correction

$$r_{3,0}\tilde{Y}_{II} = \tilde{Y}_I p_3(2d) [\tilde{Y}_I t_{3,0} p_3(d) p_0(-(d+x)) - 1]. \quad (4.29)$$

Here I used eq. (4.27) again to convert $t_{0,3}$ into $t_{3,0}$. Since the stack is thin, x can be neglected. Inserting the refractive indices and rearranging gives

$$\frac{\tilde{Y}_{II}}{\tilde{Y}_I} (\tilde{n}_3 - \tilde{n}_0) - 2\tilde{n}_3 \tilde{Y}_I e^{ikd(\tilde{n}_3 + \tilde{n}_0)} + (\tilde{n}_3 + \tilde{n}_0) e^{2ikd\tilde{n}_3} = 0 = Q. \quad (4.30)$$

This equation appears as eq. (13) in an optics letter published as part of this PhD project [48]. In the letter, I derived it for the case of a single thin film, not a stack. In the letter, n_1 denotes the index of air while I use \tilde{n}_0 in this thesis. I solve eq. (4.30) for the thickness difference d by numerically searching the minimum of $|Q|$ for each frequency step between 0.5 and 2.0 THz. An example of $|Q(d)|$ from a measurement of the 10.3 nm iron sample referenced to the reference substrate A is displayed in fig. 4.15. I use the minimisation algorithm built into MatLab to find the minimum of $|Q|$. More advanced numerical methods [53, 54] to find the roots of a complex expression like Q might help in more complicated cases.

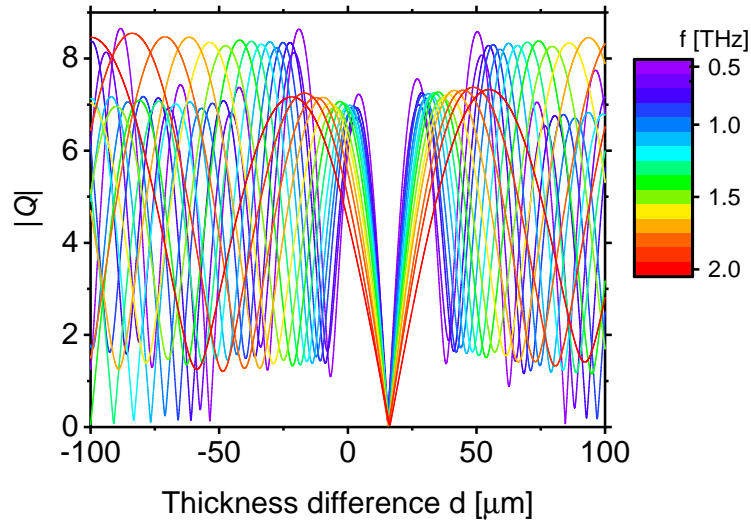


Figure 4.15: Expression $|Q|$ as a function of thickness for a measurement of the 10.3 nm iron sample reference to substrate A. The common minimum for all frequencies yields the correct value of the thickness difference. Suitable boundaries should be chosen for the minimisation algorithm to avoid getting stuck in local minima at some frequencies.

4.4.3.1 Arbitrary angles of incidence

This thesis only deals with normal incidence, but this method can be generalised to arbitrary angles of incidence. Equation (4.29) holds for all angles of incidence Θ_0 when the appropriate Fresnel factors for the respective polarisation and the general version of propagation factors are used: $p_l(y) = e^{iky\tilde{n}_l \cos(\Theta_l)}$. Θ_l is can be derived from Θ_0 with Snell's law of refraction.

4.4.4 Thick conductive film approximation

As stated earlier, metals have a very large refractive index in the terahertz range. In case of iron, an $a = 20$ nm thick film is the limit for which the thin-film approximation (eq. (4.24)) can still be applied to recover conductivity data, see page 89. Therefore I expand the thickness correction method for a film where the terahertz phase change and/or absorption are no longer small during a single pass of the pulse. Here I consider just a single sample film, not a stack of several layers including the sample film. I justify this with the negligible contribution of any thin capping layer compared to the thicker sample film. Starting with equations eqs. (4.25) and (4.26) I use the expressions for the transmission $\tilde{t}_{0,3}$ (eq. (4.7)) and reflection $\tilde{r}_{3,0}$ (eq. (4.9)) through the film to obtain the two expressions [48]:

$$\frac{1}{\tilde{Y}_I} = \underbrace{\frac{p_0(a+d)p_3(-d)}{\tilde{n}_3 + \tilde{n}_0}}_{A_I(d)} \cdot \left[\cos(k\tilde{n}_2 a)(\tilde{n}_3 + \tilde{n}_0) - i \sin(k\tilde{n}_2 a) \left(\frac{\tilde{n}_0 \tilde{n}_3}{\tilde{n}_2} + \tilde{n}_2 \right) \right] \quad (4.31)$$

$$\frac{\tilde{Y}_{II}}{\tilde{Y}_I^2} = \underbrace{\frac{p_0(a+d)p_3(d)}{\tilde{n}_3 - \tilde{n}_0}}_{A_{II}(d)} \cdot \left[\cos(k\tilde{n}_2 a)(\tilde{n}_3 - \tilde{n}_0) - i \sin(k\tilde{n}_2 a) \left(\frac{\tilde{n}_0 \tilde{n}_3}{\tilde{n}_2} - \tilde{n}_2 \right) \right]. \quad (4.32)$$

I combine these two equations to separate the influence of the sample film from the thickness difference:

$$B_+ = \frac{1}{\tilde{Y}_I A_I(d)} + \frac{\tilde{Y}_{II}}{\tilde{Y}_I^2 A_{II}(d)} = 2\tilde{n}_3 \left[\cos(k\tilde{n}_2 a) - i \sin(k\tilde{n}_2 a) \frac{\tilde{n}_0}{\tilde{n}_2} \right] \quad (4.33)$$

$$B_- = \frac{1}{\tilde{Y}_I A_I(d)} - \frac{\tilde{Y}_{II}}{\tilde{Y}_I^2 A_{II}(d)} = 2 \left[\cos(k\tilde{n}_2 a) \tilde{n}_0 - i \sin(k\tilde{n}_2 a) \tilde{n}_2 \right]. \quad (4.34)$$

Now comes the ‘‘conductive’’ approximation. When dealing with a metal sample film, the refractive film \tilde{n}_2 will be much larger than the other indices \tilde{n}_3 and \tilde{n}_1 . Further even though $k\tilde{n}_2 a$ may be large, ka must be small because otherwise the film would not transmit any terahertz radiation. Therefore the term $\sin(k\tilde{n}_2 a) \frac{\tilde{n}_0}{\tilde{n}_2}$ in equation (4.33) can be neglected. I then express $\cos(k\tilde{n}_2 a)$ as function of B_+ :

4.5 Measurements of the thickness difference

$$\cos(k\tilde{n}_2 a) = \frac{B_+}{2\tilde{n}_3}. \quad (4.35)$$

This in turn allows to express B_- in terms of B_+ , thus eliminating the unknown index \tilde{n}_2 :

$$B_- = \frac{B_+ \tilde{n}_0}{\tilde{n}_3} - 2i \sqrt{1 - \left(\frac{B_+}{2\tilde{n}_3}\right)^2} \frac{\arccos\left(\frac{B_+}{2\tilde{n}_3}\right)}{ka}. \quad (4.36)$$

This equation is solved similarly to equation (4.29) by numerically finding the minimum of

$$Q_2 = \left| B_- - B_+ \frac{\tilde{n}_0}{\tilde{n}_3} + 2i \sqrt{1 - \left(\frac{B_+}{2\tilde{n}_3}\right)^2} \frac{\Re\left[\arccos\left(\frac{B_+}{2\tilde{n}_3}\right)\right] + i \Im\left[\arccos\left(\frac{B_+}{2\tilde{n}_3}\right)\right]}{ka} \right|. \quad (4.37)$$

Here I force the real and imaginary parts of \tilde{n}_2 to be positive, which is a physical necessity in a metal. This is necessary as the computer may otherwise select the negative branch of the arccos function.

Note that the values obtained for the film index \tilde{n}_2 are only rough estimates, which work well enough to obtain the thickness difference, but should not be used to characterise the film properties.

4.5 Measurements of the thickness difference

In this section, I present the thickness difference measurements between a set of iron films on magnesium oxide and bare magnesium oxide references. First I give the specific statistical methods I used to obtain the values for the thickness difference. Then I will display the values for the thickness difference I use for further analyses. Lastly, I will show that the conductive and thin approximations result in values within each others confidence intervals. This indicates that the thin stack approximation holds for the thickness difference estimation for much thicker films than for the conductivity estimation.

4.5.1 Precision estimation

Each pair of sample and reference measurements yields m_f values d_j for the thickness difference. m_f is the number of frequency steps within the frequency range of optimal phase resolution. This range spans from 0.6 to 2.0 THz for the spectrometer I use. I repeated the measurement pairs 10 to 30 times. That makes between 140 and 420 measurements M of the thickness difference for each sample. I use an $m = 52\%$ trimmed mean to estimate the sample mean to have a robust estimator⁶. For this

⁶Estimates using this trimmed mean are robust to both outliers and distribution types; a few outliers hardly affect the estimate. Trimming by $m = 52\%$ is chosen as to allow efficient estimation of the central values of Gaussian (ideal 0%), Cauchy (ideal 70%) and exponential (ideal 99.9%) distributed measurements

4 Substrate referenced transmission terahertz time domain spectroscopy

estimation technique, all values d_j are ordered by size. Then the lowest and highest $N = \lfloor mM/2 \rfloor$ values are discarded. The mean of d is then estimated as:

$$d = \frac{1}{M - 2N} \sum_{j=N}^{M-N} d_j \quad (4.38)$$

$$\Delta d = \frac{1}{1 - m} \sqrt{\sum_{j=N}^{M-N} \frac{(d - d_j)^2}{(M - 2N - 1)(M - 2N - 2)}} \quad (4.39)$$

Δd is the estimate for the error between the mean of the sample of M measurements and the population mean. I based its formula on the standard error of the arithmetic mean. I confirmed that eq. (4.39) yields the 68 % confidence interval for the trimmed mean for samples of above 100 normal distributed randomly generated numbers.

4.5.2 Measurement and statistical precision

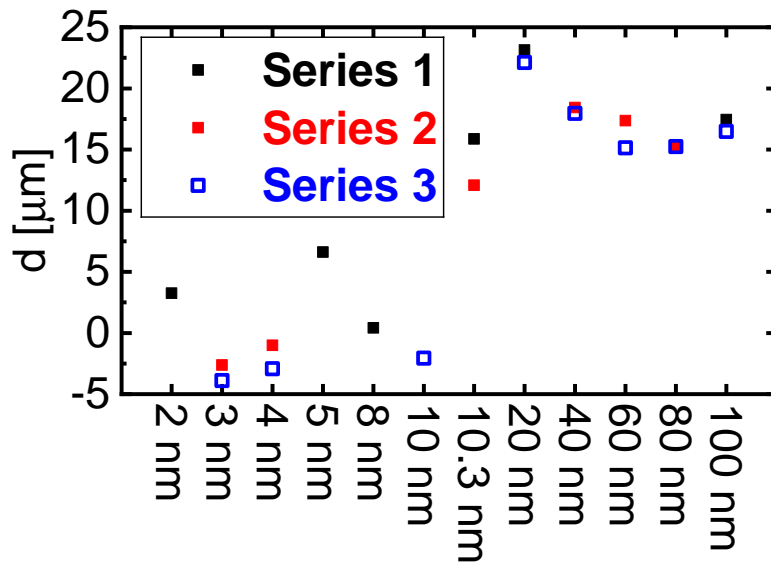


Figure 4.16: Thickness differences between samples and reference substrates. The rounded metal thickness is used to identify the samples. The samples were measured in three separate measurement runs. Series 2 and 3 used a different substrate than series 1. The thickness apparently vary by ca. 30 μm .

Three series of measurements were taken, each almost a year apart from each other. Further the reference substrate was changed from series 1 to series 2. Table 7.1 in section 7.4 lists the samples measured in each series.

4.5 Measurements of the thickness difference

Fig. 4.16 shows that thicknesses between the double polished MgO samples vary by about $30 \mu\text{m}$. This makes thickness difference correction necessary. For these MgO substrates, no values for the local thickness variation are available. The wafer-to-wafer variation is specified as $20 \mu\text{m}$. Even comparing the same substrates and samples can lead to a few μm difference, probably due to local thickness variations or sample ageing effects.

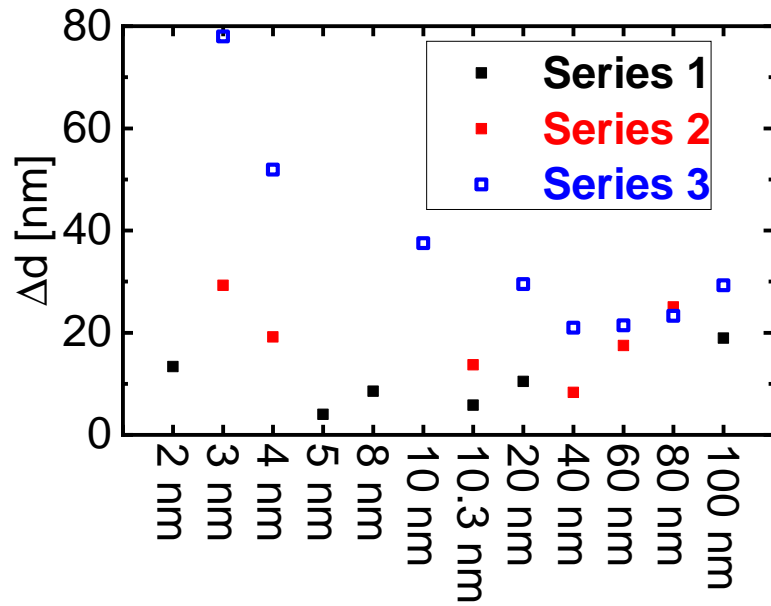


Figure 4.17: Statistical errors estimated for the thickness differences between substrate and sample. The rounded metal thickness is used to designate the samples. All errors are below 80 nm, most below 20 nm. Series 1 has the lowest errors, series 3 the highest.

The statistical errors of the thickness determination are displayed in fig. 4.17. All errors are below 80 nm. Series 1 has the smallest errors. The primary reason is that all measurements of series 1 consist of 30 repetitions. Within series 2, the number of repetitions was decreased to 10 repetitions, because other error sources usually dominated the uncertainty of the lag of the conductivity. Only in the case of the 3 nm sample, the error induced by the uncertainty of the thickness difference in the lag exceeds 1 fs and is dominant. This happens because the 3 nm iron films conductance roughly matches the terahertz impedance between the MgO substrate and the surrounding air (eq. (4.40)), thus acting as an antireflection coating [58]. The antireflection condition is [58]:

$$\tilde{n}_3 - \tilde{n}_0 = Z_0 \tilde{\sigma} a \quad (4.40)$$

With for MgO ($\tilde{n}_3 \approx 3.2$) and air ($\tilde{n}_0 = 1$) the left hand side yields ≈ 2.2 while for the 3

4 Substrate referenced transmission terahertz time domain spectroscopy

nm film $Z_0\sigma_{DC}a$ is approximately 2.8. The thinner 2 nm film has a much lower value, all other films much higher values. The antireflection effect is a weakness of my thickness correction approach, but it will only impact a small range of sheet conductances. The results will still be competitive with the previous state of the art methods.

On the other hand, the highest precisions obtained are roughly 4 nm, which allows better than 0.1 fs resolution on the lag. With larger bandwidth and more repetitions (or signal), few attosecond precision may be feasible with the echo correction method.

4.5.3 Comparing thin and conductive approximations

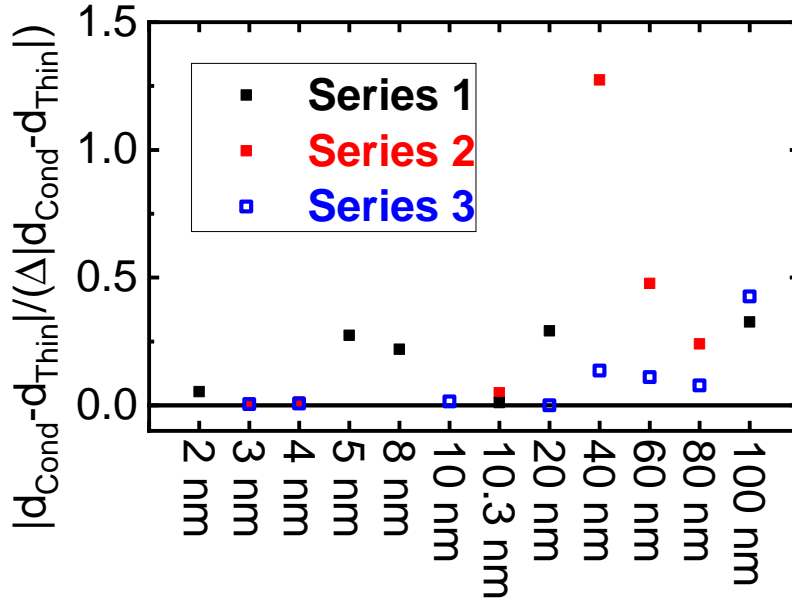


Figure 4.18: Systematic difference between conductive film approximation and thin stack approximation relative to the respective statistical error of the difference. Only the 40 nm series 2 measurement has deviation between the two that is larger than its statistical error. For the currently achievable precision, the simpler thin stack approximation can be used for all thicknesses.

Lastly, I will show that even for films too thick for the requirements of eq. (4.20), the thin film/stack approximation is accurate enough to determine thickness differences within the statistical precision of the measurement. Figure 4.18 shows the difference $d_{\text{Cond}} - d_{\text{Thin}}$ between the two approximations relative to the statistical uncertainty of this difference. Only for the measurement of the 40 nm in the second series the two approaches deviate by more than the statistical error. I also note that I cannot detect a systematic pattern for the $d_{\text{Cond}} - d_{\text{Thin}}$, i.e. the differences fluctuate randomly

from positive to negative. For the currently achievable precision, the simpler thin-stack approximation can be used for all thicknesses.

4.6 The thin conductive oxymoron

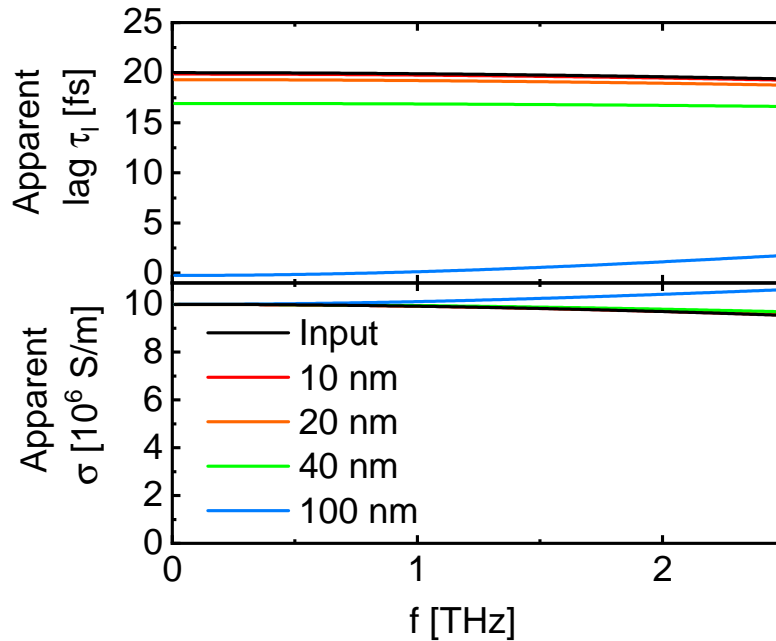


Figure 4.19: Apparent lag and conductivity amplitude recovered with the thin film approximation for a material of $\sigma_{DC} = 10 \cdot 10^6$ S/m and $\tau_D = 20$ fs depending on film thickness. Black lines denote the input, colourful lines the apparent values for 10, 20, 40 and 100 nm. 10 nm almost coincides the input, 20 nm has a lag that is less than 1 fs smaller. The 40 nm film results in already 3 fs of systematic error on the lag, while spectral shape and amplitude are still as the input. For 100 nm spectral shape and amplitude also significantly deviate.

While the thickness difference recovered under the assumption of a thin stack appears to be still valid for iron films of 100 nm, the complex conductivity recovered under the same assumption will significantly deviate for iron films above 20 nm of thickness. To illustrate this, I again perform consistency checks similar to those for the thickness difference on page 75:

1. Chose a complex conductivity, thickness and substrate index.
2. Compute the field transmission for this film using eq. (4.14).

4 Substrate referenced transmission terahertz time domain spectroscopy

3. Apply the thin conductive formula eq. (4.24) when recovering the complex conductivity.

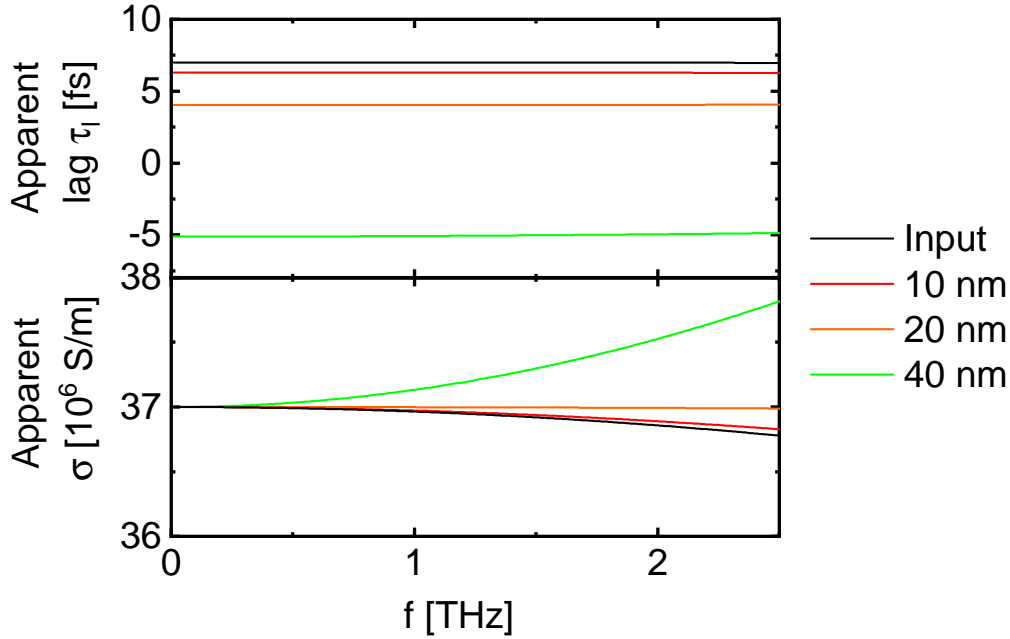


Figure 4.20: Lag and conductivity recovered by thin-film approximation for films of 37 MS/m conductivity and 7 fs response time. The thicker the film, the more the lag decreases. Since in this case the conductivity amplitude also increases, the apparent conductivity resembles that of partially localised charge carriers.

The apparent conductivity recovered for a material with σ_{DC} of $10 \cdot 10^6 \text{ S/m}$ and a Drude response time τ_D of 20 fs is shown in fig. 4.19 for thicknesses from 10 to 100 nm . For 10 nm the deviation is almost invisible. For 20 nm the change in the apparent lag is still smaller than 1 fs . For 40 nm the error on the lag increased to 3 fs , while spectral shape and amplitude remain unchanged. Therefore such an error could not be seen from the spectra alone. The thin film approximation can lead to a distorted shape and amplitude for much thicker films, seen in the case of the 100 nm film.

The distortion of the spectral shape of the apparent conductivity towards decreasing response time and increasing amplitude can lead to the display of the hallmarks of confined charge carriers. As an example, I show the case of a material with simple Drude conductivity with $37 \cdot 10^6 \text{ S/m}$ and a response time τ_D of 7 fs in fig. 4.20. Here the larger conductivity leads to larger error in the apparent lag for the same thickness. For 40 nm the lag already turns negative. The distortion of the spectral shape fits the Drude-Smith model [62, 63] for partially confined carriers as seen in fig. 4.21. The

4.6 The thin conductive oxymoron

Smith's modification of Drude's model for the conductivity of partially confined charge carriers is the following equation:

$$\tilde{\sigma}_{DS} = \frac{\sigma_{DC}}{1 - i\omega\tau_{DS}} \left(1 - \frac{C_{DS}}{1 - i\omega\tau_{DS}} \right) \quad (4.41)$$

Since I picked the conductivity and response time from the DC-conductivity and the optical/infrared response time of aluminium [15], misinterpreting the failure of the thin-film approximation for a 40 nm aluminium film as bound charge carriers in a metal is a realistic possibility.

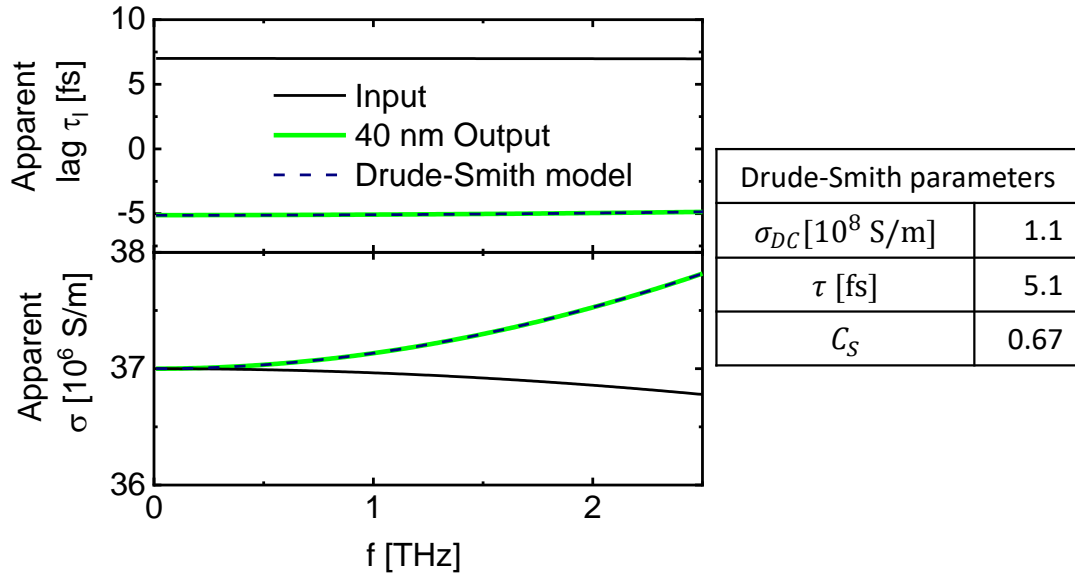


Figure 4.21: Lag and conductivity recovered by thin-film approximation for a 40 nm film of 37 MS/m conductivity and 7 fs response time. The shape of the apparent conductivity resembles that of partially localised charges, empirically often described by the Drude-Smith model. The model fits reasonably well and would mislead to the interpretation that 2/3 of the charge carriers are confined, not free.

5 Conduction dynamics in thin iron films

Here I will present the results of the substrate referenced transmission terahertz time domain spectroscopy measurements on 12 iron films between 2.2 and 100 nm thickness. I will start by describing the epitaxy of the iron films on MgO and the characterisation measurements determining the exact thickness and crystallinity. With the basic properties of the samples established, I will discuss the THz conductivity spectra. Here we see that they roughly follow the effective Drude model eq. (2.36). However, since I achieved 1 fs statistical precision, systematic distortions of the spectra by up to ca. 3 fs become apparent. Comparing measurements of different samples under the same experimental conditions to measurements of the same sample under different conditions shows that the distortions are experimental artefacts. We can adequately describe the spectra using a current response time and a DC-conductivity, as predicted by the effective Drude model eq. (2.36). The thickness scaling of these two parameters is the main focus of our analysis. For iron films on MgO, several thickness-dependent measurements of the DC-conductivities exist. Like ours, they show decreased conductivity with decreasing thickness, however, the exact scaling varies widely. Our iron films are among the most conductive, especially the thinner films. This reaffirms the quality of our films. For the current response time τ_C , we are able to resolve decreasing response times for decreasing thicknesses clearly. Only two data points exist for comparison, as only two THz measurements have been previously published. Both report much larger values for the response time at comparable thicknesses, potentially due to substrate thickness errors. The only thickness scaling of the response time for a metal film has been published for gold films on silicon. These films are extremely rough and polycrystalline. Within the 10 fs accuracy of these measurements, no thickness dependence had been observed. The accuracy of the current response time measurements in this thesis is not only high enough to resolve thickness scaling, but even to resolve that the scaling of the response time differs from that of the conductivity, i.e. the ratio between response time and conductivity is not constant.

The variation of this ratio with thickness reflects the thickness-dependent distribution of relaxation times: the response time depends on the variation of the distribution of relaxation times, and the variation of this distribution depends on thickness.

The variation decreases with decreasing thickness down to ca. 10 nm, increasing again afterwards. This is consistent with anticorrelated surface scattering reducing variation until surface scattering becomes the dominant mechanism and its anisotropy increases variation between scattering times. Comparing the ratio between response time and conductivity with a literature value calculated from the band structure allows

5 Conduction dynamics in thin iron films

estimating the variation of relaxation times.

The data and discussion presented in this chapter appear in a recently published letter [64], though in a bit less detail.

5.1 Preparation and characterisation of the iron films

The preparation and characterisation of the iron films was performed at the IPCM Strassbourg by Eric Beaurepaire, Jacek Arabski and Guy Schmerber, including the analyses of the data.

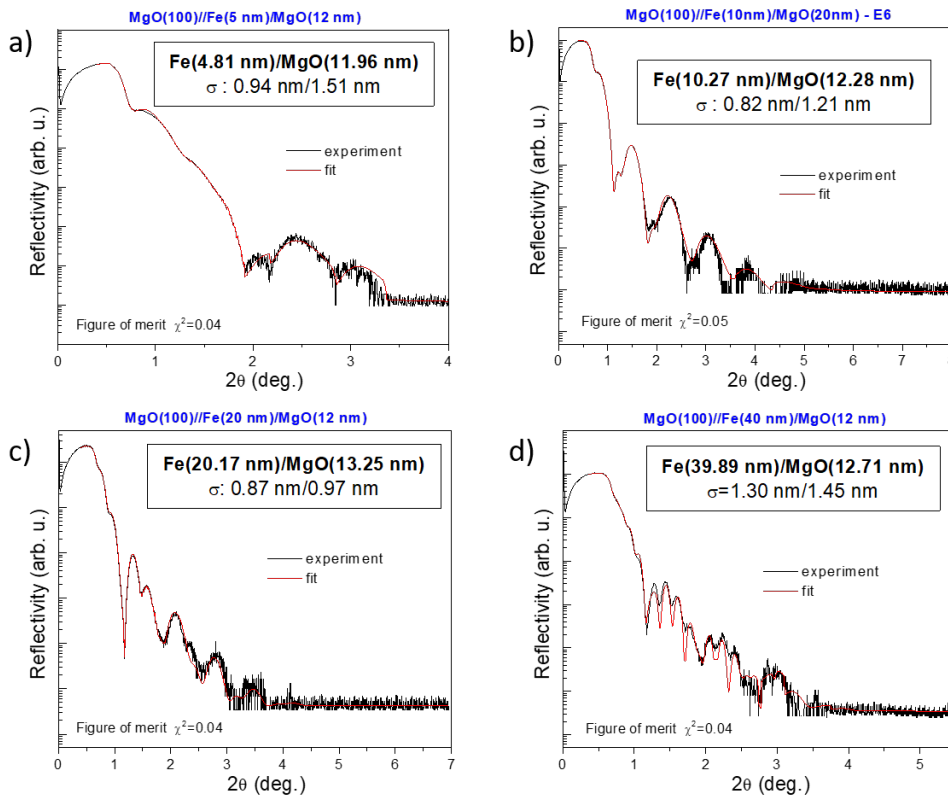


Figure 5.1: X-ray reflectivity measurements of selected iron films. Experimental data shown in black, a fit for a system of two layers (one iron, one MgO capping) in red. The four fit parameters are the thicknesses and roughnesses (here σ) of the layers. The maximum figure of merit χ^2 for the fits is 0.04. Panel a) shows the nominally 5 nm thick film, b) a nominally 10 nm thick film (10.3 in the following), c) the nominally 20 nm thick film and d) the nominally 40 nm thick film. The nominal values come from deposition time and in situ quartz balance measurements. XRD values deviate by up to 0.3 nm from them.

5.1 Preparation and characterisation of the iron films

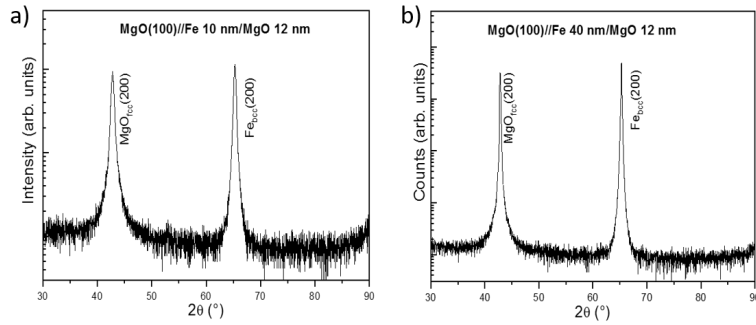


Figure 5.2: X-ray diffraction pattern of two iron films at large angles. a) Shows the diffractogram for the 10.3 nm film, b) for the 40 nm film. The peak around 43 degrees corresponds to (twice) the lattice constant of a face centred cubic (fcc) MgO lattice in (100) direction. The peak at 65 degree corresponds to (twice) the lattice constant of a base centred cubic (bcc) iron lattice in the same direction. No other peaks are visible, indicating only one crystal facet of the iron film in the system.

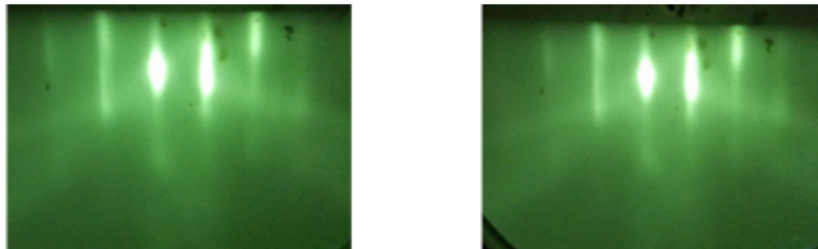


Figure 5.3: Images of reflected high energy electrons diffracted from the surface of the during iron deposition. The images indicate epitaxial uptake of iron.

The iron films were deposited on double-polished magnesium oxide (MgO). The MgO surface was oriented in the (100) direction of the crystal lattice. Iron was epitaxially grown on this surface by molecular beam epitaxy. The epitaxy was achieved by a deposition rate of 0.05 nm per minute in a vacuum of 10^{-8} Pa pressure onto a substrate at room temperature. The film thicknesses were monitored in situ by a quartz crystal microbalance (QCB) and reflection high energy electron diffraction measurements. The samples were subsequently annealed at 600 K and capped with 12 nm of MgO.

After the preparation, the thickness of selected samples was measured by small-angle X-ray diffraction (XRD) by a Rigaku SmartLab X-ray diffractometer with a monochromatic Ge(220)x2 source delivering a copper $K_{\alpha 1}$ incident beam (45 kV, 200 mA, $\lambda = 0.154056$ nm). Fig 5.1 shows the X-ray diffractograms. Thicknesses extracted from XRD deviate between 0.1 to 0.3 nm from the QCB measurements, with a standard

5 Conduction dynamics in thin iron films

deviation of 0.2 nm. XRD has a precision of ca. 0.1 nm, and I use the more precise XRD data when existent. The thickness of all other films is the QCB value, with standard deviation to XRD of 0.2 nm as error estimate. The roughnesses of the films extracted from XRD average to 0.9 ± 0.1 nm. The roughness does not depend systematically on thickness. I assume this value for all films. X-ray (fig. 5.2) and reflection high energy electron diffractograms (fig. 5.3) indicate single-crystalline films with base centred cubic (bcc) lattice structure.

From what this characterisation can tell us, we have a single crystalline orientation of the films and we know the average film thickness $\langle a \rangle$ with 0.1 to 0.2 nm precision. However, roughnesses of 0.9 nm indicate differing heights on the order of 2-3 atomic layers. For a sketch of the samples, see section 7.2.

5.2 Conductivity spectra of the iron films

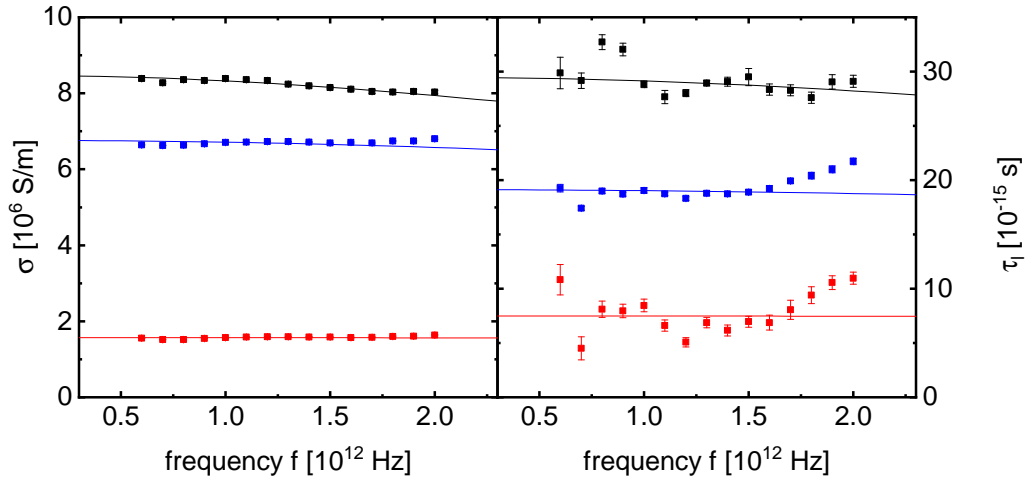


Figure 5.4: 3 example complex conductivity spectra for the 100 (black) 10.3 (blue) and 2.2 (red) nm films. The left panel shows the conductivity amplitude σ , the right panel the lag τ_l . Lines indicate effective Drude models (eq. (2.36)) derived from the data. Error bars indicate standard errors of the mean derived from repeated measurements. Where invisible, the error bars are smaller than the markers.

As explained in chapter 4, an individual transmission measurement of a given specimen consists of recording the electric field transmitted through the specimen and through a reference substrate. This transmission measurement is then repeated several times. The measurements on the iron films were performed on three separate occasions, hereafter referred to as series. The first series was measured in August 2016, the second in August

2017 and the third in June 2018, as samples became available. Series 1 measurements were repeated 30 times, the following series 10 times, after learning from series 1 that the statistical precision was not the limiting factor. Table 7.1 lists the samples measured in each series. In total, most samples were measured twice.

5.2.1 Example spectra

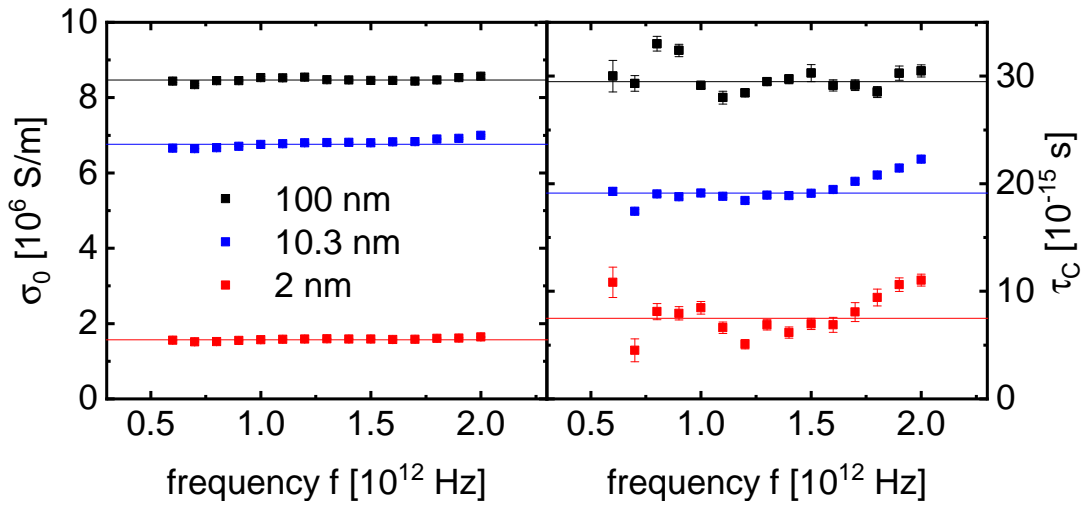


Figure 5.5: 3 example complex conductivity spectra for the 100 (black), 10.3 (blue) and 2.2 (red) nm films. The left panel shows the DC conductivity estimate σ_0 for each frequency, the right panel the current response time τ_C . Lines indicate effective Drude models (eq. (2.36)); which are spectral averages of the data.

Using the method discussed in chapter 4, I recovered THz conductivity spectra from each of these measurements. I only use the data from the range of highest phase resolution between 0.6 and 2 THz as in chapter 4. As an example, I show 3 spectra from the first series in fig. 5.4. I plot the spectra in terms of conductivity amplitude σ and lag τ_l . The statistical error on the lags is mostly less than 1 fs, and so is the systematic one from the thickness difference. This is at least 10 times more precise than the few previous measurements on thin metal films, and means that we have a time resolution comparable to intrinsic time scale of the electrical conduction itself. The rest of this thesis now focusses on what we can learn from the resolved conduction dynamics, in the framework of chapters 2 and 3.

All three samples show traces roughly agreeing with the effective Drude model eq. (2.36). I hence extract the current response time τ_C at each frequency point. These current response time values are then averaged (weighted by their statistical precision) for each spectrum. This spectral average $\bar{\tau}_C$ is my estimator for the current response time. From there, I obtain an estimate σ_0 for the DC conductivity at each frequency point

5 Conduction dynamics in thin iron films

via:

$$\sigma_0(\omega) = \sigma(\omega) \cdot \sqrt{1 + (\omega\bar{\tau}_C)^2} \quad (5.1)$$

The combined dc-conductivity estimate $\bar{\sigma}_{DC}$ is then the spectral average over $\sigma_0(\omega)$. Fig 5.5 shows the spectra for τ_C and σ_0 . Their difference to the lag and amplitude spectra is minute, just the slight decrease towards lower frequencies has vanished.

The following observations can already be made from the spectra alone:

1. The spectra are roughly constant, but they are not constant within their statistical error.
2. Both response time and conductivity decrease with decreasing thickness, but they are not directly proportional to each other.

Item 2 will be discussed in the thickness scaling sections 5.3 and 5.4. First, I will investigate whether the two constants current response time and DC conductivity suffice to describe the conduction.

5.2.2 Residual correlation

In fig. 5.5, the spectra of the current response time and the DC-conductivity are not constant within the statistical error estimated from repeated measurements. I note that the deviations on the response time are better visible in the plot, but the deviations of the conductivity are similarly significant due to much smaller statistical errors. Further, the data deviates systematically from the constant lines, for example, both the 10.3 nm and the 2 nm current response time increase in a similar manner from 1.5 THz onwards. To investigate this behaviour, I plot the differences between the individual data points and their respective averages for all measurements in fig. 5.6.

The figure 5.6 shows that the residuals of different samples performed in the same series strongly correlate. The residuals of the same sample measured in different series do not. This leads me to the conclusion that the residuals are the results of measurement artefacts characteristic to the series rather than any intrinsic properties of the iron films. The conduction dynamics within my measurement range can therefore be represented by the two parameters DC conductivity $\bar{\sigma}_{DC}$ and current response time $\bar{\tau}_C$. The question left to answer is: How much do the artefacts impact the measurement of these spectral averages? I will focus the discussion on the response time, the conductivity was handled in a similar manner. I estimate the impact of the artefacts in two ways: First by taking into account the reduced sum of residuals to estimate the statistical error on the average. Second I use the differences between the spectral averages of the same samples measured in different series. The statistical error on the measurements lead to errors between 0.2 and 1.2 fs.

5.2 Conductivity spectra of the iron films

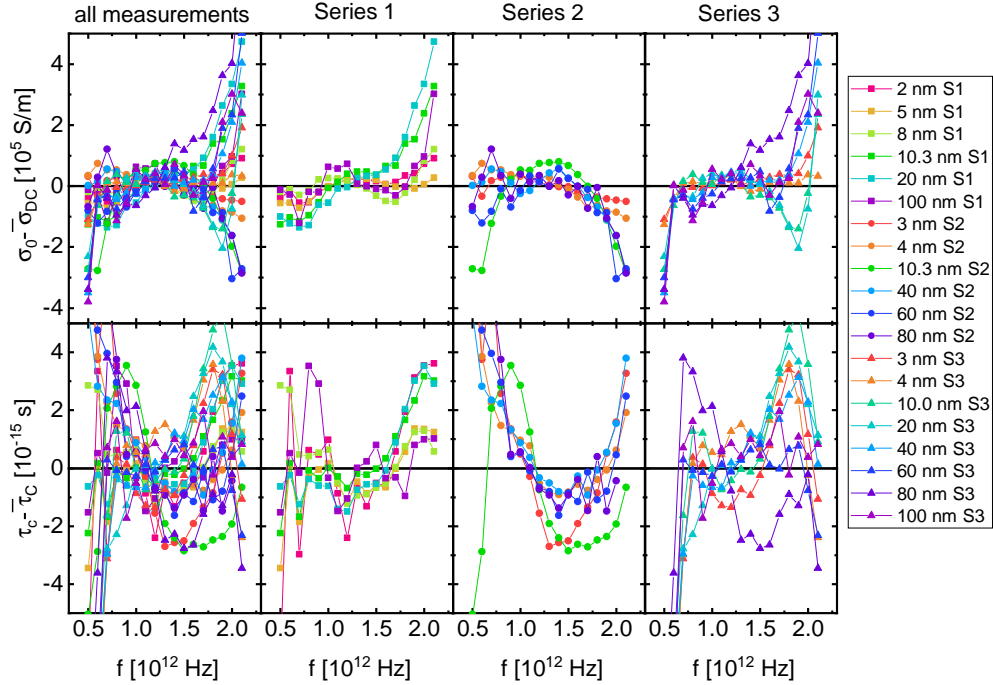


Figure 5.6: Spectra of the residuals of the spectral averages. Upper panels show the differences between the DC conductivity estimates $\sigma_0(f)$ and their spectral averages $\bar{\sigma}_{DC}$. Lower panels show deviations of the current response times $\tau_C(f)$ from their spectral averages $\bar{\tau}_C$. The first column shows the residuals of all spectra combined, columns 2 to 4 show each the spectra from a single measurement series. Strong similarities between the measurements of the same series are apparent, but no correlation between different series in general and or between the same samples or samples of similar thickness specifically are visible (similar thicknesses are indicated by similar colour). The residuals are hence artefacts specific to the respective measurement series.

The differences between measurements of the same sample are between 0 and 2.6 fs, their standard deviation is ca. 1.7 fs. This is somewhat larger than what to expect from the statistical error, even when factoring in the additional error from the substrate thickness correction. Therefore, for the samples with more than one measurement, the measurements are averaged and the differences taken into account to determine the error.

The average additional error deduced from comparing several measurements of the same sample is 0.8 fs, and this average value is added into the error estimate for the samples with only one measurement. Additionally, systematic errors from inaccuracy of the substrate index are factored in, for thick films also any uncertainties on the film

5 Conduction dynamics in thin iron films

thickness.

The biggest error contributions are the errors inferred from the residuals and the differences between repeated measurements. Only in case of the 3 nm sample, the error from the substrate thickness difference surpasses them. For future improvements in accuracy, these artefacts have to be targeted. For the conductivity, for some of the thicker films the differences between repeated measurements matter, but for all thinner films the uncertainty of the film thickness is the major source of error.

5.2.2.1 Origin of the artefacts

As mentioned above, the result of a measurement in one series was not reproduced within statistical precision in the next. This is both true for the average values as for the shape of the residual spectra. In general, the fact that the series were measured at least 10 months apart from each other gives the possibility of sample ageing. The samples were kept for ca. 90 % of the time in a dry nitrogen atmosphere to prevent the iron from rusting and especially the MgO from taking on water. Samples with visible damage from age or handling were not remeasured, but most samples did survive. Further, the conductivity did not systematically decrease over time, which would be expected from rusting. The 12 nm MgO capping layer apparently sufficed to keep the iron films quite stable. Hence we can rule out ageing as the main cause of the differences between series. Also, while the measurements were performed on the same sample, they were not done on the exact same spot. This may cause some discrepancies, but it does not explain the correlations between the residuals within one series. Occam's razor leads me to assume that whatever causes these artefacts most likely also caused the differences of the spectral averages. This must be something that was the same for all measurements of a given series. Only two things come to mind: First the state of the spectrometer, that is its transfer function, and second the reference substrate. I note that the substrate for series 1 was a different piece of MgO than for series 2 and 3, but since 2 and 3 also differ, that alone does not suffice. The substrate may have aged between series 2 and series 3, or acquired a dirt layer of some kind. However, of a more substantial impact might be the variation in substrate thickness. I have shown how a few tens of nanometres of difference in average thickness affect the measurement of the response time. But the substrate is not perfectly flat. Far from it. For a commercial-grade silicon wafer, we would expect up to 1 μm thickness variation over a distance of 2 cm [65], this means a skewness of several 100 nm over the ca. 3 mm focus spot. This might, together with any asymmetry in the spectrometer transfer function, lead to the observed differences, because the orientation and exact position of the reference substrate was not controlled between series.

5.3 Thickness scaling of conduction

The spectra already indicated that both response time and conductivity decrease with decreasing thickness, but they are not directly proportional to each other. Plotting

5.3 Thickness scaling of conduction

the conductivity and response time as a function of film thickness together in fig. 5.7 illustrates this very well. The conductivity stays constant for thick films, starts decreasing at 20 nm, jumps down between 10 and 8 and continues to decrease quickly. The response time, on the other hand, decreases from 100 nm onwards, also jumps down between 10 and 8 nm but then quickly levels off around 7 fs for the thinnest films.

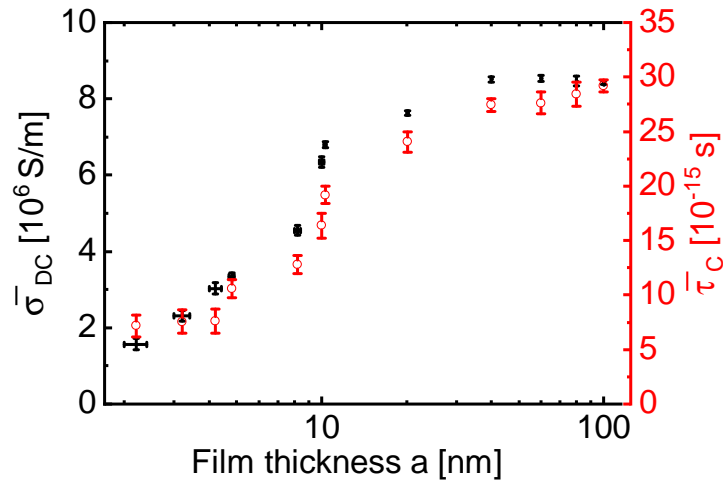


Figure 5.7: Thickness dependence of the DC conductivity and the current response time. The conductivity (black) is displayed on the left, the response time (red) on the right axis. The thickness coordinate of the response time data points is obviously the same as on the conductivity, hence the thickness uncertainty was only plotted for the conductivity. Both response time and conductivity decrease with decreasing thickness, but they are not directly proportional.

5.3.1 Comparison with previous works

I will compare the THz data with theoretical and experimental reports from the scientific literature. This helps to assess the quality of the iron film, highlight the improvement of the time resolution and show current debates impacted by this data specifically and the improved time resolution in general.

5.3.1.1 THz spectroscopy values for iron

For iron, only two SRT THz TDS measurements of the THz conductivity were published, by Hilton *et al.* [60] on a 12 nm film and by Bonetti *et al.* [9] on a 9 nm film. Hilton reports a very low conductivity of $2.5 \cdot 10^6 \text{ S/m}$ and an extremely high response time

5 Conduction dynamics in thin iron films

of 70 fs. Bonetti reports a conductivity of $6.4 \cdot 10^6$ S/m and a response time of 30 fs¹. Comparing this to $6.80 \pm 0.08 \cdot 10^6$ S/m and the 19 ± 1 fs for the 10.3 nm film, we see that Bonetti's film is similarly conductive, but its response time is ca. 10 fs higher. This is in line with the ca. 10 fs inaccuracy due to substrate thickness difference in the previous state of the art. Hilton's combination of low conductivity and extremely high time would imply ten times fewer free electrons (a ten times smaller integral of the band velocity over the Fermi surface in the Bloch picture eq. (2.28)), which also happen to scatter 3 times less often. This is physical unreasonable in the same material. Considering the relatively good agreement with Bonetti, and the fact that I have an entire series of consistent data points, I argue that Hilton's data, at least his response time, are inaccurate. Neither Bonetti nor Hilton have given explicit accuracy estimates, so I have assumed significant digit precision.

5.3.1.2 Thickness scaling of THz conductivity in metals

The only other measurement series of time-resolved THz conductivity as a function of metal thickness was done on gold deposited directly on silicon by Walther *et al.* [32]. The gold formed islands which only connected enough to form a percolation path above 8 nm, and the study stopped at 28 nm mean gold thickness. The conductivity of the gold increased with increasing thickness, while the response time stayed constant. Given that the gold was polycrystalline, grain boundary scattering was probably dominant, and if the grain size did not change much, neither would the intrinsic scattering times. The films were rough to the point that they had visible holes and even isolated islands. For such a rough film, my extension of Namba's model predicts an increase in the apparent conductivity and constant response time with increasing thickness to roughness ratio (see section 3.5). On one hand, this nicely explains the observation; on the other hand, the 10 fs limitation on the accuracy of Walther's ca. 20 fs response times might very well have obscured any thickness scaling of the response time.

5.3.1.3 Thickness scaling of iron DC-conductivity

While THz data is scarce, DC-conductivity data is more common, especially on iron. This is mostly due to interest of the spintronics community, specifically concerning giant magnetoresistance [46, 66] in the 1990's and recently concerning the anomalous Hall effect and the spin Hall angle [67, 68]. The resulting magnitude and scaling differ quite impressively between the different works.

Jacob *et al.* [46] measured the conductivity during the epitaxial growth on a room temperature substrate. The key point is that the film was neither annealed nor capped. Jacob's iron was not conducting below 3 nm, and the conductivity values are lower than all other measurements at similar thicknesses, with the exception of Hilton's [60].

¹Both works refer to the time constant as "(Drude) scattering time" rather than response time. Even though at least Bonetti *et al.* acknowledge that spin up and spin down relaxation time are different [9], they somewhat contradictorily still interpret conductivity in Drude's universal relaxation time picture.

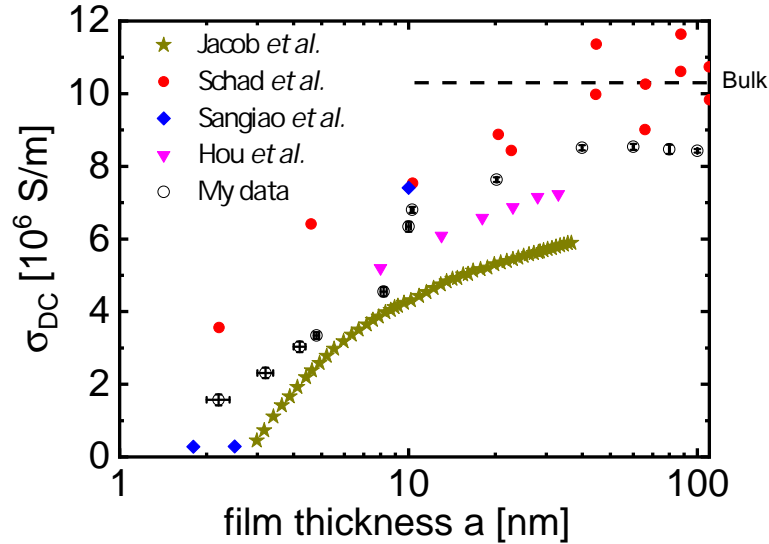


Figure 5.8: Thickness dependence of the DC conductivity of thin iron films on MgO measured for this work compared to literature values. My data is displayed as black circles. Jacob *et al.* [46] (gold stars) measured the conductivity of iron during epitaxial deposition on MgO. Schad *et al.* [66] (red disks) measured films grown on MgO, but capped with strontium fluoride (SrF_2). Sangiao *et al.* [67] (blue diamonds) and Hou *et al.* [68] (pink triangles) both use MgO capping, same as the samples in this thesis. The dashed line indicates the bulk value, taken from Hust’s report [3].

Jacob *et al.* extrapolate a bulk conductivity of $6.3 \pm 0.8 \cdot 10^6$ S/m, which is only 61% of value for optimally annealed bulk iron [3], though that may have been due to the extrapolation model used.

Schad *et al.* [66] epitaxially grew their iron from molecular beams on a 50° C warm MgO substrate and capped with SrF_2 . They do not mention any annealing. Their values are the highest across the board, even exceeding the literature bulk value for thicknesses above 50 nm. The latter point makes me a bit sceptical, since either Schad *et al.* have found a way to make thin iron films more conductive than bulk iron or they somehow systematically overestimate the conductivity. Schad *et al.* just state that their values are “close” to the literature bulk value and do not discuss this comparison in more detail. Further the values reported for similar thicknesses fluctuate by more than 10%. These fluctuations suggest somewhat limited statistical accuracy. Within the fluctuations, Schad’s values are constant above 50 nm film thickness, similar to my measurement.

Sangiao *et al.* [67] measured microscopic iron films sputter-deposited on 200° C hot MgO and capped with 3 nm of sputter deposited MgO. They report the room temperature

5 Conduction dynamics in thin iron films

conductivity only for three samples: a 10 nm film, which is slightly more conductive than the 10 and 10.3 nm films measured for this thesis; and a 1.8 and a 2.5 nm thick film, whose conductivities are extremely low. Sangio *et al.* did extensive characterisation on these thin films, including transmission electron micrographs, but could not find any defects or other anomalies explaining this extremely low conductivity. The fact that those extensively characterised films without apparent defects have a much lower conductivity than the thin films I measured speaks, I submit, to the quality of my samples. It also indicates that conductivity itself is probably the best macroscopic measure of film quality.

Hou *et al.* [68] studied iron epitaxially grown on MgO, but do not give any details concerning the growth method and recipe nor characterisation. Their thick films are slightly less conductive than my measurements, the 8 nm film is slightly more conductive than my 8.2 nm sample.

Thin iron films, due to their technological application in giant magnetoresistance stacks, are among the best-studied and controlled nanometric thin film systems. However, the various samples, nominally all bcc iron, are very different from another. This indicates the experimental control over the system is still somewhat lacking. This makes a quantitative comparison with a supposedly universal microscopic model somewhat useless. Still, Jacob *et al.* [46] and Schad *et al.* [66] extracted universal mean free path values based on different versions of Fuchs's model [43](section 3.3).² Jacob *et al.* give a lower limit on the bulk universal mean free path of 11 ± 1 nm while Schad *et al.* give 14 nm. The latter estimate contradicts the assumption implied Schad *et al.* [66], since they use the approximation of Fuchs's model for thicknesses much larger than the mean free path [43] and their result critically depends on the 2 nm film, 7 times thinner than their mean free path value. Those values do not match, but are surprisingly similar, considering that Jacob *et al.* extrapolate a bulk conductivity only half as large as Schad's. The universal mean free path assumption would require the mean free path to be directly proportional to the "bulk" value. These inconsistencies are unsurprising given the lack of control over the system and the lack of justification for using a universal mean free path to theoretically describe the thickness scaling of metals in general and iron in particular (sections 2.5.3 and 3.1.1).

The conductivity of the films presented here is comparably high, indicating good film quality. However, the comparison also emphasizes the jump between the 8.2 and 10 nm films, which most likely results from a sudden reduction in film or interface quality. Hence I do not attempt quantitatively model the detailed thickness scaling of conductivity in these iron films.

²Note that both works cite the giant magnetoresistance effect in iron chrome heterostructures [40] as motivation, which is based on the difference between the expected free paths of spin- \uparrow and spin- \downarrow electrons [20, 40, 41]. There is some inconsistency in assuming a universal mean free path for analysing measurements motivated by the variation between expected free paths.

5.3.1.4 Comparison to other spectroscopic data

One occasionally finds experimental values for Drude model parameters in metals. For example, Bonetti *et al.* refer to the 25 fs optical response time τ_o deduced by Ordal *et al.* [15] as “literature values for bulk Fe” and compares this data to their THz current response time. Such “literature” values are usually derived from optical to mid-infrared spectroscopy measurements [14, 15, 69]. Optical spectroscopy data on metals is usually not intrinsically phase resolved. Kramers-Kronig relations are applied to estimate real and imaginary parts based on amplitude data [14]. This procedure will be the less accurate, the smaller the analysed frequency range is. The resulting spectra can be fitted more or less well with Drude’s model eq. (2.3). Ordal *et al.* write that they could not fit a Drude model to their data for iron in their 1983 paper [14], but Ordal and a different group of co-workers do use the mid-infrared part of this data to estimate Drude parameters in 1988 [15]. I consider the fit for iron generally very poor, and therefore the values questionable. More importantly, I have shown in section 2.5.2 that observing a Drude model in the optical range ($\omega \gg \tau_C^{-1}$) does not by any means prove Drude’s hypothesis of a universal relaxation time, nor is the optical response time τ_o directly comparable to the current response time τ_C in the THz regime ($\omega \ll \tau_C^{-1}$). Last but not least, Ordal *et al.* also tried to include resonant cavity measurements in the THz/far-infrared regime in the data they estimated their Drude parameters from [15]. These low-frequency measurements should be more relevant for comparison since they are close to our frequency range. However, Ordal *et al.* use the assumption that the real n and imaginary κ part of the refractive index \tilde{n} are equal to recover the material properties from the cavity measurements. As shown in fig. 1.3, this negates the key influence of the dynamics on the complex refractive index and prohibits any meaningful estimate of the response time. Generalising for all metals, some infrared spectroscopy values for optical response times may exist, but Kramers-Kronig and other analyses schemes result in questionable accuracy and the meaning of these high-frequency measurements for direct current conductivity is qualitative at best.

5.3.1.5 THz conductivity deduced from surface plasmon polariton propagation

THz transmission measurements of metals tend to agree well with direct current data in terms of the magnitude of the conductivity [70–72]. However, metal waveguides perform much worse than they should for flat structures of such highly conductive materials (see the review by Pandey *et al.* [72] and references therein). Vice versa, the conductivities estimated from the surface plasmon polariton (SPP) propagation in wave guides or plain metal sheets are much lower than the DC-conductivities of those components. This leads Pandey *et al.* [72] to conclude that there is “non-Drude like behaviour of metals in the THz spectral range” (the title of their review). Gerasimov *et al.* [73] explain their observed discrepancies by stating that surface properties of metals are different than in bulk. The data on the iron films measured here show that the THz properties between “bulk” and very thin, basically surface-only films, are in no way different enough to explain the discrepancy between the SPP conductivity values

5 Conduction dynamics in thin iron films

and direct current data.

Pandey *et al.* do not claim a definite cause of the discrepancy, but they do rule out the effect of a surface roughness h of ca. $3 \mu\text{m}$ (standard deviation of the height); which was found in a work of Pandey and a different group of co-workers [74]. Pandey *et al.* reason that the $3 \mu\text{m}$ roughness are much smaller than the free space wavelength λ_0 ; at their example frequency of 0.5 THz $h \approx 0.005\lambda_0$. They make the case that optical grade metal coatings for mirrors only need to be flat within $h < 0.05\lambda_0$.

I argue that the relevant wavelength is not the one in air, but the one inside the material; therefore we should look at $\frac{\lambda_0}{n}$. As Pandey *et al.* remind in their review [72], the real refractive indices n of metals at optical frequencies are very low³. Let us use the same example as Pandey, gold at 800 nm wavelength. This frequency, gold has $\tilde{n} = n + i\kappa = 0.16 + 5.08i$ [69]. Therefore the relevant flatness of a $h < 0.05\lambda_0$ metal coating is even better with $h < 0.008\lambda_0/n$ for 800 nm light.

In the THz range, metal refractive indices are on the order of several hundred (see fig. 1.4); at 0.5 THz, gold of a bulk conductivity of $44 \cdot 10^6 \text{S/m}$ and ca. 20 fs response time [32] should have $\tilde{n} = 860 + 916i$. At 0.5 THz, $h = 3 \mu\text{m}$ roughness lead to $h = 4.3 \frac{\lambda_0}{n}$; that means the roughness is more than 4 times higher than the effective wavelength at THz frequencies. This is very rough; roughnesses on a similar relative scale severely impact optical SPP dispersion. The measurements presented here and in the work on gold meshes [71] show that the THz metal conductivities are on the same order as the direct current conductivities. I therefore argue that roughness, and not material properties, is the cause of the slow and lossy propagation of THz SPPs and may be the factor currently limiting the distance THz signals be transmitted by wire to a few meters compared to the several hundred meters theoretically possible.

5.4 Thickness scaling of the variation of relaxation times

Despite Mott [5] and Fert [20, 40, 41] widely spreading the concept that a significant variation between microscopic relaxation times exists at least in magnetic metals, many works ignore this fact partially or completely. An example is the work of Hou *et al.* [68], who calculate scattering and spin deflection for surface and bulk scattering in iron films in quite some detail, just to sum scattering and resistivities up with Mathiessen's rule. Mathiessen's rule only applies when there is no variation between microscopic relaxation times and the scattering mechanisms are uncorrelated (see section 2.7.2, [13, 27]). Neither of the two conditions apply for surface scattering in iron (see section 3.4.1 and fig. 3.3). Empirically, already Mathiessen and Vogt [39] found iron to deviate from the scaling relation they observed in most metals.⁴

³Potentially, the modulus of the index $|\tilde{n}|$ should be used instead of the real part. This will however not alter the key result, namely that for THz waves, $\lambda_0/200$ roughness of a metal surface is rough, while in the optical regime a metal coating with $\lambda_0/20$ can be considered flat

⁴The key empirical observation in Hou's paper [68] is a minimum of the anomalous Hall effect in temperature and thickness scaling. Hou interprets this in terms of different spin-orbit coupling for surface and bulk scattering. However, surface scattering may alter the spin polarisation of the current in a film by preferentially scattering the spin with the longer expected free path. This can,

5.4 Thickness scaling of the variation of relaxation times

So, despite all theoretical insight and experimental evidence, the variation of microscopic relaxation times is often ignored. In the THz region, interpreting conductivity under Drude's assumption of a single, universal relaxation time is still very common [9, 32, 60], spurred by the observation that the spectral shape matches Drude's model. I have shown that we would also expect an effective Drude type dispersion at THz frequencies when the microscopic relaxation times vary (see section 2.5, eq. (2.36)). Still, looking at the observed spectral shape individually, Occam's razor would dictate interpreting them according to Drude's simpler universal relaxation time assumption. However, there is a way to determine the validity of the universal relaxation time assumption, since it also dictates that response time and conductivity are proportional.

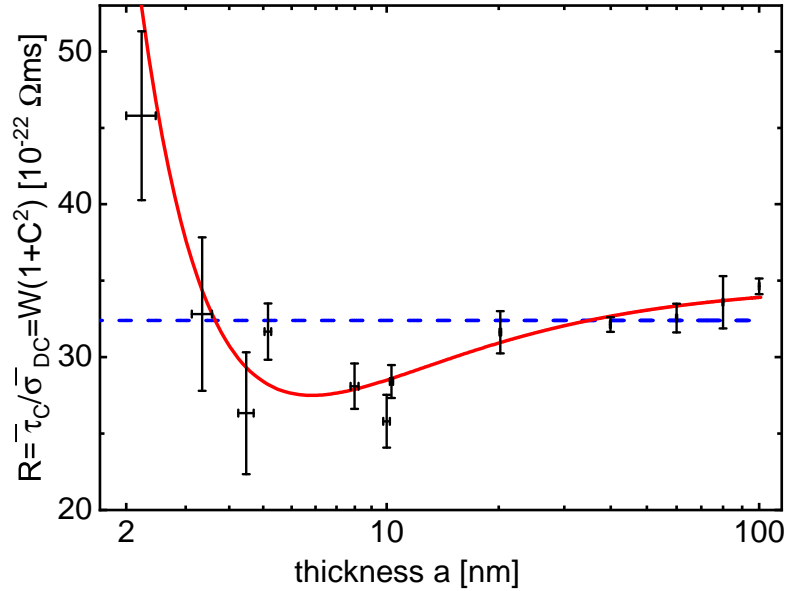


Figure 5.9: Ratio R between current response time $\bar{\tau}_C$ and DC-conductivity $\bar{\sigma}_{DC}$ estimates as a function of the film thickness. The blue dashed is the constant fitted to the data, as predicted by the hypothesis of a universal relaxation time. The probability of obtaining data fitting worse to universal relaxation time hypothesis is 0.000 000 001, lower than the probability to lie outside a 6 Gaussian standard deviation confidence interval. The red curve is a second-order polynomial fit in $1/a$, consistent with two competing processes altering the variation C of the relaxation times. The probability of obtaining data fitting worse to the red curve is 0.21.

The accuracy of the measurements of the response times is not only high enough to show that decreasing conductivities correlate with decreasing response times, but it also

at least qualitatively, explain Hou's observation as well.

5 Conduction dynamics in thin iron films

shows that response time and conductivity are not directly proportional. Therefore, I plot the thickness scaling of the ratio R of response time per conductivity in fig. 5.9. The ratio starts out high, decreases down to 10 nm and increases again. I analyse how significant these deviations from direct proportionality are. The best fit for a constant ratio lies several times the estimated errors above the intermediate films around 10 nm, and several times below that for 100 nm. Under the assumption that the data is normally distributed, the error bar gives my estimate of the 68 % confidence interval. Within this assumption, the probability of obtaining data fitting worse to the hypothesis of a universal relaxation time is 10^{-9} , equivalent to 6 standard deviations for a normal distribution. The deviations are significant.

The ratio of response times to conductivity $R = \frac{\bar{\tau}_C}{\bar{\sigma}_{DC}}$ is equal to $W \cdot (1 + C^2)$. I will, therefore, interpret the scaling of the ratio R as scaling of the variation C of microscopic relaxation times. The first observation is that above 10 nm, the thicker the film, the larger R and therefore the variation C . Therefore the variation of relaxation times in bulk must be large. I have identified 2 mechanisms by which surface scattering may change the variation of relaxation times: Anticorrelation with bulk scattering (section 3.4.1) and addition of positional and further directional variation between scattering times (section 3.4.2). The anticorrelation between scattering mechanisms decreases the variation of relaxation times. This may explain the observed decrease of R from bulk towards 10 nm. Surface scattering will add variation between electronic relaxation times with regards to the electron's position and speed towards the surface. This increase in variation will outcompete the anticorrelation with bulk scattering when surface scattering replaces bulk scattering as the dominant scattering process. At the point where both scattering processes are equally prevalent, the conductivity should have dropped roughly by half compared to the bulk value; which is the 8 nm sample in this study. Therefore, the additional positional and directional variation of microscopic relaxation times may explain the tentative increase in R for films thinner than 8 nm. For these thin films, though, any interpretation of the results are tentative only for several reasons: Firstly, because the statistical accuracy is much smaller than for the thick films; secondly because other effects like Namba's roughness size effect [45] (section 3.5) should result in similar trends. For extremely thin films, even the electronic structure (and thereby the value of W) might change [75].

The simplest mathematical formula satisfying the above qualitative argumentation for the scaling of the ratio R is

$$R(a) = R_\infty - \frac{b_1}{a} + \frac{b_2}{a^2}. \quad (5.2)$$

R_∞ is the bulk limit of R , the b_1 term describes the decrease of variation by anti-correlated scattering and the b_2 term the additional variation due to positional and directional dependence of the surface scattering probability. This polynomial fits the observed data decently well (red line in fig. 5.9); the probability to observe worse fitting data is 0.21.⁵ The coefficients for which this polynomial fits the data are

⁵The expectation value of this probability is 0.5.

5.4 Thickness scaling of the variation of relaxation times

$R_\infty = 34.8 \cdot 10^{-22} \text{ } \Omega\text{ms}$, $b_1 = 9.2 \cdot 10^{-15} \text{ } \Omega\text{s}$ and $b_2 = 2.9 \cdot 10^{-6} \text{ } \Omega\text{s/m}$. Values are given to significant digit precision. The main function of these parameters is to simplify empirical comparison of the $R(a)$ data to any future results; the main point shown by this polynomial describing the data is that the deviations from the universal relaxation time hypotheses are systematic and qualitatively this systematic scaling can be understood in terms of a scaling of the variation times. The hypotheses of the anticorrelation of bulk and surface scattering competing with the increase in directional variation by surface scattering also qualitatively explains the coincidence the minimum of the $R(a)$ curve with the thickness where the measured conductivity reduces to half the thick film limit. The reasoning is as follows: Anticorrelation with bulk scattering will only have an effect when bulk scattering is still significant. The minimal variation will happen where further decreases of the bulk variation will exactly match increases of the variation of surface scattered electrons. This will most likely happen when both scattering processes are similarly likely, and this in turn will be roughly where the resistivity due to surface plus bulk scattering is twice that from bulk scattering alone.

5.4.1 Comparison with band structure calculations

At last, we can compare the estimated bulk value of R to values of W calculated from band structure. I remind that $R = W \cdot (1 + C^2)$. Therefore we can hope to quantify the variation C . The quantity W is the same as the product of an assumed universal relaxation time τ_u and the bulk resistivity ρ_∞ ; $W = \tau_u \cdot \rho_\infty$. This is the way Gall [30] denotes it. Gall calculated the value for the 20 most conductive elemental metals. Iron is only the 22nd most conductive, so it is not included on Gall's list. Nevertheless, I can remark that the measured value of R_∞ of $34.8 \cdot 10^{-22} \text{ } \Omega\text{ms}$ is larger than the $\tau_u \cdot \rho_\infty$ of all of the 20 metals Gall calculates. Looking at nickel, a ferromagnet with a cubic lattice like iron, Gall obtains a value of $\tau_u \cdot \rho_\infty = 10.0 \cdot 10^{-22} \text{ } \Omega\text{ms}$, 3.5 times smaller than our observed value for R_∞ . Cazzaniga *et al.* [76] calculated a Drude plasma frequency ω_p from his calculated band structure. Via $W^{-1} = \epsilon_0 \omega_p^2$ from which one can deduce a value for W of $9.76 \cdot 10^{-22} \text{ } \Omega\text{ms}$; very close to Gall's value for nickel. We can therefore observe that R_∞ is about 3.5 times larger than what band structure calculations predict for W . From this we can estimate the variation $C = 1.6$, an extremely large variation (see an example of a distribution with $C = 0.6$ variation in fig. 2.9 for comparison). This implies that the average relaxation time $\langle \tau \rangle$ is 3.5 times smaller than the observed current response time τ_C values; the 29 fs response time of the 100 nm film translate to a mean relaxation time of only 8 fs.

5.4.2 Comparison with Drude's model

Quite surprisingly, Drude's outdated formula eq. (2.3) is still frequently used to estimate W as $(e^2 n / m)^{-1}$ and thereby (universal) relaxation times from empirical conductivities, mostly in conjunction with values for the electron density n taken from table 1, page 5 of Ashcroft and Mermin's book [27] and the free electron mass m [76, 77]. Chatterjee and Meyerovitch [77] even state "A good estimate for τ_{tr}^b and τ_b can be obtained from

5 Conduction dynamics in thin iron films

the experimental data on bulk resistivity ρ , $1/\tau_{tr}^b = ne^2\rho/m$., where τ_{tr}^b appears to correspond to the average relaxation time $\langle\tau\rangle$ in this thesis. The value of n is even within Drude’s original theory often not exactly determined, as Ashcroft and Mermin state that they “have arbitrarily selected one value of [the number of electrons per atom contributing to conduction] Z for those elements that display more than one chemical valence” [27], such as iron, which may have oxidation state 2 or 3. Using Ashcroft and Mermin’s choice of 2 for iron, $(e^2n/m)^{-1} = 2.1 \cdot 10^{-22} \text{ } \Omega\text{ms}$, five times lower than the band structure estimate, leading to an estimate on the average bulk response time $\langle\tau\rangle$ of 2 fs, compared to 10 fs from Cazzaniga *et. al.*’s band structure estimate and a 14 times lower than observed current response time of 29 ± 1 fs at 100 film thickness. I point out that at least for metals with more than one band at the Fermi surface, Drude’s original model may only be used for rough estimates with a inaccuracies of one or two orders of magnitude.

5.5 Summary

I have time-resolved the dynamics of conduction in iron films with enough precision to demonstrate decreasing current response times with decreasing thickness. The resolution was sufficiently high to resolve significant deviations between the scaling of the DC-conductivity and the response time. This happens when a variety of microscopic relaxation times exists and the variation of these relaxation times changes. At this point, we need to distinguish between the observable macroscopic response time τ_C , the various microscopic relaxation times τ , and the mean relaxation time $\langle\tau\rangle$ parametrising DC-conductivity σ_{DC} . The conductivity spectrum can be fully described by the distribution $w(\tau)$ of microscopic relaxation times. For the low-frequency limit, the observable DC-conductivity depends on the mean $\langle\tau\rangle$, the response time on mean $\langle\tau\rangle$ and variation C of the distribution of relaxation times. Surface scattering changes the shape of the distribution of relaxation times, which in turn explains the thickness scaling of the ratio $R = \tau_C/\sigma_{DC}$.

6 Impact of time-resolving conduction in a metal

In this concluding chapter, I will take a step back and discuss the general implications that the ability of time-resolving conduction in metals demonstrated in this thesis has for the understanding and investigation of the conduction process and the time domain spectroscopy method. The key advantage that time-resolving conduction brings is adding a second macroscopic observable of the conduction process on top of the conductivity: the current response time.

Measuring the current response time in a metal with THz time domain spectroscopy was thought to be impossible by the THz scientists Dressel and Scheffler [78]¹ back in 2006. The underlying misconception was that one needs frequencies of the same size as the rate constant investigated to resolve the respective rate. This argument holds for resolving resonance frequencies (which are connected to transitions between states of different energies), but not for damping rates (which are connected to dephasing rather than energetic transitions). This misconception is likely even more common outside the THz community. This thesis will spread the understanding of the power of time domain spectroscopy to measure dephasing processes in general and current response times in metals in particular.

While this is not the first measurement of current response times in a metal, the increase in precision achieved here means that now the current response time becomes a valuable second observable of the conduction process. Adding this second macroscopic observable will advance the understanding of the conduction process. The thickness scaling of conduction is one area that may particularly benefit. As the dimensions of transistors shrink to 10 nm [80, 81] or even lower, so must the dimensions of the metal wires connecting them. The decreasing conductivity with decreasing dimensions exacerbates the problem that the resistance of a wire increases when one scales it down in all three dimensions, contrary to the switching loss of a transistor. This problem quickly approaches the point where the metal interconnects, and not the semiconductor transistors, dominate the heat generated in logical circuits and thereby limit the maximum transistor density and ultimately the computational power. Understanding the thickness scaling of electrical conduction in metals has thus become industrially relevant. Experimentally, controlling thin metal films in terms of crystal growth and quality is difficult, adding a lot of variables influencing a single measured quantity: the conductivity. Measuring the current response time helps to improve the balance between the number of experimental variables to be controlled and the number of

¹And Dressel's and Scheffler's misconception is still spread on wikipedia [79].

6 Impact of time-resolving conduction in a metal

quantities measured. The correlation between the conductivity and the response time may serve as a crude consistency check, which may allow uncovering a severely flawed estimation of the film thickness. This may prove especially helpful when studying complex structures like patterned films [71], where the correct thickness average is hard to estimate. More importantly, I have shown that the current response time contains additional information about the distribution of microscopic relaxation times, and thereby delivers additional information on the increased momentum relaxation in thin films compared to the conductivity. This additional information can advance the understanding of the thickness scaling of transport processes.

The theoretical description of the current response time also necessitates a fundamental improvement of the models currently used to describe the thickness scaling of conduction. Current theoretical descriptions of the scaling make both unrealistic assumptions, such as universal mean free paths and relaxation times, and depend on a lot of additional parameters to describe the direct current conductivity as the single resulting observable. The precise measurement of the current response time necessitates new or expanded models that can predict the dynamics of conduction. The detailed relation between response time and conductivity might depend on fewer parameters than either observable. This may allow testing predictions of conduction models even if the experimental control over some of the parameters is limited. Even further, I have shown that one has to abandon the universal mean free path and universal relaxation time assumptions to accurately derive the current response time. One has to take into account a distribution of microscopic relaxation times to describe the full dynamics of conduction; for the current response time in the low-frequency limit, the average and the variation of this distribution suffice. This demands an even greater revision of the current conductivity models.

The above discussion holds for the general theoretical description of conduction, not just in thin films. The reader may have noticed that I did not compare the observed current response times to estimates based on theoretical calculations. Such estimates are not published; neither for the current response time nor for a universal or average relaxation time. An important reason may be the lack of awareness that the time/rate constants used in the theoretical description of conduction are actual (microscopic) observables and connect to macroscopic observables like the current response time which can be measured in addition to the conductivity. As an example, Chatterjee and Meyerovich [77] derive effective transport times $\tau_{tr}^{(eff)}(\vec{p})$ as function of momentum \vec{p} from microscopic transition rates to infer the thickness scaling of the conductivity, but do not give any explicit estimates on the times, their scaling or their distribution. On a similar note, of the five works [76, 82–85] recently publishing the electronic band structure of iron, only Cazzaniga *et al.* [76] did the small extra step to publish the integral of the band velocity over the Fermi surface, which I denote as W . W is useful to compare with conductivity measurements [30] and allows estimating the variation of microscopic relaxation times from the ratio of the effective Drude parameters, as done in this thesis. Showing that these theoretical quantities are more directly linked to actual observables hopefully leads to more of them getting published, paving the

route to a quantitative description of conduction dynamics in metals. I have shown that while the THz conductivity of iron is well described by an effective Drude spectrum, the relationship between the parameters of this spectrum does not match Drude's hypothesis of a universal relaxation time. In other spectral regions, such inconsistencies of Drude's model had already been observed. Ordal *et al.* [14] found the infrared spectra of tungsten to fit Drude's spectral shape well, but obtained three different Drude relaxation rates for three different ways of extracting this rate from Tungsten spectra and DC-conductivity. Faced with the fact that Drude's curve fits the spectra, but its parameters are inconsistent with Drude's underlying model, Ordal *et al.* did "disclaim any physical significance for the Drude model. The intent is only to parameterize the optical constants for these metals even when there is some question as to the physical meaning of the parameters". With the relaxation time distribution picture that I have introduced in this thesis, the parametrisation of the THz spectra is again linked to the microscopic relaxation times and the electronic structure. Therefore measuring the parameters allows inferring information about the microscopic relaxation times. Providing this link may be critical in advancing the understanding of conduction, as even though Drude's assumption of a universal relaxation time has been deprived of its theoretical basis and empirically proven wrong multiple times, the concept of a universal relaxation time and derivatives such as Mathiessen's "rule" are still used abundantly. This leads to very questionable inferences from experimental data and equally questionable assumptions in theoretical calculations. The crux is "that misinformation can still influence inferences one generates after a correction has occurred", as Johnson and Seifert [86] state; "however, providing an alternative that replaces the causal structure it affords can reduce the effects of misinformation". I hope that by enabling measurements precise enough to necessitate going beyond Drude's universal relaxation time hypotheses and developing the relaxation time distribution picture to describe them, this thesis contributes to replacing the universal relaxation time assumption with the relaxation time distribution picture.

7 Appendix

7.1 Different relaxation times approximation

This is a less formal and slightly different way of deriving the relaxation times approximation. It is based on expanding the collision integral for a small perturbation g_1 . Under the assumption of spatial homogeneity already used to justify the transition from plasma to gas, the collision integral must vanish in equilibrium; $I_C(\vec{p}, g_0) = 0$. Now, since the variation of the distribution $g_1(\vec{p}')$ at all points \vec{p}' is caused by the same external field \vec{E} as $g_1(\vec{p})$ at point \vec{p} , these variations should be correlated. Since \vec{E} enters linearly into the equation of motion eq. (2.8), we can expect the response to be linear. Therefore, a linear expansion taking into account the all correlations within the collision integral will be an adequate description of I_C for small variations g_1 .

$$I_C(\vec{p}, g_0 + g_1) = I_C(\vec{p}, g_0 + g_1)|_{g_1=0} + \left. \frac{dI_C}{dg} \right|_{\vec{p}, g_1=0} g_1(\vec{p}) + O((g_1)^2) = -\frac{g_1(\vec{p})}{\tau(\vec{p})} \quad (7.1)$$

Here $\left. \frac{dI_C}{dg} \right|_{\vec{p}, g_1=0}$ is the derivative of the collision integral.

7.2 Geometry of the iron film samples

The samples presented this thesis are thin iron films epitaxially grown on a MgO substrate capped with a thin MgO layer. This sequence of layers is sketched in fig. 7.1. The thickness of the MgO layer is $b \approx 12$ nm for all samples. The iron layer is between $a = 2.2$ nm to $a = 100$ nm thick. The substrates of the samples are $l_s = 500$ μm thick. The substrate thicknesses l_s vary by up to 30 μm between samples.

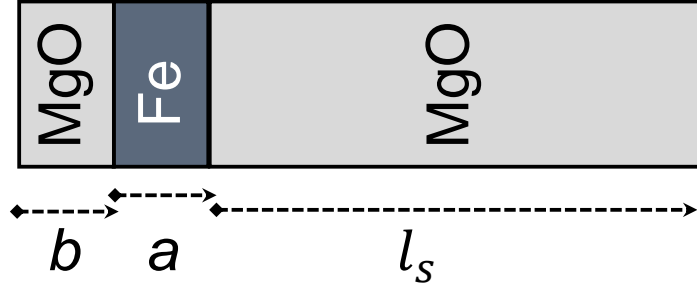


Figure 7.1: Sketch of an iron film on a magnesium oxide substrate. All films measured in this thesis are capped by $b \approx 12$ nm of MgO to prevent oxidation. The iron layers range from $a = 2.2$ nm to $a = 100$ nm thickness. The substrates are nominally $l_s = 500$ μm thick. I refer to the whole stacks in the following as “samples”.

7.3 Substrate index

The refractive index of the substrate \tilde{n}_3 is necessary to obtain the thickness difference and to retrieve the complex conductivity. The substrate index is measured by comparing the field pulse transmitted through a bare substrate to a field pulse transmitted through dry nitrogen, see fig. 7.2. To exactly determine the substrate thickness, the first echo in the substrate is also recorded. The resulting time traces are recorded in three time windows: The direct transmission in the substrate $E_{S,I}$, the echo $E_{S,II}$ and the transmission through dry nitrogen E_N . For the numerical treatment, the time windows are chosen to be the same lengths and to have their respective pulses at roughly the same position relative to the window starting times. These starting times are referred to as $T_{S,I}$, $T_{S,II}$ and T_N . Having the pulses at similar positions within the windows will avoid errors in the numerical unwrapping of the phase when the phase jump per frequency step exceeds 2π .

For an incident pulse E_0 the spectral densities of the three pulses read:

$$\tilde{E}_{S,I} = \tilde{E}_0 t_{0,3} p_3(l_s) t_{3,0} \quad (7.2)$$

$$\tilde{E}_{S,II} = \tilde{E}_0 r_{0,3}^2 p_3(2l_s) \quad (7.3)$$

$$\tilde{E}_N = \tilde{E}_0 p_0(l_s) \quad (7.4)$$

Here l_s is the thickness of the substrate material. Remembering that $p_i(x) = e^{i\omega/c0\tilde{n}_i x}$ and using the fact that the index of the transparent substrate is predominantly real,

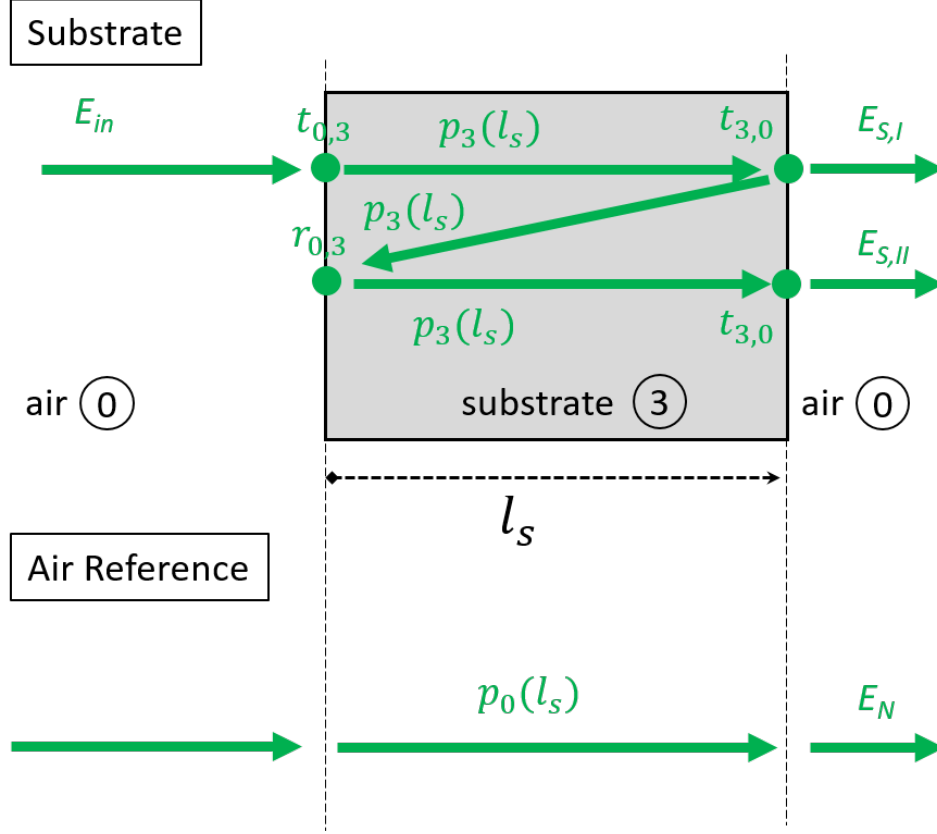


Figure 7.2: Beam paths for the direct transmission and the first echo through a bare substrate and the beam path through dry nitrogen (air). The substrate material is denoted with 3 and the nitrogen with 0.

we can write down the following relations for the lags $T = \phi/\omega$ between the pulses¹:

$$T_{0,1}(\omega) = \phi \left(\frac{\tilde{E}_{S,I}}{\tilde{E}_N} \right) / \omega = (\tilde{n}_3 - \tilde{n}_0) l_s / c_0 \quad (7.5)$$

$$T_{1,2}(\omega) = \phi \left(\frac{\tilde{E}_{S,II}}{\tilde{E}_{S,I}} \right) / \omega = 2\tilde{n}_3 l_s / c_0 \quad (7.6)$$

$T_{0,1}$ is the lag between the pulse through air and the direct transmission through the sample; $T_{1,2}$ is the lag between direct transmission and first echo. $\phi(\tilde{x})$ denotes the phase of the complex number \tilde{x} ; c_0 is the speed of light in vacuum. The substrate thickness can then be extracted from each frequency component of the THz measurement using $\tilde{n}_0 = 1$ as:

$$l_s(\omega) = c_0 (T_{1,2}(\omega) - 2T_{0,1}(\omega)) / 2 \quad (7.7)$$

¹For the practical numeric data treatment, I use 3 windows with different start times. The differences in respective start times between two pulses add to the lag between them.

7 Appendix

Since the thickness needs to be constant, a spectral average \bar{l}_s is taken to obtain a single constant.

With this, the real part n_3 of the refractive index of the substrate is:

$$n_3(\omega) = c_0 T_{0,1}(\omega) / \bar{l}_s + 1 \quad (7.8)$$

Within the assumption that the absorption is small, the imaginary part κ_3 can

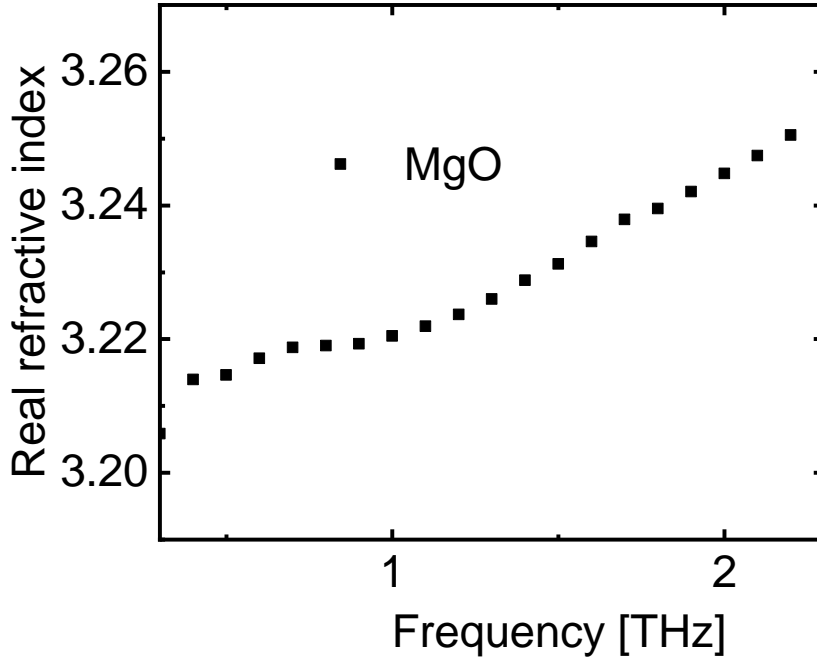


Figure 7.3: The average values of real refractive index of MgO as measured. Statistical errors not shown, since systematic errors from uncertainties of the substrate thickness and Gouy shift will dominate them. 1% systematic error assumed when propagating the error in refractive index onto DC-conductivity and current response time estimates.

be retrieved by using the amplitude and approximating the \tilde{n}_3 as n_3 in the Fresnel coefficients:

$$\kappa_3(\omega) = -\log \left(\left| \frac{\tilde{E}_{S,I}}{\tilde{E}_{N2}} \right| \frac{1}{t_{0,3} t_{3,0}} \right) \frac{c_0}{l_s \omega} \quad (7.9)$$

For MgO, the measured κ_3 turns out to be very close to 0 and mostly slightly negative; the latter part is non-physical. Therefore κ_3 is set as 0. Figure 7.3 show the measured real part of the refractive index.

7.4 Measurement series

Table 7.1 lists the samples measured in each series.

series	month	reps	samples
1	08.2016	30	“2 nm”, “5 nm”, “8 nm”, “10.3 nm”, “20 nm”, “100 nm”
2	08.2017	10	“3 nm”, “4 nm”, “10.3 nm”, “40 nm”, “60 nm”, “80 nm”
3	06.2018	10	“3 nm”, “4 nm”, “10.0 nm”, “20 nm”, “40 nm”, “60 nm”, “80 nm”, “100 nm”

Table 7.1: Table of measurement series. The table lists the month of the measurements, the number of repetitions of sample/reference alternations in that round and the names of the samples, designated by their rounded thickness.

Bibliography

- [1] E. W. Weisstein, "Fourier Transform." <http://mathworld.wolfram.com/FourierTransform.html>.
Accessed: 2019-05-21.
- [2] R. A. Serway, *Principles of Physics*.
Fort Worth, Texas: Saunders College Pub., 2nd ed., 1998.
- [3] J. G. Hust and A. B. Lankford, "Standard Reference Materials: Update of thermal conductivity and electrical resistivity of electrolytic iron, tungsten and stainless steel," Tech. Rep. 90, National Bureau of Standards, U. S. Department of Commerce, Boulder, Co 80303, 1984.
- [4] P. D. Desai, H. M. James, and C. Y. Ho, "Electrical Resistivity of Aluminum and Manganese," *Journal of Physical and Chemical Reference Data*, vol. 13, no. 4, pp. 1131–1172, 1984.
- [5] N. F. Mott, "The electrical conductivity of transition metals," *Proceedings of the Royal Society of London. Series A - Mathematical and Physical Sciences*, vol. 153, no. 880, pp. 699–717, 1936.
- [6] E. Sondheimer, "The mean free path of electrons in metals," *Advances in Physics*, vol. 1, no. 1, pp. 1–42, 1952.
- [7] A. A. Abrikosov, *Fundamentals of the theory of metals*.
Amsterdam: North-Holland, 1988 editi ed., 1988.
- [8] C. Kittel, "Theory of the Dispersion of Magnetic Permeability in Ferromagnetic Materials at Microwave Frequencies," *Physical Review*, vol. 70, no. 5-6, pp. 281–290, 1946.
- [9] S. Bonetti, M. Hoffmann, M.-J. Sher, Z. Chen, S.-H. Yang, M. Samant, S. Parkin, and H. Dürr, "THz-Driven Ultrafast Spin-Lattice Scattering in Amorphous Metallic Ferromagnets," *Physical Review Letters*, vol. 117, no. 8, p. 087205, 2016.
- [10] J. J. Thomson, "XL. Cathode Rays," *The London, Edinburgh, and Dublin Philosophical Magazine and Journal of Science*, vol. 44, no. 269, pp. 293–316, 1897.
- [11] P. Drude, "Zur Elektronentheorie der Metalle," *Annalen der Physik*, vol. 306, no. 3, pp. 566–613, 1900.
- [12] P. Drude, "Zur Elektronentheorie der Metalle; II. Teil. Galvanomagnetische und thermomagnetische Effecte," *Annalen der Physik*, vol. 308, no. 11, pp. 369–402, 1900.

Bibliography

- [13] A. Sommerfeld, “Zur Elektronentheorie der Metalle auf Grund der Fermischen Statistik,” *Zeitschrift fuer Physik*, vol. 47, no. 1-2, pp. 1–32, 1928.
- [14] M. A. Ordal, L. L. Long, R. J. Bell, S. E. Bell, R. R. Bell, R. W. Alexander, and C. A. Ward, “Optical properties of the metals Al, Co, Cu, Au, Fe, Pb, Ni, Pd, Pt, Ag, Ti, and W in the infrared and far infrared,” *Applied Optics*, vol. 22, no. 7, p. 1099, 1983.
- [15] M. A. Ordal, R. J. Bell, R. W. Alexander, L. A. Newquist, and M. R. Query, “Optical properties of Al, Fe, Ti, Ta, W, and Mo at submillimeter wavelengths,” *Applied Optics*, vol. 27, p. 1203, mar 1988.
- [16] J. Lloyd-Hughes and T. I. Jeon, “A review of the terahertz conductivity of bulk and nano-materials,” *Journal of Infrared, Millimeter, and Terahertz Waves*, vol. 33, no. 9, pp. 871–925, 2012.
- [17] I. Ivanov, M. Bonn, Z. Mics, and D. Turchinovich, “Perspective on terahertz spectroscopy of graphene,” *EPL (Europhysics Letters)*, vol. 111, no. 6, p. 67001, 2015.
- [18] D. H. Lowndes, K. Miller, and M. Springford, “Anisotropy of the electron-impurity scattering in some dilute gold alloys,” *Physical Review Letters*, vol. 25, no. 16, pp. 1111–1115, 1970.
- [19] M. Springford, “Electron lifetimes in metals,” *Physics of Condensed Matter*, vol. 19, no. 1-4, pp. 1–15, 1975.
- [20] A. Fert and I. A. Campbell, “Two-Current Conduction in Nickel,” *Physical Review Letters*, vol. 21, no. 16, pp. 1190–1192, 1968.
- [21] J. Bass, “Deviations from Matthiessen’s Rule,” *Advances in Physics*, vol. 21, no. 91, pp. 431–604, 1972.
- [22] V. Gasparov and R. Huguenin, “Electron-phonon, electron-electron and electron-surface scattering in metals from ballistic effects,” *Advances in Physics*, vol. 42, no. 4, pp. 393–521, 1993.
- [23] A. B. Pippard, “Experimental analysis of the electronic structure of metals,” *Reports on Progress in Physics*, vol. 23, no. 1, p. 304, 1960.
- [24] L. D. Landau, “The Theory of a Fermi Liquid,” *SOVIET PHYSICS JETP*, vol. 3, no. 6, pp. 920–925, 1957.
- [25] T.-S. Choy, J. Naset, J. Chen, S. Hershfield, and C. Stanton, “A database of fermi surface in virtual reality modeling language (vrml),” in *Bulletin of The American Physical Society, MAR00 Meeting of the APS*, (Minneapolis), p. L36.042, American Physical Society, 2000.
- [26] T.-S. Choy, J. Naset, J. Chen, S. Hershfield, and C. Stanton, “The Fermi Surface Database.” <http://www.phys.ufl.edu/fermisurface/>, 2000.
Accessed: 2019-11-18.

- [27] N. W. Ashcroft and N. D. Mermin, *Solid State Physics*. Philadelphia: Saunders College Pub., 1976.
- [28] A. Einstein, “Über die von der molekularkinetischen Theorie der Wärme geforderte Bewegung von in ruhenden Flüssigkeiten suspendierten Teilchen,” *Annalen der Physik*, vol. 322, no. 8, pp. 549–560, 1905.
- [29] R. S. Sorbello, “On the anisotropic relaxation time,” *Journal of Physics F: Metal Physics*, vol. 4, no. 4, pp. 503–512, 1974.
- [30] D. Gall, “Electron mean free path in elemental metals,” *Journal of Applied Physics*, vol. 119, no. 8, p. 085101, 2016.
- [31] C.-K. Sun, F. Vallée, L. H. Acioli, E. P. Ippen, and J. G. Fujimoto, “Femtosecond-tunable measurement of electron thermalization in gold,” *Physical Review B*, vol. 50, no. 20, pp. 15337–15348, 1994.
- [32] M. Walther, D. G. Cooke, C. Sherstan, M. Hajar, M. R. Freeman, and F. A. Hegmann, “Terahertz conductivity of thin gold films at the metal-insulator percolation transition,” *Physical Review B*, vol. 76, no. 12, p. 125408, 2007.
- [33] S. Kamal, D. M. Kim, C. B. Eom, and J. S. Dodge, “Terahertz-frequency carrier dynamics and spectral weight redistribution in the nearly magnetic metal CaRuO₃,” *Physical Review B*, vol. 74, no. 16, p. 165115, 2006.
- [34] M. Shalaby, *Magneto-photonics phenomena at terahertz frequencies*. PhD thesis, Université du Québec, 2013.
- [35] W. J. de Haas and P. M. van Alphen, “The dependence of the susceptibility of bismuth single-crystals upon the field,” *Proceedings of the Section of Sciences, Koninklijke Akademie van Wetenschappen te Amsterdam*, vol. 33, pp. 1106–1118, 1930.
- [36] M. Springford, “The anisotropy of conduction electron scattering in the noble metals,” *Advances in Physics*, vol. 20, no. 86, pp. 493–550, 1971.
- [37] M. I. Azbel and E. A. Kaner, “The Theory of Cyclotron Resonance In Metals,” *SOVIET PHYSICS JETP*, vol. 6, no. 6, pp. 1126–1134, 1958.
- [38] D. H. Lowndes, K. M. Miller, R. G. Poulsen, and M. Springford, “Studies of the anisotropy of electron-impurity scattering in metals by the use of the de Haas—van Alphen effect: application to gold,” *Proceedings of the Royal Society of London. A. Mathematical and Physical Sciences*, vol. 331, no. 1587, pp. 497–523, 1973.
- [39] A. Mathiessen and C. Vogt, “IV. On the influence of temperature on the electric conducting-power of alloys,” *Philosophical Transactions of the Royal Society of London*, vol. 154, pp. 167–200, 1864.
- [40] M. N. Baibich, J. M. Broto, A. Fert, F. N. Van Dau, F. Petroff, P. Etienne, G. Creuzet, A. Friederich, and J. Chazelas, “Giant Magnetoresistance of (001)Fe/(001)Cr Magnetic Superlattices,” *Physical Review Letters*, vol. 61, no. 21, pp. 2472–2475, 1988.

Bibliography

- [41] A. Fert, “Origin, development, and future of spintronics (Nobel lecture),” *Angewandte Chemie - International Edition*, vol. 47, no. 32, pp. 5956–5967, 2008.
- [42] J. J. Thomson, “On the theory of Electric Conduction through thin metallic films,” *Proceedings of the Cambridge Philosophical Society*, vol. 11, pp. 120 – 122, 1901.
- [43] K. Fuchs, “The conductivity of thin metallic films according to the electron theory of metals,” *Mathematical Proceedings of the Cambridge Philosophical Society*, vol. 34, no. 1, pp. 100–108, 1938.
- [44] A. F. Mayadas and M. Shatzkes, “Electrical-Resistivity Model for Polycrystalline Films: the Case of Arbitrary Reflection at External Surfaces,” *Physical Review B*, vol. 1, no. 4, pp. 1382–1389, 1970.
- [45] Y. Namba, “Resistivity and Temperature Coefficient of Thin Metal Films with Rough Surface,” *Japanese Journal of Applied Physics*, vol. 9, no. 11, pp. 1326–1329, 1970.
- [46] M. Jacob, G. Reiss, H. Brückl, and H. Hoffmann, “Electronic transport properties of giant-magnetoresistance Fe/Cr multilayers,” *Physical Review B*, vol. 46, no. 17, pp. 11208–11211, 1992.
- [47] R. D. Averitt and A. J. Taylor, “Ultrafast optical and far-infrared quasiparticle dynamics in correlated electron materials,” *Journal of Physics: Condensed Matter*, vol. 14, no. 50, pp. R1357–R1390, 2002.
- [48] K. L. Krewer, Z. Mics, J. Arabski, G. Schmerber, E. Beaupaire, M. Bonn, and D. Turchinovich, “Accurate terahertz spectroscopy of supported thin films by precise substrate thickness correction,” *Optics Letters*, vol. 43, no. 3, pp. 447–450, 2018.
- [49] V. Skoromets, H. Němec, V. Goian, S. Kamba, and P. Kužel, “Performance Comparison of Time-Domain Terahertz, Multi-terahertz, and Fourier Transform Infrared Spectroscopies,” *Journal of Infrared, Millimeter, and Terahertz Waves*, vol. 39, no. 12, pp. 1249–1263, 2018.
- [50] I. Ivanov, *Terahertz spectroscopy of graphene and graphene nanostructures*. PhD thesis, Johannes Gutenberg-Universität Mainz, 2018.
- [51] P. Kužel, H. Němec, F. Kadlec, and C. Kadlec, “Gouy shift correction for highly accurate refractive index retrieval in time-domain terahertz spectroscopy,” *Optics Express*, vol. 18, no. 15, pp. 15338–15348, 2010.
- [52] C. C. Katsidis and D. I. Siapkas, “General transfer-matrix method for optical multilayer systems with coherent, partially coherent, and incoherent interference,” *Applied Optics*, vol. 41, no. 19, pp. 3978–3987, 2002.
- [53] L. Duvillaret, F. Garet, and J. L. Coutaz, “A reliable method for extraction of material parameters in terahertz time-domain spectroscopy,” *Selected Topics in Quantum Electronics, IEEE Journal of*, vol. 2, no. 3, pp. 739–746, 1996.

- [54] D.-X. Zhou, E. P. J. Parrott, D. J. Paul, and J. A. Zeitler, “Determination of complex refractive index of thin metal films from terahertz time-domain spectroscopy,” *Journal of Applied Physics*, vol. 104, no. 5, p. 053110, 2008.
- [55] O. Heavens, *Optical properties of thin solid films*. New York: Dover Publications, 1991.
- [56] J. Lloyd-Hughes and T. I. Jeon, “A review of the terahertz conductivity of bulk and nano-materials,” *Journal of Infrared, Millimeter, and Terahertz Waves*, vol. 33, no. 9, pp. 871–925, 2012.
- [57] R. E. Glover and M. Tinkham, “Transmission of Superconducting Films at Millimeter-Microwave and Far Infrared Frequencies,” *Physical Review*, vol. 104, no. 3, pp. 844–845, 1956.
- [58] A. Thoman, A. Kern, H. Helm, and M. Walther, “Nanostructured gold films as broadband terahertz antireflection coatings,” *Physical Review B*, vol. 77, no. 19, pp. 1–9, 2008.
- [59] B. G. Alberding, G. P. Kushto, P. A. Lane, and E. J. Heilweil, “Reduced photoconductivity observed by time-resolved terahertz spectroscopy in metal nanofilms with and without adhesion layers,” *Applied Physics Letters*, vol. 108, no. 22, p. 223104, 2016.
- [60] D. J. Hilton, R. D. Averitt, C. A. Meserole, G. L. Fisher, D. J. Funk, J. D. Thompson, and A. J. Taylor, “Terahertz emission via ultrashort-pulse excitation of magnetic metal films,” *Optics Letters*, vol. 29, no. 15, p. 1805, 2004.
- [61] Z. Mics, K.-J. Tielrooij, K. Parvez, S. A. Jensen, I. Ivanov, X. Feng, K. Müllen, M. Bonn, and D. Turchinovich, “Thermodynamic picture of ultrafast charge transport in graphene,” *Nature Communications*, vol. 6, no. 1, p. 7655, 2015.
- [62] N. Smith, “Drude theory and the optical properties of liquid mercury,” *Physics Letters A*, vol. 26, pp. 126–127, jan 1968.
- [63] T. L. Cocker, D. Baillie, M. Buruma, L. V. Titova, R. D. Sydora, F. Marsiglio, and F. A. Hegmann, “Microscopic origin of the Drude-Smith model,” *Physical Review B*, vol. 96, p. 205439, nov 2017.
- [64] K. L. Krewer, W. Zhang, J. Arabski, G. Schmerber, E. Beaurepaire, M. Bonn, and D. Turchinovich, “Thickness-dependent electron momentum relaxation times in iron films,” *Applied Physics Letters*, vol. 116, no. 10, p. 102406, 2020.
- [65] G. Eranna, *Crystal Growth and Evaluation of Silicon for VLSI and ULSI*. Boca Raton: CRC Press, 2014.
- [66] R. Schad, P. Beliën, G. Verbanck, V. V. Moshchalkov, and Y. Bruynseraede, “Analysis of the transport properties of epitaxial Fe and Cr films,” *Journal of Physics: Condensed Matter*, vol. 10, no. 30, pp. 6643–6650, 1998.
- [67] S. Sangiao, L. Morellon, G. Simon, J. M. De Teresa, J. A. Pardo, J. Arbiol, and M. R. Ibarra, “Anomalous Hall effect in Fe (001) epitaxial thin films over a wide

Bibliography


- range in conductivity,” *Physical Review B - Condensed Matter and Materials Physics*, vol. 79, no. 1, pp. 2–6, 2009.
- [68] D. Hou, G. Su, Y. Tian, X. Jin, S. A. Yang, and Q. Niu, “Multivariable Scaling for the Anomalous Hall Effect,” *Physical Review Letters*, vol. 114, no. 21, p. 217203, 2015.
- [69] P. B. Johnson and R. W. Christy, “Optical constants of the noble metals,” *Physical Review B*, vol. 6, no. 12, pp. 4370–4379, 1972.
- [70] N. Laman and D. Grischkowsky, “Terahertz conductivity of thin metal films,” *Applied Physics Letters*, vol. 93, no. 5, pp. 1–3, 2008.
- [71] K. L. Krewer, K. Jiang, K. Bley, Z. Jin, Z. Mics, C. K. Weiss, K. Landfester, H.-J. Elmers, M. Bonn, and D. Turchinovich, “Large area conductive nanoaperture arrays with strong optical resonances and spectrally flat terahertz transmission,” *Applied Physics Letters*, vol. 111, no. 2, p. 021107, 2017.
- [72] S. Pandey, B. Gupta, A. Chanana, and A. Nahata, “Non-Drude like behaviour of metals in the terahertz spectral range,” *Advances in Physics: X*, vol. 1, no. 2, pp. 176–193, 2016.
- [73] V. V. Gerasimov, B. A. Knyazev, A. K. Nikitin, and G. N. Zhizhin, “A way to determine the permittivity of metallized surfaces at terahertz frequencies,” *Applied Physics Letters*, vol. 98, p. 171912, apr 2011.
- [74] S. Pandey, S. Liu, B. Gupta, and A. Nahata, “Self-referenced measurements of the dielectric properties of metals using terahertz time-domain spectroscopy via the excitation of surface plasmon-polaritons,” *Photonics Research*, vol. 1, no. 4, p. 148, 2013.
- [75] S. Ueda, M. Mizuguchi, M. Tsujikawa, and M. Shirai, “Electronic structures of MgO/Fe interfaces with perpendicular magnetization revealed by hard X-ray photoemission with an applied magnetic field,” *Science and Technology of Advanced Materials*, vol. 20, no. 1, pp. 796–804, 2019.
- [76] M. Cazzaniga, L. Caramella, N. Manini, and G. Onida, “Ab initio intraband contributions to the optical properties of metals,” *Physical Review B - Condensed Matter and Materials Physics*, vol. 82, no. 3, pp. 1–7, 2010.
- [77] S. Chatterjee and A. E. Meyerovich, “Interference between bulk and boundary scattering in high quality films,” *Physical Review B*, vol. 81, no. 24, p. 245409, 2010.
- [78] M. Dressel and M. Scheffler, “Verifying the Drude response,” *Annalen der Physik (Leipzig)*, vol. 15, no. 7-8, pp. 535–544, 2006.
- [79] “Drude model - Wikipedia.” https://en.wikipedia.org/wiki/Drude_model, 2020.
Accessed: 2020-01-28.

- [80] Bin Yu, Leland Chang, S. Ahmed, Haihong Wang, S. Bell, Chih-Yuh Yang, C. Tabery, Chau Ho, Qi Xiang, Tsu-Jae King, J. Bokor, Chenming Hu, Ming-Ren Lin, and D. Kyser, “FinFET scaling to 10 nm gate length,” in *Digest. International Electron Devices Meeting*, pp. 251–254, IEEE, 2002.
- [81] W. Spencer and T. Seidel, “National technology roadmaps: the U.S. semiconductor experience,” in *Proceedings of 4th International Conference on Solid-State and IC Technology*, pp. 211–220, IEEE, 1995.
- [82] G. Borghi, M. Fabrizio, and E. Tosatti, “Gutzwiller electronic structure calculations applied to transition metals: Kinetic energy gain with ferromagnetic order in bcc Fe,” *Physical Review B*, vol. 90, no. 12, p. 125102, 2014.
- [83] J. Sánchez-Barriga, J. Fink, V. Boni, I. Di Marco, J. Braun, J. Minár, A. Varykhalov, O. Rader, V. Bellini, F. Manghi, H. Ebert, M. I. Katsnelson, A. I. Lichtenstein, O. Eriksson, W. Eberhardt, and H. A. Dürr, “Strength of Correlation Effects in the Electronic Structure of Iron,” *Physical Review Letters*, vol. 103, no. 26, p. 267203, 2009.
- [84] A. Grechnev, I. Di Marco, M. I. Katsnelson, A. I. Lichtenstein, J. Wills, and O. Eriksson, “Theory of bulk and surface quasiparticle spectra for Fe, Co, and Ni,” *Physical Review B*, vol. 76, no. 3, p. 035107, 2007.
- [85] J. Schäfer, M. Hoinkis, E. Rotenberg, P. Blaha, and R. Claessen, “Fermi surface and electron correlation effects of ferromagnetic iron,” *Physical Review B*, vol. 72, no. 15, p. 155115, 2005.
- [86] H. M. Johnson and C. M. Seifert, “Sources of the Continued Influence Effect: When Misinformation in Memory Affects Later Inferences,” *Journal of Experimental Psychology: Learning, Memory, and Cognition*, vol. 20, no. 6, pp. 1420–1436, 1994.

ANGABEN ZUR PERSON

Keno Krewer

 Bertha-von-Suttner-Str. 12, 55291 Saulheim (Deutschland)

 152 06540085

 krewer+dis@posteo.de

SCHUL- UND BERUFSBILDUNG

-
- | | | |
|-----------------------|---|--------------|
| 01.06.2015–10.06.2020 | Dr. rer. nat. (Physik)
Max-Planck-Institut für Polymerforschung, Mainz (Deutschland)
"Time-resolving electrical conduction in thin iron films"
Supervisor: Prof. Dr. Bonn | EQF Niveau 8 |
| 09.05.2016–30.11.2018 | MAINZ-Graduate School of Excellence
Mainz (Deutschland)
Mitglied | |
| 08.08.2012–23.03.2015 | M.Sc. Physik
Johannes Gutenberg-Universität, Mainz (Deutschland)
Masterarbeit: "Plasmonic Structures in Simulation and Experiment" | |
| 01.04.2008–08.08.2012 | B.Sc. Physik
Johannes Gutenberg-Universität, Mainz (Deutschland)
Bachelorarbeit über "Plasmonisch verstärkte Emission spinpolarisierter Elektronen" | |
| 01.07.2001–20.03.2010 | Abitur
Elisabeth-Langgässer-Gymnasium, Alzey | |
| 01.04.2008–31.03.2010 | Frühstudium
Johannes Gutenberg-Universität, Mainz (Deutschland) | |

BERUFSERFAHRUNG

-
- | | | |
|-----------------------|---|--|
| 02.09.2013–06.12.2013 | ERASMUS-Praktikum
Department of Physics, Imperial College London, London (Vereinigtes Königreich)
Programmierung von Laborsoftware, Computersimulationen von metallischen Nanostrukturen | |
|-----------------------|---|--|

ZUSÄTZLICHE
INFORMATIONEN

Publikationen

- Krewer, K. L. *et al.* Thickness-dependent electron momentum relaxation times in iron films. *Appl. Phys. Lett.* **116**, 102406 (2020).
- Krewer, K. L. *et al.* Accurate terahertz spectroscopy of supported thin films by precise substrate thickness correction. *Opt. Lett.* **43**, 447–450 (2018).
- Krewer, K. L. *et al.* Large area conductive nanoaperture arrays with strong optical resonances and spectrally flat terahertz transmission. *Appl. Phys. Lett.* **111**, 021107 (2017).